UCLouvain

epl

École polytechnique de Louvain

Biomechanics - Mechanical characterization of artery tissue and synthetic arterial grafts

Author: **Alice Coirbay**
Supervisors: **Greet Kerckhofs, Valérie Lacroix**
Readers: **Nele Famaey, Thomas Pardoen, Laurent Delannay**
Academic year 2019–2020
Master [120] in Chemical and Materials Engineering

Acknowledgements

First of all, I would like to express my gratitude to my supervisor Prof. Dr. Greet Kerckhofs for her support during this year, especially in these unusual times. Also, I would like to thank her for sharing her expertise, for her regular and constructive feedback and for her availability. I would also like to thank my supervisor Prof. Dr. Valérie Lacroix for her clinical perspective. In addition, I thank Dr. Grzegorz Pyka for his technical and practical advice and optimistic guidance.

I would also like to thank Prof. Dr. Nele Famaey, Lauranne Maes and Dr. Heleen Fehervary for sharing their knowledge on the extension-inflation device and their valuable advice in optimizing the experimental protocol. My gratitude goes to Prof. Dr. Benoît Herman for his recommendations on the improvement of the mounting system and to Samuel Laurent for introducing his camera systems during a laboratory visit.

Finally, I would like to thank my family, Guillaume and my friends for their countless encouragements, their trust and for being a moral support through this journey.

Abstract

Cardiovascular diseases are one of the leading causes of death in the developed world. The need for accurate mechanical characterization of the native arterial tissue, along with synthetic graft materials, is essential and can provide valuable insights for the correct medical treatment to follow. The general aim of this thesis was to characterize the mechanical properties of native tissue and of one of the clinically available synthetic vascular graft materials, i.e. Dacron. For this purpose, both biaxial extension-inflation testing and 4D micro-CT was used.

Preliminary, extension-inflation tests identified parameter of the experimental protocol to be further optimized, such as the proper adjustment of the axial force and transmural pressure, the mounting system, the fluid and the shape of the triaxial cell.

Subsequently, two Dacron samples, each tested in different orientations, were imaged using a micro-CT combined with an *in situ* tensile mechanical loading. This specific experiment is called a 4D micro-CT. First, by visual inspection, a warp knitted Dacron graft was highlighted. This kind of graft is characterized by the longitudinal alignment of the knitted yarns. Then, the mechanical properties of Dacron were evaluated both in longitudinal and circumferential direction. The values of elastic modulus were of 5.75 MPa and 13.65 MPa, respectively. These values highlighted an anisotropy, already identified in some literature papers. Afterwards, the data acquired by the micro-CT scans were processed and a zero-strain test was realized to estimate the amount of error registered by the DVC analysis. Finally, three incremental DVC techniques were tested on Dacron. The "fixed reference image" conventional DVC method was used to visualize the evolution of the strain maps along a maximal displacement of 0.6 millimeter. For the Dacron sample tested in the longitudinal direction, the strain maps represented on the microstructure regions showed a higher strain accumulation in the fold, meaning that the folding induces concentration of stress. For the Dacron sample tested in the circumferential direction, higher tensile strain was identified in the region between the longitudinally warp knitted yarns of the microstrcuture. The thinnest part of the sample was assessed as it was a possible area of failure of the sample.

Performing 4D micro-CT on soft tissues, aorta in this work, needs the use of contrast agents that bind with some components of the material to enhance contrast and enable relevant observations. This specific technique is referred as 4D contrast-enhanced micro-CT (4D CE-CT). By visual inspection of the results, an insufficient penetration of the contrast agent through the sample was identified. In addition, the zero-strain test determined a high level of error for the aorta sample, consequence of this lack of staining of the soft tissue.

As a conclusion, this work is a first step in the standardization of the experimental protocol of the extension-inflation test. Furthermore, it emphasized the challenges of performing 4D micro-CT on a Dacron graft and 4D CE-CT on native tissue. Further perspectives would be to test more samples for measuring the mechanical properties of different materials.

Résumé

Les maladies cardiovasculaires sont l'une des principales causes de décès dans les pays développés. Une caractérisation mécanique précise du tissu artériel, ainsi que des matériaux synthétiques utilisés pour les greffes, est dès lors essentielle. Celle-ci peut fournir des informations précieuses pour le traitement médical correct à suivre. L'objectif général de cette thèse est de caractériser les propriétés mécaniques du tissu artériel et de l'un des matériaux synthétiques disponibles pour les greffes vasculaires, le Dacron. Pour ce faire, un test d'extension-inflation ainsi qu'une technique d'imagerie, la micro-tomographie à rayons X, combinée à un test de traction uniaxial *in situ*, appelé 4D micro-CT, ont été réalisés.

Dans un premier temps, le protocol experimental d'extension-inflation testé a permis d'identifier les paramètres à optimiser, tels que le bon réglage de la force axiale et de la pression transmurale, le système de montage, le fluide à utiliser et la forme de la cellule triaxiale.

Dans un deuxième temps, deux échantillons de Dacron d'orientation différente, ont été testés dans une expérience de 4D micro-CT. Tout d'abord, par inspection visuelle, les résultats du test ont permis d'identifier une greffe de Dacron tricotée en chaîne. Celle-ci est caractérisée par l'alignement longitudinal des fibres. Ensuite, les propriétés mécaniques du Dacron ont été évaluées, à la fois dans le sens longitudinal et dans le sens circonférentiel. Les valeurs du module élastique calculées sont 5,75 MPa et 13,65MPa, respectivement. Ces valeurs mettent en évidence une anisotropie, déjà mise en évidence dans certains articles de littérature. Ensuite, les données acquises par la tomographie ont été traitées et l'erreur enregistrée par l'analyse DVC a été evaluée par un premier test à contrainte nulle. Enfin, trois techniques de DVC progressives ont été testées sur l'échantillon de Dacron étiré de façon longitudinale. La technique basée sur une image fixe de référence a été choisie pour visualiser l'évolution des champs de deformation pour un déplacement maximal de 0,6 millimètre. Pour ce premier échantillon, les cartes de déformation représentées sur la microstructure ont montré une accumulation plus importante dans l'ondulation, ce qui signifie que l'ondulation induit une concentration de contraintes. Pour le Dacron étiré circonférentiellement, la déformation la plus élevée a été identifiée dans l'espace entre les fibres alignées en chaine. Cette partie, qui la plus fine de l'échantillon, a été évaluée comme étant la zone de défaillance possible de l'échantillon.

Concernant l'échantillon d'aorte, la realisation du 4D micro-CT nécessite la diffusion d'un agent de contraste à travers l'épaisseur du matériaux afin d'acquérir des images de bonne qualité. Lors de l'inspection visuelle des résltats, une diffusion insuffisante de l'agent de contraste a été identifiée. De plus, le test à contrainte nulle a déterminé un niveau d'erreur élevé pour l'échantillon de l'aorte, conséquence d'une absence de contraste.

En conclusion, ce travail constitue une première étape dans la normalisation du protocole expérimental du test d'extension-inflation. En outre, il met en évidence les défis rencontrés, dûs à la structure ondulée de l'échantillon de Dacron, lors de la micro-tomographie à rayons X, combinée à un test de traction uniaxial *in situ*. Finalement, les difficultés afin d'obtenir un contraste correcte lors de la micro-tomographie de l'aorte, dans ce cas-ci, sont soulignées. Quelques idées de solutions et de perspectives futures, comme l'étude des propriétés mécaniques de différents matériaux, sont également suggérées.

Contents

List of Figures

List of Tables

Chapter 1

Introduction

Cardiovascular diseases affect a large number of people. A cardiovascular disease that accounts for almost half of all deaths in Europe is atherosclerosis, a disease where the lumen of the artery narrows due to the formation of a plaque [25]. To treat those diseases, the placement of a bypass is often the best choice. In fact, 600 000 patients undergo coronary and peripheral vascular bypass graft procedures each year in the United States [29]. One first option for a bypass graft is to use autologous vascular substitutes, namely the saphenous vein or the internal mammary artery. The drawback is that these tissue sources may be inadequate or unavailable. In addition, the surgical procedure is invasive in time, cost, and potential additional morbidity.

To increase the efficiency of the procedure, researchers focused on the use of synthetic prosthetic vascular conduits having similar properties as human tissue. The first material tested as a synthetic graft was Vynion-N, but because of a lack of biostability, it was replaced by Dacron and ePTFE. However, both have advantages and drawbacks. Replacing autologous grafts by synthetic material is not as easy as it sounds. In fact, some complications can occur due to the mechanical properties mismatch. Mechanical properties are of great concern, knowing that compliance or diameter mismatch could lead to the development of anastomotic intimal hyperplasia and thrombus formation [3]. Thickening of the intimal layer of the artery wall is a normal phenomenon, beginning the healing process of the graft anastomoses. However, the progression of this thickening to a hyperplastic occlusive lesion at the distal end-to-side anastomoses is problematic and gives rise to the before-mentioned anastomotic intimal hyperplasia [30]. A thrombus is a blood clot due to aggregation of plaques, such as atherosclerotic plaque, resulting in the occlusion of the vessel [31]. Intimal hyperplasia and thrombus mostly occur in small diameter vascular graft (<6 mm) where the patency rate is shown to be disappointing [23]. This explains why, nowadays, the aim of researchers is to identify as accurately as possible, the mechanical properties of synthetic materials and native tissue.

In this thesis, to better understand the mechanical properties as well as the failure mechanisms occurring in the synthetic materials compared to native tissue, the extension-inflation experimental protocol will be tested and suggestions for further optimization will be made. This test is of significant importance because it replicates the physiological conditions very well. In addition, micro-CT imaging combined with *in situ* mechanical loading, i.e. 4D micro-CT, and 3D image analysis will be performed. This allows to visualize and quantify the mechanical behavior and local properties, respectively, under dynamic loading. Furthermore, the results obtained with the 4D micro-CT imaging may be useful to further optimize the extension-inflation tests experimental parameters.

Chapter 2

State of the art

2.1 Cardiovascular system

In order to get familiar with the properties and the typical values that characterize the vascular system, table 2.1 lists some key features. The typical value of heart rate for a young man is 70 beats/min. The stroke volume, which is the amount of blood pumped by the left ventricle of the heart per beat, is 80 mL [32]. The cardiac output corresponds to the heart rate times the stroke volume, which gives a value of 5.6 L/min. Finally, the mean pressure in the arteries is of 100 mmHg, which is equal to 13.33 kPa [6].

Table 2.1: Table of key figures of cardiovascular system [6].

Characteristic	Value	Units
Heart rate	70	beats/min
Stroke Volume	80	mL
Cardiac output	5.6	L/min
Mean Pressure	100	mmHg

2.1.1 Artery

To understand the properties that the synthetic materials have to fulfil, it is first essential to study the anatomy of the human artery. Arteries are blood vessels that bring oxygenated blood from the heart to the tissues of the body. They are generally split into two categories, the *elastic* arteries, which are located near the heart, and the *muscular* arteries that are located in the periphery. The artery wall is constituted of three layers as shown in figure 2.1.

The innermost layer, called *intima*, is in direct contact with the blood and is composed of endothelial cells, which are flat and polarized. This layer is very thin and does not influence the mechanical properties of the artery wall. However, as the intima stiffens and thickens with age, its contribution to mechanical properties can become significant. This

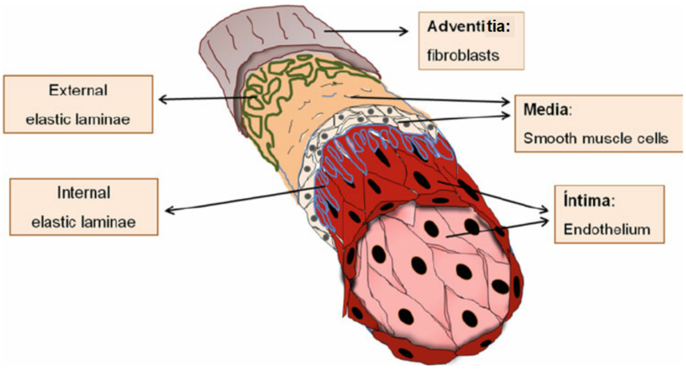

Figure 2.1: Different layers of the artery wall [1].

variation of the intima may be associated with *atherosclerosis*, which is one of the most common diseases of the arterial wall.

On top of this layer is the *media*, made of elastin, collagen and smooth muscle cells separated by elastic laminae. Between the intima and the media, an internal elastic lamina separates both layers. Elastin, collagen fibres, elastic laminae and smooth muscles cells are oriented and interconnected in a way that constitute a continuous fibrous helix. This specific structure gives the media the property of being the layer that resist the best to mechanical load.

The third, outermost layer is the *adventitia*. It is composed of a fibrous tissue constituted of fibroblast, fibrocytes, which are the cells that secrete collagen and elastin, and collagen fibrils. As the internal elastic lamina, the external elastic lamina separates the media from the adventitia. The adventitia has a role of stabilization and strengthening of the arterial wall thanks to the helical structure of the collagen fibrils [27].

2.2 Synthetic vascular grafts: Physical requirements

To be accepted by the human body, a synthetic graft must fulfil specific requirements. In fact, there are numerous problems associated with synthetic grafts, such as thrombogenicity and intimal hyperplasia. The ideal prosthetic bypass graft should therefore be biocompatible, non-biodegradable and have similar mechanical strength and compliance as the native tissue to withstand long-term hemodynamic stresses [23][25].

2.2.1 Biocompatibility

In general terms, biocompatibility is defined as the ability of a material to perform with an appropriate host response in a specific application [33]. However, this is a complex notion that contains a series of events or interactions happening at the tissue/material interface, which are influenced by intrinsic characteristics of the material and by the biological site of implantation.

In the case of vascular grafts, as they are meant to permanently replace the human arterial tissue, they must meet the basic biocompatibility requirements, defined by the ISO 10993 standards [1], namely, to be nontoxic, nonthrombogenic, noncarcinogenic, nonantigenic, and nonmutagenic. For biomaterials in contact with blood, the nonthrombogenic criterion is very important. In fact, arterial grafts must be thromboresistant, which is the ability of a material to reduce formation of thrombus by formation of platelet-based and/or fibrin-based clots. This will avoid coagulation and formation of a site prone to bacterial colonization and infection [34].

The healing process after the placement of vascular grafts corresponds to a cascade of events involving the contribution of many factors including coordination of host immune cells activity, migration, infiltration, proliferation and differentiation of endothelial cells, smooth muscle cells and their progenitors, all converging through the formation of new tissue. The most important cells are the macrophages, which respond rapidly to the implantation of the biomaterial. Indeed, after graft implantation, monocytes from the circulatory system are attracted to the site and will activate macrophages and release cytokines, which propagate into inflammation and fibrosis [2]. Fibrosis consist in an overgrowth, a hardening and/or scarring of fibrous tissue in an organ or tissue. It is attributed to excess deposition of extracellular matrix components including collagen [35]. This sequence of events is schematized on figure 2.2.

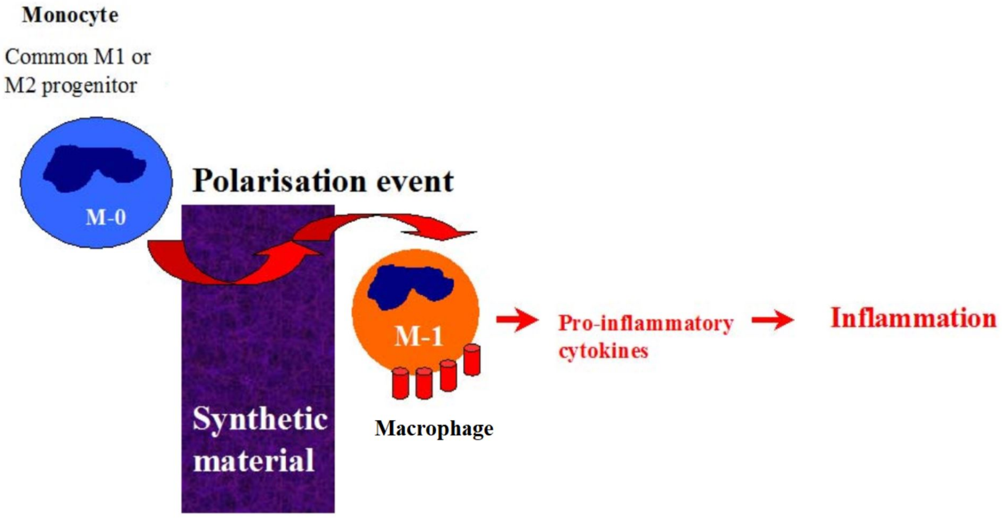

Figure 2.2: Sequence of events of the interaction of monocytes with synthetic materials leading to inflammation [2].

---

[1] ISO 10993 define a serie of standard that medical devices must fulfill to be considered as biocompatible

2.2.2 Biodegradibility

It is essential for the synthetic vascular graft to be non-biodegradable. Otherwise, it could result in irreversible change in the graft characteristics. There are several modes of degradation, but the principal ones include physical and chemical changes. Physical changes include swelling, plasticization, crystallization, fatigue, creep, and kinking. Factors that can induce chemical degradation are oxidation by inflammatory mediators or calcification. In addition, toxic by-products may also be released post-degradation, which should be avoided [23].

2.3 Mechanical properties of arteries and synthetic grafts

It has been shown, in many studies, that the differences in mechanical characteristics between the synthetic vascular grafts and the native tissue, such as mismatch in compliance, diameter, Young's modulus, and impedance phase angle, play an important role in the failure of the graft by intimal hyperplasia.

2.3.1 Compliance

Compliance is one of the most important properties of the artery and therefore of the vascular graft. In fact, a mismatch of compliance between the native artery and the graft at the anastomotic site may result in the failure of the graft because of altered pressure and flow dynamics. It is a structural property, meaning that its value depends on sample dimension and modulus [5].

Compliance is defined as the radial extensibility of the artery/graft in a physiological range of pressure. In other terms, it is a mechanical property that expresses a dimensional change with respect to luminal pressure change and is described as

$$C = \frac{\mathit{\Delta} D}{D P_P},$$

where D is the internal diameter in diastole, $\mathit{\Delta}$D is the change in internal diameter, and P_P is the pulse pressure [3]. It can be noted that this definition is applicable for dynamic compliance and not for static compliance. In static compliance measurements, the internal pressure P in a vessel is slowly increased and the corresponding dimensions are recorded. In opposition, dynamic compliance measurements depend on the degree of initial strain, governed by the mean pressure, and the deformation rate, governed by the frequency and magnitude of the pressure oscillation. In order to realise comparative measurements it is useful to reduce these variables to one. This is achieved by using the systolic-diastolic pressure, P_P, that appears in the equation above while only varying the mean pressure.

As explained before, compliance mismatch is a cause of graft failure. Two types of compliance mismatch can be considered, namely, tubular and anastomotic compliance mismatch.

Tubular compliance mismatch occurs at the interface between a compliant artery and a noncompliant graft, where the change in impedance will reduce the propagation of original pulsatile energy. The consequence of this resistance to pulsatile flow is the vibratory weakening of the arterial wall, the loss of endothelial cell viability and anastomotic aneurysm.

Anastomotic compliance mismatch is due to the stiffness of the graft wall and the suture technique. An increase in compliance can be observed a few millimetres on either side of the suture. This zone, called the para-anastomotic hypercompliance zone (PHZ), is illustrated on figure 2.3 and is responsible for intimal hyperplasia. There is at least three different ways in which this mismatch of mechanical properties around the anastomosis may develop intimal hyperplasia. First, a region of excessive mechanical stress can grow, leading to wall injury and therefore to intimal hyperplasia. In addition, cyclic stretching will induce the replication of vascular smooth muscle and the production of extracellular matrix due to the high level of distension and tangential stress. Thirdly, the sudden increase in compliance influences the residence time of the particles present in blood, the flow separation and stasis. This will result in low shear stress conditions, in which intimal thickening is likely to occur [3].

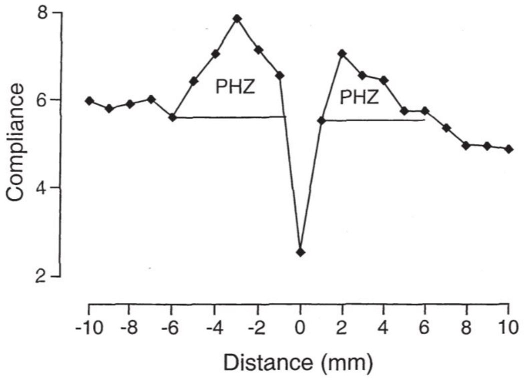

Figure 2.3: Compliance profile of a continuous anastomosis showing the para-anastomotic hypercompliance zone (PHZ). Anastomosis is at 0 mm [3].

2.3.2 Anisotropy

The anisotropic property of the artery is due to the multilayered heterogeneous structure of the artery wall. More specifically, the specific orientation of the helically wound collagen fibers is responsible for the anisotropic mechanical response [27]. In fact, arterial tissue is

40% stiffer in the circumferential than in the axial direction, and approximately 100% stiffer circumferentially when inflated to the physiological pressure [4]. This is illustrated on figure 2.4, where the difference in force and in modulus between the axial and circumferential direction is visible during a uniaxial test on porcine aorta.

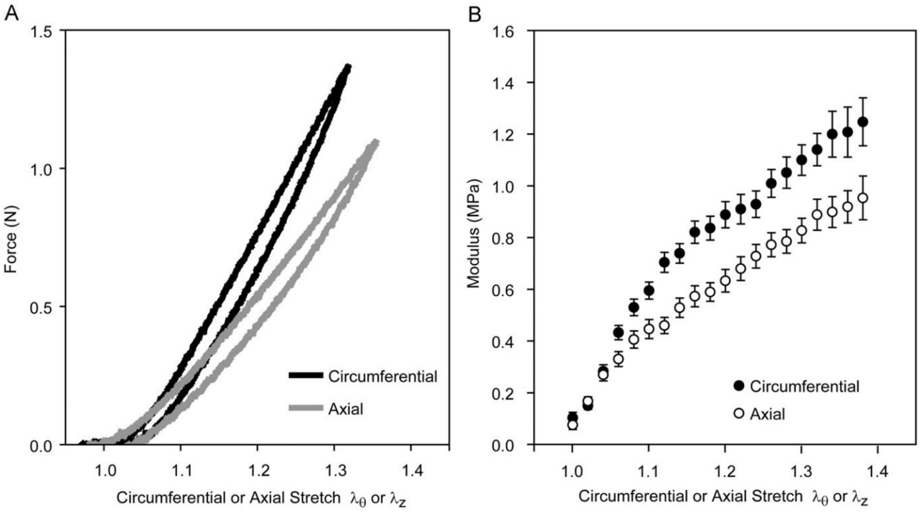

Figure 2.4: Behavior in uniaxial tests of porcine aorta. (A) Force-stretch response showing a greater resistance to deformation along the circumferential axis compared to the axial axis. (B) Circumferential and axial moduli demonstrating non-linear behaviour. The tissue average stiffness is 41% greater in the circumferential direction compared to the axial one [4]

Two types of anisotropy exist: the *inherent anisotropy* due to structural features of an unstressed material and *induced anisotropy* due to superimposed stresses on a non-linear material in different directions. These anisotropic mechanical properties must be replicated by the graft because they prevent excessive stimulation of the anastomotic region, while being compliant in radial direction to prevent any flow disturbances [5].

2.3.3 Viscoelasticity

The viscoelasticity or stress relaxation is the property that determines the hemodynamic behaviour of an arterial vessel and is difficult to reproduce in synthetic grafts [5]. Due to the fact that the artery has viscoeleastic properties, it will induce a delayed response when subjected to cyclic inflation-deflation stresses, known as hysteresis. Drawing the hysteresis loop, as in figure 2.5, is useful to determine the energy lost in each cycle. It also indicates that a major component of strain energy is recovered elastically each time arterial wall is distended. The fatigue behaviour of arteries is potentially improved by the viscoelastic property because it reduces dynamic stresses and strains in the wall. In synthetic implants, viscoelasticity depends on the structural construction and on the property of the material they are made of. However, in general the hysteresis loop of synthetic implants is smaller that the one of artery, meaning that less energy is lost in each cycle.

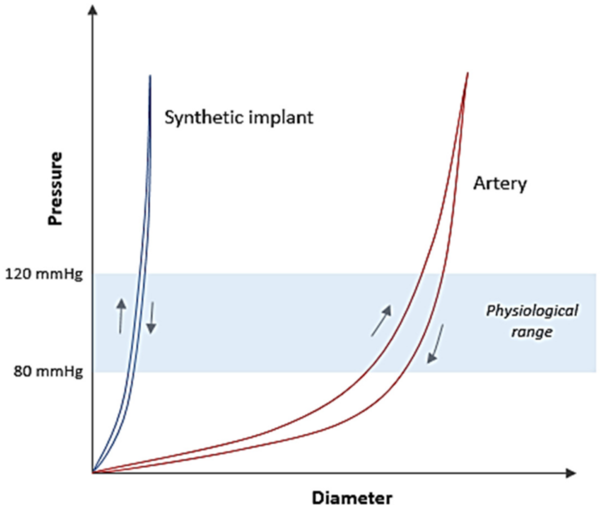

Figure 2.5: Comparison of the pressure-diameter curve between an artery and a synthetic implant [5].

2.3.4 Stress-Strain behaviour

The stress-strain behaviour of the artery is very specific. Arteries must be distensible to provide capacitance and a pulsatile circulation, but they must also withstand inflation over a range of pressure [36]. This explains why the stress-strain behaviour of the native arterial tissue is, nowadays, still quite different from the one of a synthetic graft.

As most soft biological materials, blood vessels do not have simple linear elastic properties. So that, on the one hand, the native artery presents a very low stress response at low pressures and a steep increase in elastic modulus as the pressure is increased; this relates to the property known as the non-linearity or incremental elastic modulus, which is one of the most important mechanical property of the artery [5]. On the other hand, synthetic grafts often show low elasticity and a higher linear stress response for similar levels of strain (figure 2.5).

In addition, the artery is an heterogeneous structure, which makes it difficult to match it with the mechanical properties of the vascular graft, most often being an homogeneous structure. In fact, collagen and elastin, which are the structural components of the mechanically dominating layer, the media, have very different elastic moduli; 1 GPa and 0.6-1 MPa respectively. This composite structure of arteries, which is a combination of both rubbery and stiff fibrous constituents, gives the non-linear properties. On figure 2.6

the incremental elastic modulus, E_{inc}, is illustrated with the distinction of the two regions dominated by elastin and collagen.

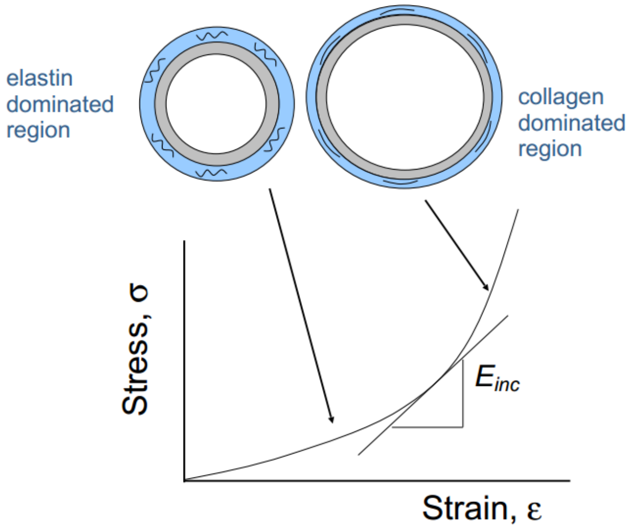

Figure 2.6: Stress-strain behavior of the artery with the representation of the incremental modulus as well as the distinction between the collagen-dominated region and the elastin-dominated region [6]

2.3.5 Residual stress

It is important to differentiate the load-free configuration and the stress-free configuration. The unloaded state, when there is zero transmural pressure and zero axial load, is commonly referred to as the initial state where stresses and strains are considered to be zero [37]. However, this is not the case in arteries, since residual stresses exist in the tissue. The residual stress is the stress that remains in a body after removal of external loads [38]. The presence of this residual stress in the arterial wall becomes evident when a segment of the vessels springs open after being longitudinally cut. It is due to the growth and remodeling of the vessel and one of its role is to reduce the transmural distribution of stresses across the arterial wall. In addition, after the sudden relief of the initial residual stress, the opening angle will be time-dependent, showing that the state of the artery succeeding the cutting is not fully stress-free. The different configurations of the artery are shown on figure 2.7. To incorporate the residual stress in the arterial model, the *opening angle method* is used [37].

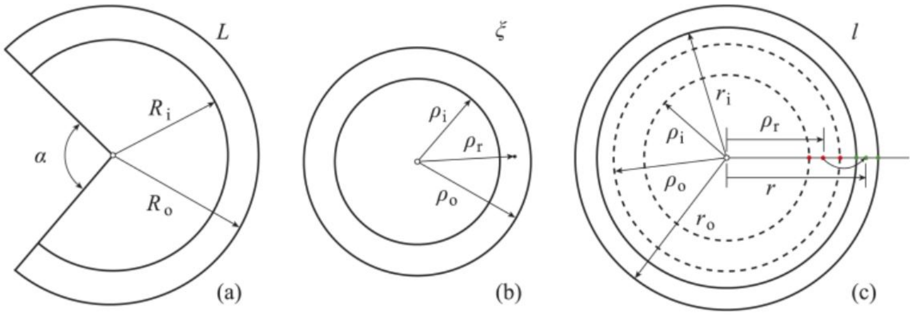

Reference configuration
(load-free, stress-free)

Load-free configuration
(residually stressed)

Loaded configuration

Figure 2.7: Representation of the residual stress through the different configurations of the cross-section of a cylindrical artery: (a) the reference configuration with an opening angle α; (b) the stressed load-free configuration; (c) the loaded configuration (due to the applied internal pressure and axial force) compared with the load-free configuration (dashed curves). The parameters L, ξ and l denotes the lengths of the arterial segments in the three configurations, respectively [7].

2.4 Clinically applied synthetic vascular grafts

Graft failure is more likely to happen if there is compliance mismatch between the artery and the graft [3]. Nowadays, two synthetic materials are used in a clinical setting (Dacron and Gore-Tex), but this section will also introduce the first synthetic material invented for this application (Vinyon-N), which was their predecessor.

2.4.1 Vinyon-N

Vinyon-N was the first synthetic graft material clinically used. It was introduced in 1952 by Voorhees, who used Vinyon (polyvinylchloride) synthetic fibres as a scaffold to repair the arterial wall of dogs [39]. A first clinical study of cloth prostheses tested in eighteen cases of arteriosclerotic aneurysms was realized in 1954, but only ten persons survived [40]. Nevertheless, Vinyon-N was promising because of the porosity of its structure, which enabled capillaries to form and fibroblasts to proliferate and therefore organizing a new inner surface [3]. Unfortunately, because of a lack of long-term biostability, which is the ability of a material to withstand biodegradation, and an inappropriate scaffold for tissue ingrowth

Several years later, researchers came with new ideas of polymeric materials for synthetic vascular grafts. They developed grafts using polymers such as polyethylene terephthalate (PET) or polytetrafluoroethylene (PTFE).

2.4.2 Dacron - Polyethylene terephthalate (PET)

Polyethylene terephthalate has the chemical formula, $[O - C = O - C_6H_4 - O - C = O - CH_2CH_2]_n$ and the acronym PET [23]. It is a thermoplastic polyester and commercialized under the name of Dacron when made into fibres that form a synthetic vascular graft [25]. In fact, as the Young's modulus of PET is quite high (2.8-3 GPa [8]), it is convenient to make fibres out of it to form a fabric (woven or knitted configuration).

The woven graft has small pores and is dimensionally stable, but less extensible than the knitted configuration. It involves two sets of yarns perpendicularly to each other [8]. As shown on figure 2.8, there are two kinds of weave: plain weave, which is very resistant, but has low flexibility, and twill weave, which has both good resistance and flexibility.

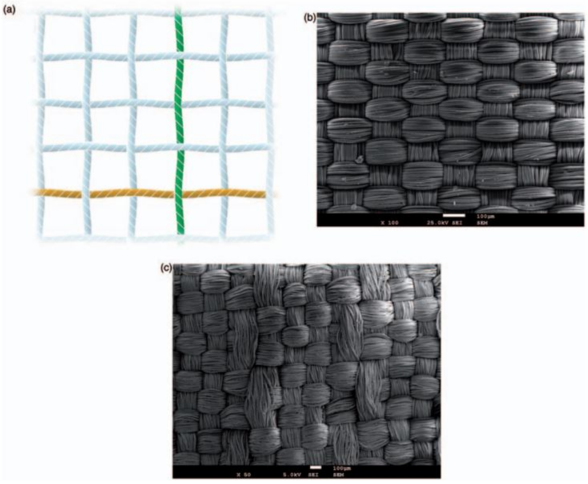

Figure 2.8: Dacron woven graft: (a) Graphic representation; (b) Scanning electron microscopy (SEM) of an endovascular prosthesis woven fabric with plain-weave pattern; (c) SEM of an endovascular prosthesis woven fabric with twill-weave pattern [8].

Knitted Dacron is strong and has a highly crystalline structure [3][23]. The knitted graft has larger pores, is more flexible than the woven graft and can be radially distended. It is formed by looping fibres together, which is called the velour technique [29]. The larger pores will enable a better tissue ingrowth and are more compliant. There are two categories of knitted grafts: warp knit (loop along the length of the fabric) and weft knit (loop across the width of the fabric). As for woven fabrics, properties of the lattice, such as flexibility and pore size, can be controlled by changing the density of the knit. As limitation, it can be noted that, because of the larger pore size and therefore water permeability, grafts need to be perclotted with gelatin, collagen and albumin to prevent seepage [8][25].

Both knitted and woven Dacron vascular grafts have a folded structure in order to

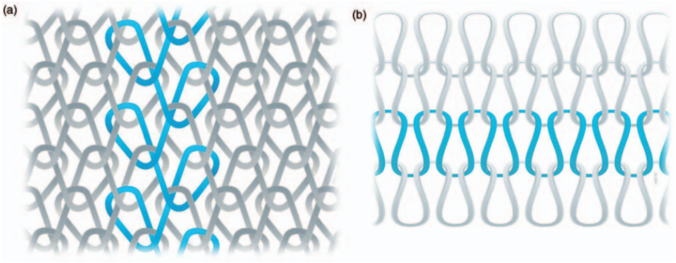

Figure 2.9: Dacron knitted graft: (a) warp knit; (b) weft knit [8]

mimic the structure of collagen fibers in natural blood vessels. In arteries, the elastic fibers plaited with collagen fibers constitute wavy membranes. This waviness enables to withstand the internal pressure and the longitudinal stretch applied to the artery during blood flow [41].

2.4.3 Gore-Tex (Expanded PTFE)

Polytetrafluoroethylene has the chemical formula $[-(\mathrm{CF_2}-\mathrm{CF_2})-]_\mathrm{n}$, and has the acronym PTFE. It is an inert and very versatile fluorocarbon polymer. In 1969, Gore discovered that, by extrusion and sintering of the polymer under the right conditions, he could change its properties and create a strong and microporous material. It was then patented as Gore-Tex and called expanded PTFE or ePTFE. It is manufactured in a porous tube composed of node-fibril microstructure, shown on figure 2.10, with a standard pore size of about 30 µm [25].

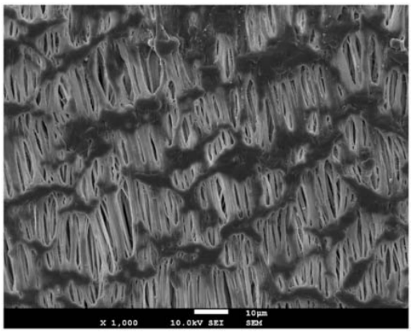

Figure 2.10: SEM of ePTFE and its polymeric node-fibril microstructure [8].

As for Dacron, the porosity of the graft can be controlled, which can be an advantage because it will promote the in-growth of tissue and formation and retention of an endothelial layer. Nevertheless, the right amount of porosity must be reached to avoid the deposition of other materials on the surface. This biosynthetic material is highly crystalline with a tensile modulus of elasticity of 0.5 GPa and tensile strength of 14 MPa [8][23]. ePTFE is more biostable than Dacron, meaning that it is less disposed to deterioration in a biological environment. One last characteristic of Gore-Tex is that its luminal surface is electronegative, which reduces its interactions with blood elements [29].

2.4.4 Vectra-Polyurethane

Even though results are satisfactory in larger vessels for Dacron and ePTFE, there are still limitations in terms of patency rates for small-diameter (< 6mm) grafts and low flow rates. In fact, in small vessels, these biosynthetic materials induce formation of thrombus on its lumen, and compliance mismatch at the anastomotic site causes formation of intimal hyperplasia [23][3]. Researchers have, therefore, expanded their interest in other possible solutions including polyurethane, tissue engineering approaches and coatings, the two latter to be discussed in the following sections.

Polyurethanes (PU), of chemical formula, $[-\mathrm{NH}-\mathrm{O}=\mathrm{C}-\mathrm{O}-\mathrm{R}-]_\mathrm{n}$ is a large family of elastic polymers containing a urethane $[-\mathrm{NH}-(\mathrm{CO})-\mathrm{O}-]$ group. These polymers were developed in Germany in the 1930s and used in biomedical applications since the 1960s. As polyurethanes are more likely to match the compliance of native tissue, and therefore to reduce the incidence of intimal hyperplasia at the anastomotic sites, they seem to be a good alternative to ePTFE and Dacron.

They are copolymers of three different segments of monomer, each having a specific function. One is crystalline (hard) for rigidity, a second is amorphous (soft) for flexibility and a third serves as a chain extender. The amount of each segment can be varied in order to reach the right mechanical behaviour and, more precisely, the right compliance. Polyurethanes are known for their good biocompatibility, high tensile strength, fatigue properties, ease of handling and processing versatility. The tensile strength ranges between 20 MPa and 90 MPa and the tensile modulus is of 5 MPa to 1150 MPa [8].

Several generation of polyurethanes have been tested. The first generation was polyester polyurethane and had the disadvantage of being *in vivo* degradable, because of the degradation of the polyol soft segment. Then, polyetherurethaneurea, patented as Vectra®, with a pore size of 15 µm was developed. The graft is manufactured with a non-porous layer under the luminal surface, which makes it impermeable to liquids. However, the PU graft elongated with time after implantation, and the incidence of pseudointimal formation [2] near the anastomosis was higher than with ePTFE grafts [43]. The next generation, Corvita®graft, was carbon-based PU with no ether/ester linkages, better stability and more resistant to biodegradation. It did not show changes in diameter at one year postimplantation [44]. Cardiotech®, currently under clinical trial, made of poly(carbonate-urea)urethane is resistant to hydrolytic and oxidative stresses and remains patent even 36 months after implantation into the aorto-iliac segment of four dogs [45]. Pulse-Tec®is another promising polyurethane graft with a pore size of 28 µm, since it

---

[2] A biological interface between a fibrin surface and blood [42]

has an excellent radial compliance with concordant hydrogen and homogeneity, but it is structurally weaker than similar PU grafts [46] and susceptible to oxidative degradation [43].

In conclusion, polyurethane vascular grafts have a better thromboresistance and reduce anastomotic hyperplasia compared to Dacron and ePTFE, but studies have shown that they are susceptible to be biodegradable, which unfortunately results in mechanical failure [25][23]. In addition, one major concern of PU grafts is the potential carcinogenic effect of its degradation products [43]. Table 2.2 summarizes and compares the mechanical properties, the advantages and the disadvantages of the synthetic material presented above with the native tissue.

2.4.5 Coating

In order to reduce thrombogenicity of synthetic materials, researchers tried to fix chemicals or anticoagulants to the graft lumen [25]. Several techniques have been used, such as, carbon deposition, photodischarge, and plasma discharge technologies to deposit reactive groups onto the polymer surfaces [29]. For Dacron, it has been shown that the patency rates of bypass grafts improved by coating its lumen with heparin and its outer surface with collagen [23]. In the case of ePTFE, fibronectin-coated graft improved graft healing and surfaces coupled with an adhesion peptide significantly improved endothelial attachment [29]. Unfortunately, the most appropriate coating is unclear so that it is still in the clinical trial phase.

2.4.6 Tissue engineering

Another approach to try to prevent thrombus formation, compliance mismatch and low patency rate of small diameter vascular vessels is tissue engineering. This technique has already been successful for the healing of chronic wounds and burns and, at experimental level, in repair of cartilage defects [47].

The basic principle of tissue engineering, illustrated on figure 2.11, is to regenerate certain parts of the human body. Tissues are created *in vitro* originated from embryonic or adult stem cells. To grow, cells need a three-dimensional mechanical support, called a scaffold, to provide the initial graft shape and strength. The scaffold is, in most cases, degradable and has a porous structure that allows cells to adhere, migrate, proliferate and differentiate, and to secrete extracellular matrix [9]. There are two main approaches concerning the use of the scaffold [48][49]. First, it can be used as cell support device upon which cells are seeded *in vitro*. This will encourage the growth or regeneration of functional tissue and therefore the production of the tissue foundations for transplantation. Secondly, the scaffold can be used as a growth factor or drug delivery device. Upon implantation, it will recruit cells from the body and encourage the body's natural ability to repair itself and help determination of new tissue growth direction.

However, the challenges to tissue engineer blood vessels with the mechanical properties of native vessels, and with anti-thrombotic properties are immense, but achievable. To

Table 2.2: Summary of mechanical properties of the different materials studied (native tissue [22] and synthetic grafts [5][23][24])

	Native tissue	Vinyon-N	Dacron	Gore-tex	Vectra
Tensile strength	1.44±0.87 MPa	.	**Knitted**: 170-180 MPa **Woven**: 72-74 MPa	14MPa	20-90 MPa
Tensile modulus	1.48±0.24 MPa	.	**Knitted**: 2800-3000 MPa **Woven**: 800-900 MPa	500 MPa	5-1150 MPa
Advantages	No thrombus formation, compliance matching, lower risk of rejection, autologous graft	Porous	**Knitted**: Strong, larger pores: tissue ingrowth, flexible, more compliant **Woven**: Stable, resistant, lower permeability	Porosity, better biostability, electro-negative luminal surface	More compliant, controllable rigidity and flexibility, good biocompatibility, fatigue properties, less thrombogenicity
Drawbaks	Not always available nor adequate, invasive surgery	Lack of long-term biostability and insufficient ability to proliferate tissue	**Knitted**: Permeable, dilatation over time **Woven**: smaller pores, reduced compliance	Limited incorporation, perigraft seroma formation, stitch bleeding	*in vivo* degradable, potentially carcinogenic

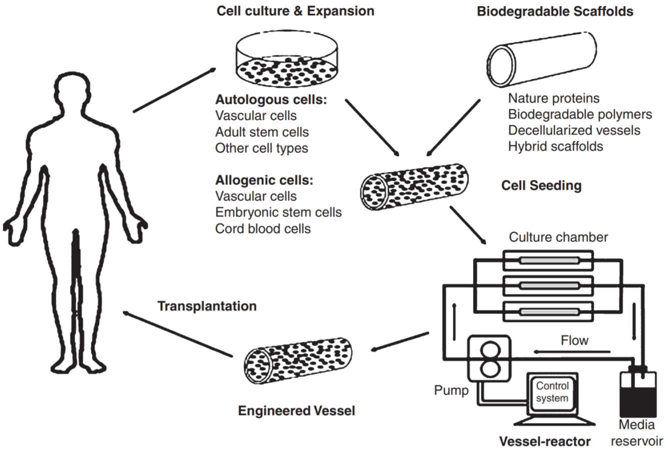

Figure 2.11: Scheme illustrating the tissue engineering approach to prepare vascular grafts [9].

cite some of them, tissue engineered blood vessels must provide a conduit that will have sufficient strength not to burst with changes in blood pressure, a vessel wall that is elastic and can withstand cyclic loading, matching compliance with the adjacent host vessel, a lining of the lumen that is anti-thrombotic and must function immediately after implantation without relying on remodeling of the tissue *in vivo*.

The first attempt to create such a tissue-engineered blood vessel was done by Weinberg and Bell in 1986 [50]. In the field of tissue engineered vascular grafts, four major approaches can be identified: permanent synthetic support, natural acellular tissues, a biodegradable scaffold, and a non-scaffold technology [51].

Natural scaffolds from tubular organs are the most obvious scaffold for tissue engineering of arteries, because they already contain the appropriate extracellular components. Concerning the permanent support, collagen gel scaffolds were first used as said before by Weinberg and Bell, and further improved by surrounding them with a supporting sleeve of collagen or Dacron. Biodegradable synthetic scaffolds are usually made of polyglycolic acid, which is the most commonly used biodegradable polymer [25]. The advantage of this approach is that scaffolds will have the appropriate physical strength as well as the degradation kinetics of synthetic polymers, together with the biological specificity of the major extracellular components. The non-scaffold technology is based on the assembly of two layers, one forming the media layer constituted of smooth muscle cell sheet and another one forming the adventitial layer, which consist in a fibroblast sheet. Those two layers are rolled over a permeable mandrel to assume the tubular configuration.

To regenerate tissue from the patient is a promising approach, but it is still in the clinical research phase since there are major issues to overcome. Two of them are the fact that the graft usually needs one to three months to be prepared so that it cannot be used in emergency situations and, because of the long period of culture needed to produce the graft, the risk of infection and cell transformation is increased as well as the cost in terms of equipment and materials [51]. In table 2.3, a comparison between the new techniques and the autologous graft is presented.

Table 2.3: Comparison of the advantages and disadvantages between the native tissue, the synthetic materials and tissue engineered blood vessels [25].

	Native tissue	Synthetic graft	Engineered blood vessels	Coated-vascular grafts
Advantages	Non-trhombogenecity, compliance matching, lower risk of rejection, autologous graft	Directly available, biocompatible, porous to enable cell gingrowth	Responsiveness, non-thrombogenecity, self-repair, growth, metabolically active, potentially cost-effective	Improved endothelial cell attachment and patency rates
Drawbacks	Not always available nor adequate, invasive surgery	Compliance mismatch, thrombogenecity for small-diameter vessels	Still in clinical trials: No direct availability for emergency, long time of preparation, long period of culture	Unclear appropriate coating, still in clinical trials

2.5 Mechanical characterization methods for arterial tissue and synthetic grafts

To ensure that arterial tissue and synthetic grafts show the most similarities in their mechanical behavior, mechanical characterization of both materials is necessary. It is significant to note that mechanical characterization of the arterial wall is influenced by physical and chemical factors such as temperature, osmotic pressure, pH, partial pressure of carbon dioxide and oxygen, ionic concentrations and monosaccharide concentration. To consider those factors is essential when measuring samples in *ex vivo* conditions. In fact, if they experience biological degradation, their mechanical behaviour does not match that of *in vivo* arteries anymore. The need to test samples mimicking the physiological condition as well as possible is obvious [27].

This section will present three mechanical characterization methods used for native artery tissue and graft material as well as a way to observe, in a non-destructive approach, the relationship between the structure of the material and its mechanical behavior. All of these methods require a pre-conditioning step before running the test. This pre-conditionning step is necessary to overcome the effects of tissue handling and to establish a repeatable reference state [52]. It is conducted by subjecting the sample to a series of loading-unloading cycles until the behaviour becomes repeatable. The pre-conditioning is dependent of the maximum strain imposed, and the pre-conditioning protocols must be the same for coherent results.

2.5.1 Uniaxial testing

Uniaxial tensile testing is one of the most common tests in order to determine the mechanical behaviour of biological tissues. The sample studied is typically a dog bone-shaped piece submitted to elongation in a single direction (figure 2.12).

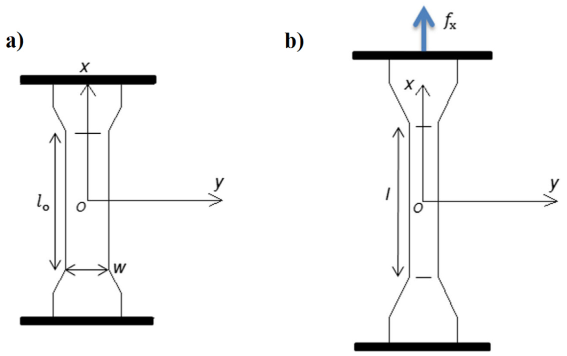

Figure 2.12: Schematic of a uniaxial tensile test. (a) Reference configuration and (b) deformed configuration [10].

The dog bone-shaped format is useful because it has a smaller width in the middle of the sample to ensure the failure at a specific emplacement. The test is often realized until failure to get the value of the maximal elongation the tissue can experience before breaking, namely, the ultimate tensile strength. With the data collected, it is interesting to plot a graph expressing the relationship between the calculated stress and strain values. To do so, the values to be measured are the initial dimensions, the displacement during elongation and the force in the direction of the elongation. Uniaxial tensile testing data are useful to compare different specimens but they are not sufficient to obtain three-dimensional anisotropic constitutive relations and do not replicate the real *in vivo* loading conditions [10].

2.5.2 Planar biaxial testing

As uniaxial testing does not provide enough information to completely characterize the sample's behaviour, planar biaxial testing can be performed, as illustrated on figure 2.13. A thin planar squared-shaped sample is cut and is submitted to a loading regime similar to the one of *in vivo* conditions. The variables that must be measured are the initial dimension of the sample, the displacement of tracking markers during testing and forces in the two test directions. Tracking markers are applied to the surface of the sample before the beginning of the test.

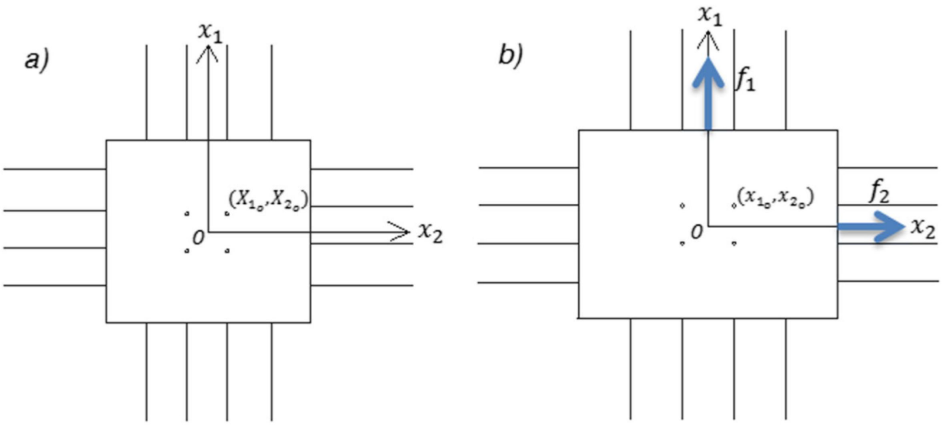

Figure 2.13: Schematic of planar biaxial tension test in the (a) reference and (b) deformed configuration [10].

The studied specimen is mounted along the edges employing flat clamps, rakes, sutures. The boundary conditions are different depending on the mounting mechanisms [53]. Clamps apply a load continuously over the four edges of the sample but the forces at the clamps are not fully transmitted to the center of the sample. Therefore, the sample may appear more stiff. Rakes consist in five needles mounted on a base with their tips pierced through the sample. The loading is applied discretely and allows transverse movement of the sample, however, the base of the rakes experiences a bending force. The last mechanisms requires flexible wires to perform sutures. There will be no bending force associated, but the mounting is less repeatable and spacing between sutures less uniform.

Planar biaxial tests can be conducted at either constant loading rate or stretch rate thanks to the independent loading applied along each axis. This test can also be applied until failure to analyse biaxial failure mechanisms, in which case clamps would be required to avoid failure near gripping points. Data about ultimate tensile stress can be collected and it is observed that they are different in longitudinal and transverse directions. Biaxial testing is insufficient to fully characterise the three-dimensional behaviour of an anisotropic material when the shear components are significant [10].

2.5.3 Extension-inflation testing

The extension-inflation testing is a relatively new technology that mimics the physiological loading conditions of tubular samples very well and preserves the native geometry of the sample. It is an alternative method to planar biaxial testing, where force is applied transmurally and axially.

The sample is typically loaded through stretching in the axial direction to produce axial load, and a transmural pressure, P, is produced by pumping fluid into the vessel. The axial elongation will lead to an increase in axial stress and the inflation pressure will induce a change in circumferential and axial forces [28]. A scheme of a sample under extension and inflation can be found on figure 2.14.

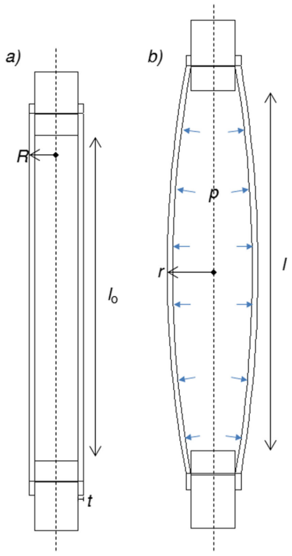

Figure 2.14: Schematic of an artery under exension-inflation testing in (a) reference configuration and (b) deformed configuration [10].

In addition, as this test is sometimes realized on a triaxial device, a third torsional component can be added. In fact, it is demonstrated that native artery tissue is often submittted to bending and twisting in *in vivo* conditions [54]. Multiaxial testing enables, thus, to replicate the artery behaviour under three-dimensional loading, which considers all spatial variations in deformation, and gives insight into the behaviour of heterogeneous, irregularly-shaped samples. In this thesis, extension-inflation without torsion will be considered [10].

2.5.4 Remaining issues of mechanical testing

In table 2.4, a comparison of the different methods detailed above is presented. Each one of the testing methods has its proper measured parameters, advantages and drawbacks. Extension-inflation testing has a great potential since, among other advantages, it nearly fully mimics the physiological loading behaviour. Unfortunately, as said above, one remaining issue of this method is the not yet standardized testing protocol.

Table 2.4: Comparison of the different mechanical testing methods: Uniaxial testing ([10]), Planar Biaxial testing ([10][26]) and Extension-Inflation testing ([10][27][28]).

	Uniaxial testing	Planar biaxial testing	Extension-Inflation testing
Measured parameters	Young's modulus, Yield stress, Ultimate tensile stress	Ultimate tensile stress, Normal and shear stresses	Relation between internal pressure and circumferential stretch, Relation between axial force and circumferential stretch, Compliance
Advantages	Easy to perform, Useful to compare specimen	Analyse biaxial failure mechanisms, Information about the anisotropic stress-strain behaviour	Mimics the physiological loading of arteries very well, Preserves *in vivo* structure of arteries, Collects accurate data for Finite Element method simulation and determination of appropriate constitutive equations, Describes non-linear and anisotropic behaviour of artery wall
Drawbacks	Does not replicate *in vivo* loading condition, Does not preserve the *in vivo* structure of arteries, Data collected not sufficient to obtain 3D constitutive relations, Anisotropic behaviour not described	*In vivo* structure of arteries not preserved, Data collected not sufficient to obtain 3D constitutive relations, Data complicated by in-plane shear, tissue heterogeneities, inelastic changes in specimen geometry	Protocol not yet optimized and standardized, Mounting the sample is more difficult, More tissue needed because of the tubular structure of the sample analysed

2.5.5 Micro-CT imaging and 3D image analysis combined with in situ mechanical loading (4D micro-CT) of native tissue and synthetic material

A) Micro-CT imaging

One of the main challenge in vascular biomechanics is the detailed characterization of the relationship between the micro-scale mechanisms and the mechanical response of the tissue [12]. There are several techniques able to provide micro-structural characterization of materials, but the most accessible is X-ray microfocus computed tomography (micro-CT).

Micro-CT is a non-destructive technique able to provide 3D information of materials. The acquired set of images enables the visualization of the internal architecture at the microscopic level. In addition, image analysis of the micro-CT images results in an extensive 3D quantitative description of the morphology of materials, and thus highly suitable for the synthetic materials presented before and native artery tissue [55]. The main acquisition steps of X-ray computed tomography are shown in figure 2.15.

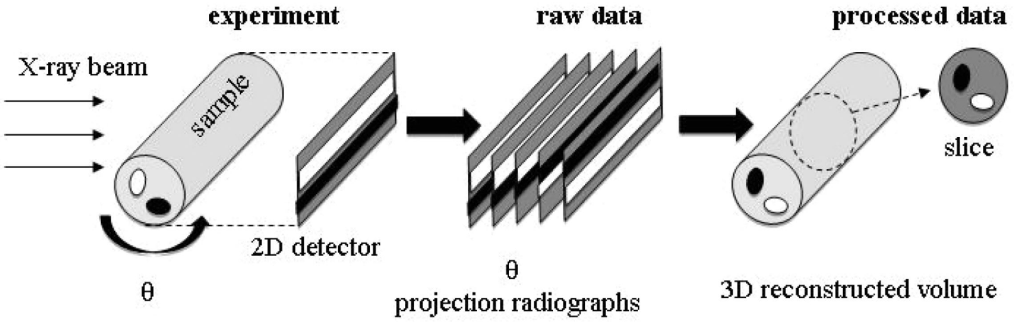

Figure 2.15: Main acquisition steps of X-ray computed tomography [11].

The basic principle of micro-CT is X-ray radiography. An X-ray beam is sent through a sample and the transmitted beam is recorded on a detector [56]. All micro-CT devices follow the same sequence of elements: an X-ray source, a specimen to be imaged and a detector able to convert the electric signal in an image array. A device that either rotates the specimen within the stationary scanners or, in the case of *in vivo* micro-CT devices, rotates the scanner around the stationary specimen, is also required.

Radiography is based on Beer-Lambert's law, which relates the absorption of electromagnetic waves to the material through which the light passes. The absorption of X-rays passing through a material is related by the following equation,

$$\frac{I}{I_0} = exp(-\mu t)$$

where I is the intensity of transmitted X-rays, I_0 is the intensity of incident X-rays, μ is the linear attenuation coefficient of the material and t is the thickness of the material through which X-rays have travelled [57]. The parameter responsible for the X-ray image contrast is the linear attenuation coefficient (μ), which is dependent on the density and the atomic number of the material.

For the study of the microstructure and failure mechanisms in biological and engineering materials, micro-CT has become a popular tool producing 3D maps of the X-ray linear attenuation coefficient. However, the image quality can be influenced by limitations of the system performance, which gives rise to artefacts in the reconstructed image. It is important to take these artefacts into account to distinguish them from real features and for optimizing experimental design in order to minimise their effect on the results [19]. Appendix A highlights some of the most relevant artefacts.

Unfortunately, micro-CT shows low contrast for soft biological tissues, in which we are interested. One solution to enhance the contrast is to stain the sample with a contrast-enhancing staining agent (CESA) yielding to contrast-enhanced micro-CT (CE-CT) [58]. This will enable micro-CT imaging to produce quantitative, high-resolution, high-contrast 3D volume images of soft biological tissues, without destroying the specimens.

B) Micro-CT imaging with *in situ* mechanical loading - 4D micro-CT

In situ observation is often desirable because of "non standard" operating conditions, such as high temperature, or because the chronology of the experiment is important [59]. Chronology is a key concern when examining the behaviour of a sample under mechanical loading. Performing *in situ* experiments taking the time into account, with characterization of the microstructure thanks to an imaging technique, such as micro-CT, can provide a global information on the material microstructure evolution. This is known as 4D micro-CT. Guvenilir et al. [60] was one of the first group applying *in situ* high resolution micro-CT on a tensile sample of an Aluminium-Lithium alloy to study its crack closure behaviour. Since then, 4D micro-CT experiments were broadened and were involved in the dynamic study of various environments (temperature, stress, corrosive environment etc.).

As micro-CT is a non-destructive technique, several scans of a single sample can be recorded while the experimental environment is changing with time. This enables to obtain a set of 3D images of the internal microstructure of the material in function of time. The resolution in time will depend on the duration of the scans, which typically ranges from 30 min to nearly 10s for the fastest [59]. To perform *in situ* mechanical loading in tension or compression, and study the deformation behaviour of the sample, *in situ* stages able to be mounted on the micro-CT device were developed. Other stages to study various environment changes, such as high and low temperature deformation, were also designed [59][61].

C) 4D Contrast-Enhanced micro-CT

Detailed characterization of damage and rupture mechanics of arteries is one of the current challenges in vascular biomechanics [12]. Conventional histology is still used for structural analysis of biological tissue, even if it is a destructive technique limited by 2D sections. The development of suitable experimental approaches that enable precise and quantitative 3D structural analysis is, therefore, essential [62]. Performing 4D micro-CT on soft tissues shows some limitations due to the intrinsic low X-ray adsorption of soft tissues and due to the instability of such samples. As they are likely to move during scanning, to avoid ending with a blurry reconstructed image, this motion should be minimized. In addition, the sample is heated during scanning, which should be avoided to keep the properties of the sample. The solution to these issues should be to scan the sample with fast acquisition time. However, this is only possible if the tissue exhibit sufficient absorption contrast which is not the case for arterial tissue.

To overcome this issue, a CESA that binds to components of the tissue can be used to obtain satisfying contrast and allow relevant observations. This will lead to the development of 4D CE-CT, a promising technique which enables to characterize complex mechanical mechanisms of soft tissues.

The first studies identified about contrast agent dates from fifteen years ago. Porcine lungs and mouse embryos were stained with a highly toxic agent, osmium tetroxide, in order to be imaged by X-ray computed tomography [63][64]. Then, Metscher et al. presented several simple and versatile staining methods for micro-CT imaging of animal soft tissues, along with tissue fixation and sample preparation advice [58]. From this research, it was demonstrated that phosphotungstic acid (PTA) and inorganic iodine were the most broadly useful contrast stains. The PTA binds to fibrin, collagen, and fibers of connective tissues [65][66][67]. However, it has the disadvantage to induce significant tissue shrinkage due to its strong acid behavior.

More specifically about the tissue of interest in this thesis, Helfenstein-Didier et al. [12] performed a 4D CE-CT test using solutions of diluted sodium polytungstate (SPT) as CESA to increase the absorption coefficient of the elastin sheets of the medial layer in arterial tissue. On figure 2.16, the effect of the CESA penetration in function of the staining time and the concentration of the solution is well illustrated. After 48 hours, the staining is still not completed, the CESA was not able to penetrate through the whole tissue. This means that the contrast agents nature, concentration and penetration time are parameters important to control and to study.

The CESA used in this work is an Halfnium-substituted Wells-Dawson polyoxometalates (Hf-WD-POM), which main application was as catalyst before being tested and validated as a contrast agent for micro- or nano-CT imaging [67]. It has been used for visualization of cartilage tissue, bone marrow compartment and muscle [68]. Among other

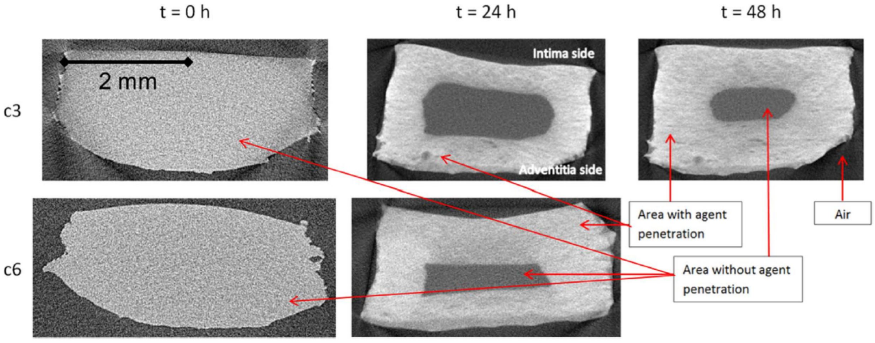

Figure 2.16: Micro-CT images of longitudinal arterial tissue sample at t=0 and after 24 and 48h of staining in a concentrated (c3=15g/l and c6=30g/L) solution of SPT [12].

advantages, Hf-WD-POM does not alter tissue integrity of stained sample and allows 3D multi-tissue visualization. Recent studies focused on the characterization and alternatives based on this CESA, which would be more cost effective, more straightforward and less time-consuming to synthesize [62].

The effect of the staining on mechanical properties of soft biological tissue should be assessed. If the reader is interested in this subject, he/she could be referred to the thesis of Maïté Pétré (UCLouvain) who has worked on this topic.

D) 3D image analysis - Digital volume correlation (DVC)

4D micro-CT imaging is after combined with digital volume correlation method [13][69][70]. In fact, this combination enables to map the full-field 3D internal deformation of a porous structure subjected to, for example, step-wise uniaxial compressive or tensile loading. It could also be used to calculate and map deformations caused by the heating or the freezing of the sample.

Biological tissues present complex anisotropic structure and non-linear response (see section 2.3.2). Therefore, the strain gradients can fluctuate significantly through the thickness of the tissue. In this context, a 3D full-field deformation measurement is required [71]. Digital volume correlation (DVC) is a full-field, contactless technique that provides both displacement and strain maps inside specimens via the comparison of 3D datasets acquired from 4D micro-CT [72].

The first application of DVC for strain mapping of biological tissue was done in bone tissue, then followed by subsequent DVC applications to various hard (e.g. bone [73], tooth [74]) and soft biological tissues [13]. In theory, DVC techniques define a series of regularly distributed discrete calculation points within the reference volume image. Then, the deformed positions of the calculation points are tracked and the full-field displacement vector can be extracted (figure 2.17). Finally, using a proper numerical differentiation approach, the 3D full-field strain can be estimated by differentiating the 3D displacement fields.

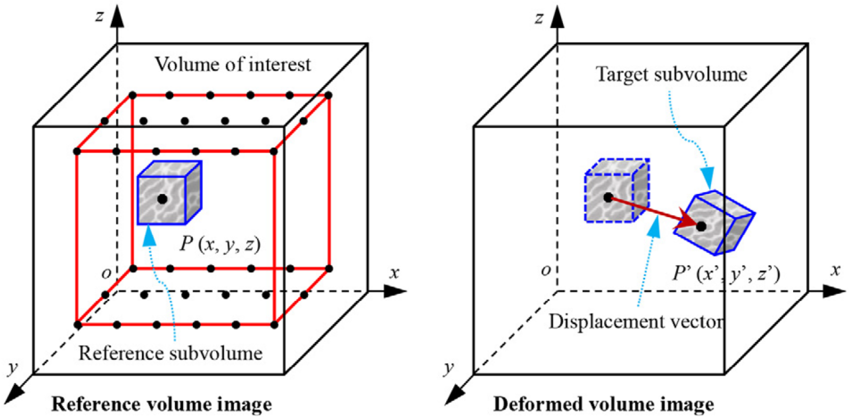

Figure 2.17: Basic principle of DVC: matching the same subvolumes located in the reference and the deformed volume images yields the desired 3D displacement vector [13].

Two DVC methods exist for quantifying continuum-level strain measurements, and they are based on two different approaches; a more local one and a more global one [14]. The first approach, which is a local analysis, is the most commonly used. It consists in dividing the reference and the deformed images into smaller interrogation windows that are then individually correlated. This approach was developed at the beginning of the 1980s, and first applied to solid mechanics in 2D and then extended to 3D applications. Since then, several robust and accurate DVC algorithms have been developed. They are based mainly on cross-correlation and sum of squared differences criteria, with displacement uncertainties ranging between $10^{-}2$ voxel and $10^{-}1$ voxel. The second approach is the more global one. It estimates the displacement fields from pairs of images based on continuous and global field, as commonly used in finite element simulations. Similarly to the first approach, it was first developed in 2D and then extended to 3D, and has been applied with success to solid and cellular materials, such as arteries [71][75]. Figure 2.18 shows the differences between the local and the global approaches described.

Both DVC methods are applicable to porous material and the measured displacements and strains compare well between the two DVC methods [14]. The local approach gives a good compromise between accuracy and computational cost, where the global approach is more accurate and presents less bias but requires more computational time. However, today it is no more an issue since several algorithms exist to preprocess some computation [76]. More details about the different steps behind DVC can be find in appendix C.

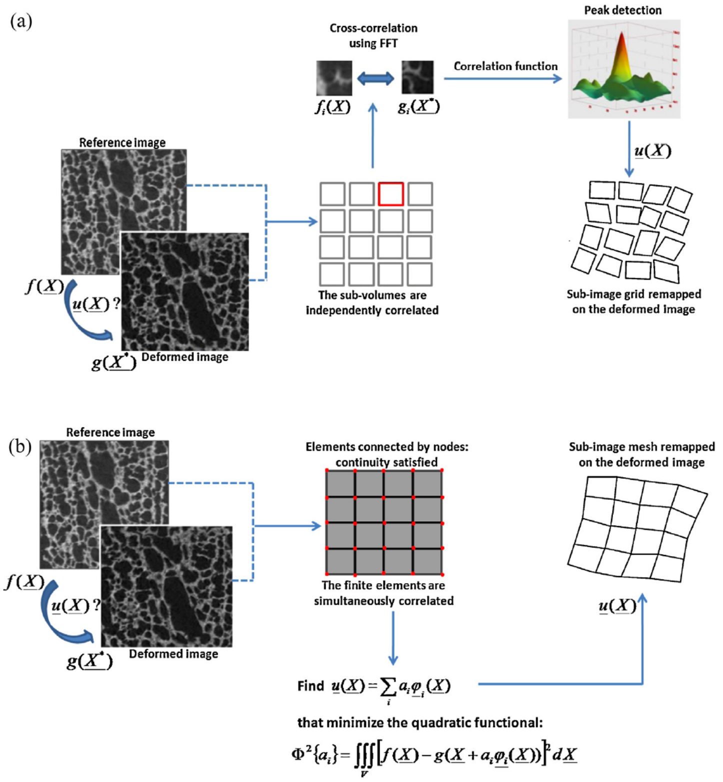

Figure 2.18: Differences between (a) the FFT-based local approach, and (b) the finite element global approach. X and X^* refer to coordinates (in voxels) of the same point in the reference and the deformes state respectively and $u(X)$ is the sought displacement field; f ang g are the grey levels of the initial and deformed volumes respectively [14].

E) Conclusions and perspectives of 4D micro-CT and CE-CT combined with DVC analysis

From all the literature available, several valuable conclusions and perspectives from 4D miro-CT and CE-CT experiments using DVC to analyse the results can be given:

(1) Mechanical properties of the test sample, such as the elastic modulus and the Poisson's ratio, can be determined and related to the geometric structure of the sample visualized by micro-CT.

(2) DVC measurements can allow potential failure mechanisms to be predicted based on the evolution of the maximal principle strain and maximal shear strain. In this manner, effective and reliable failure predictions can be realized via micro-CT imaging and DVC measurements without destroying the sample in practical.

(3) The experimental results can be used for specifying boundary conditions and extracting constitutive parameters for FEM simulations so that they can be performed with higher reliability.

Chapter 3

Problem statement, aim and objectives

Cardiovascular diseases are one of the leading causes of death in the developed world. The need for accurate mechanical characterization of the native arterial tissue, along with synthetic graft materials, is essential and can provide valuable insights for the correct medical treatment to follow. Mechanical characterization of soft tissues, like arterial tissues is very challenging because of its non-linear behaviour, large deformation under loading and the presence of heterogeneity and anisotropy. This thesis focuses on one of the synthetic vascular graft available used to create a bypass in order to re-establish a viable blood flow rate, i.e. Dacron.

Uniaxial tensile testing and planar biaxial testing have already been performed, but they do not fully replicate the *in vivo* physiological loading conditions. Numerical simulations also exist to simulate mechanical behaviour of arterial tissue thanks to the data collected from the two previously mentioned tests. Nevertheless, other methods are required to acquire more accurate data. In this thesis, two of them are developed: the extension-inflation testing and micro-CT imaging with *in situ* mechanical loading (4D micro-CT and CE-CT of Dacron and native tissue, respectively).

The general aim of this thesis was to characterize the mechanical properties of native tissue and Dacron. This has been done by two different processes:

(1) Optimize the protocol of the extension-inflation test, so that it can be further performed on native arterial tissue and synthetic grafts. Due to the lock down because of COVID-19, unfortunately, this part of the thesis could not be completed. Nevertheless, the onset of the work is presented in chapter 4.

(2) Optimize the protocols for 4D micro-CT and 4D CE-CT combined with DVC for Dacron and native tissue, respectively

The objectives of the above mentioned experiments, can be further detailed as follow. Note that objectives written in red could not be performed because of the lock down and should be considered as future work.

(1) Optimization of the extension-inflation protocol:

- Optimize the following aspects of the protocol: the fluid used to apply pressure on the sample and the bath shape, the testing condition (the preload, the axial stretch and the pressure applied, the number of cycles) and finally the strain-mapping to enhance the understanding of the response of the sample
- In a further step, the objective of this optimization would be to test stained native tissue and compare its mechanical properties with unstained native tissue. As native tissue needs to be stained to have enough contrast for CE-CT imaging, it is useful to study its influence on the mechanical properties.

(2) Optimization of 4D micro-CT and 4D CE-CT:

- Optimize the methodology and experimental protocol when working with Dacron.
- Analyse the mechanical properties and anisotropy of Dacron by performing uniaxial testing on several orientations (longitudinal and circumferential).
- Optimize 4D CE-CT for native tissue
- Analyse the failure mechanisms of native tissue and Dacron by calculating strain maps of the sample thanks to the DVC analysis.
- Compare the data of native tissue and Dacron to highlight the differences and similarities in order to better understand its behaviour under mechanical loading and provide feedback for further extension-inflation tests.

Chapter 4

Extension-inflation testing

This experiment could not be completed due to the exceptional circumstances linked to COVID-19. Nevertheless, the preliminary results are gathered here and could be useful for further experiments.

Extension-Inflation testing is of great interest since it replicates the physiological loading conditions of tubular samples very well and preserves the native geometry of the sample. It is an alternative method to planar biaxial testing, since force is applied transmurally and axially.

4.1 Materials and methods

4.1.1 Materials

One sample of native tissue was used to perform the first test. This sample was a sheep femoral artery that was stored in the freezer in a physiological solution until testing. In addition, some tests were done on an unknown synthetic graft material (kindly provided by the lab of Prof. Nele Famaey).

4.1.2 Sample preparation

The native tissue was first thawed in a hot water bath during approximately 20 minutes. The sample had a diameter between 5 to 6 mm and was cut at the right length of 5 cm long. The loose connective tissue present around the artery was removed to avoid to distort results and to enable precise deformation measurements. The synthetic material had a diameter of 6 mm and a length of 5 cm.

4.1.3 Extension-inflation testing set-up

A) Hardware

The triaxial tester (figure 4.1) has been manufactured by ZwickRoell's subsidiary company Messphysik. Extension, inflation and torsion tests can be performed on this device. Extension is achieved via crossheads moving in opposite directions. To generate the inflation pressure, a motor-driven pump is installed at the back of the testing machine. Torsion was not used in this study, but can be achieved by a stepper motor connected to the twistable lower plate of the system. Axial force and inflation pressure were measured by a 20N load cell and a 5 bar pressure transducer, respectively.

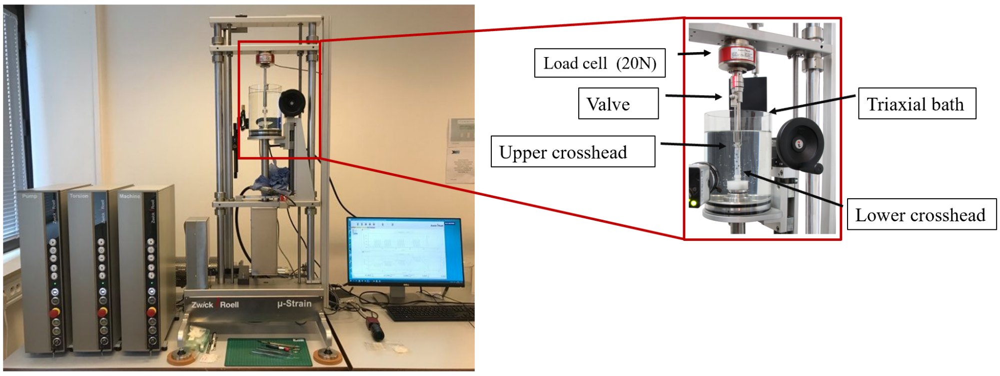

Figure 4.1: Illustration of the triaxial tester used in this thesis and its components.

B) Software

To operate the triaxial tester, the Zwick testXpert II software is used. This software uses a standardized operating platform for all of its applications, so that it can be used on all the material testing devices. The software enables to create an experimental protocol through virtual boxes fixing the preload, the desired force and pressure, the testing speed, the number of cycles. The sofware then plots a graph of the results and is able to export an Excel file with all the information recorded.

The software takes a txt.file as input, where the user can specify the protocol parameter. The entry of this file is devided in two parts: the global test input and the individual loading steps. The global test input contains the axial preload, the pressure preload, the axial preload speed, the pressure preload speed, the axial initial position, the axial loading unit, the pressure loading unit and the sample rate. The user is also able to define the individual loading steps by specifying the name (AF for axial force fixed or PF for pressure fixed), the axial load (in Newton [N] if force controlled and in percents of strain [%] if displacement controlled), the pressure load [MPa], the number of cycles, the axial speed [mm/s] or [%/s], the pressure speed [mm/s].

4.2 Experimental protocol

4.2.1 Optimization of the protocol

As the extension-inflation testing is a relatively new technology, the protocol to correctly use the device is not yet optimized and standardized. This is an issue since, in addition to the lack of literature about this testing method, the published results can hardly be compared due to the different experimental methods adopted. It was, therefore, one of the objectives of this thesis to improve the testing protocol for extension-inflation. The parameters of the protocol highlighted to be optimized are the following:

- **Proper zero adjustment of the axial force and transmural pressure** is an important parameter to look at when setting up the device. A proper zero adjustment of the axial load is to attach the artery or the synthetic graft to the upper crosshead and then setting the axial force to zero [28]. Thereafter, the sample can be fixed to the lower crosshead. For proper zero adjustment of the pressure, the valve on the upper shaft is opened. Then, the bath is filled in until the water reaches the valve level. The pressure is then set to zero and the valve is closed to measure the transmural pressure. The specific terms used are illustrated on figure 4.1.

- **The mounting system** should also be optimized as it is difficult to mount the cylindrical sample in a satisfactory manner to avoid leaking at high pressure. If the sample is leaking at the fixed extremities, it may result in an incomplete set of data, unless the pressure is high enough.

- **The fluid** present in the triaxial cell is another critical parameter to take into account. The fluid must be translucent, cannot interact with the sample and must replicate physiological conditions of the blood (viscosity, pH, osmolarity, ion concentration,...). There is nearly no literature concerning the extension-inflation testing of synthetic grafts. However, when testing an artery, a possibility for the fluid is phosphate-buffered saline (PBS) [28]. This water-based salt solution is typically used in biological research and matches the osmolarity and ion concentrations of the human body. Another fluid used in literature is a Tyrode solution kept at 37°C [77]. Any physiological solution is acceptable, provided that the optical technique is calibrated to take the fluid into account in order to analyse and work with the sharpest possible image [78].

- **The shape of the triaxial cell** is also important. A camera can be used to track the diameter change of the sample or it can be used to perform marker tracking and recording the elongation of the sample, thus obtaining the necessary displacement data. Therefore, in both cases, diffraction of the light must be minimized to obtain a clear image.

4.2.2 Preparations

First of all, the software and the machines governing the axial displacement, the pump displacement and torsion were started. Then, the upper part of the sample was mounted on the 3D printed mounting pieces, tightened by a clamp ring (figure 4.2). The proper zero adjustment of the axial load and pressure is crucial for extension-inflation tests. The zero adjustment of the axial load was achieved after fixing the upper part. For proper adjustment of the pressure, the mounting of the sample was completed by fixing the lower part, the valve was opened and the bath was filled with water until it reached the level of the valve (figure 4.1). Once the valve was submerged by water, the pressure was set to zero and the valve was closed.

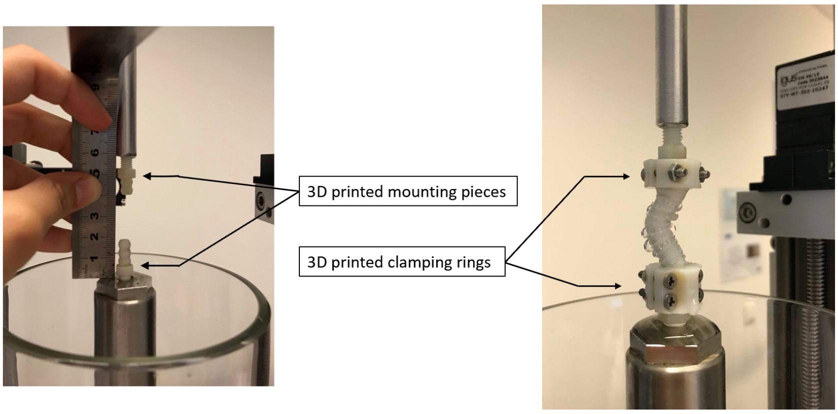

Figure 4.2: Mounting system of the triaxial tester.

4.2.3 Preload

The definition of the preload varies much in literature. The main idea behind the different definitions is that it represents all the factors that contribute to passive wall stress (or tension) at the beginning of contraction, which corresponds to the end of diastole [79]. Nevertheless, the basis for the definitions is the Law of Laplace, stated as follows for a thin-walled spherical structure

$$2\sigma_\theta hl = P(2rl)$$

$$\sigma_\theta = \frac{Pr}{h}$$

where σ_θ is the circumferential stress, P is the inflation pressure and r the inner radius, l is the length of the vessel, and h is the thickness of the vessel wall (figure 4.3). In the literature, the preload is fixed either by a strain or by a percentage of the tensile strength [80]. In our case, based on previous experiments, the preload applied was 0.05N for both materials at a rate of 0.3 mm/s for the native tissue and at a rate of 0.01 mm/s for the synthetic material.

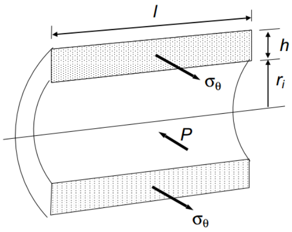

Figure 4.3: Illustration of the vessel with the terms used in the definition of Laplace's law [6].

4.2.4 Testing protocol

A) Native tissue

The testing protocol applied on the native tissue sample was displacement-controlled, meaning that the axial displacement was fixed to a specific value and that the force experienced by the sample to reach this displacement, has been registered.

The behaviour of the sample was evaluated at two different pressures: the physiological pressure of 100 mmHg (0.013 N/mm^2) and the supra-physiological pressure of 200 mmHg (0.026 N/mm^2). The second range of pressure tested is the case of an hypertensive patient or during hard physical activities. To reach these pressures, the pump displacement was set at a speed of 1 mm/s.

At the beginning of the test, the preload was applied and the next steps of the protocol were repeated for several levels of strain. The levels of strain were 15%, 25%, 35% and 45%. These strain levels were reached at a speed of 0.6 %/s. For every strain level, 2 sets of five cycles were performed, one at low pressure and the other at higher pressure. For each set, five cycles were needed to precondition the sample and have accurate results during the last cycle. Between each set of cycles, the preload was reached in order to keep a better control of the results.

B) Synthetic graft

The testing protocol applied on the synthetic graft sample was force-controlled, meaning that the axial displacement was fixed at a specific value of force and the axial force to remain at this fixed axial displacement under pressure has been registered.

Similarly to the native tissue, the behaviour of the sample was evaluated at two different pressures, the physiological pressure of 100 mmHg (0.013 N/mm^2) and the supra-physiological pressure of 200 mmHg (0.026 N/mm^2). To reach these pressures, the pump displacement was set at a speed of 1 mm/s.

At the beginning of the test, the preload was applied and the following steps of the protocol were repeated for several axial forces. The axial forces applied were 1N, 2N, 3N and 4N. The displacement of the crosshead to reach these forces was set at a speed of 0.05 mm/s. For each pressure level, four set of five cycles were performed. For each of the set, the axial force applied was reached during the first cycle, then the displacement of the crossheads was fixed. The four other cycles evaluated the variation of the axial force with the pressure. Five cycles were needed to precondition the sample and to have accurate results at the last cycle.

4.3 Results and discussion

4.3.1 Native tissue

Figure 4.4 shows the results of the extension-inflation experiment on native tissue. Leaking is clearly visible on this graph, since the displacement of the pump, meaning the displacement of the motor-driven pump controlling the fluid rate going through the sample and therefore the pressure applied to it, is continuously increasing. This leaking can come from a hole in the native tissue caused by a branch of the artery that was not well stitched. Another cause of this leaking could come from the mounting. This is indeed a parameter to yet optimize.

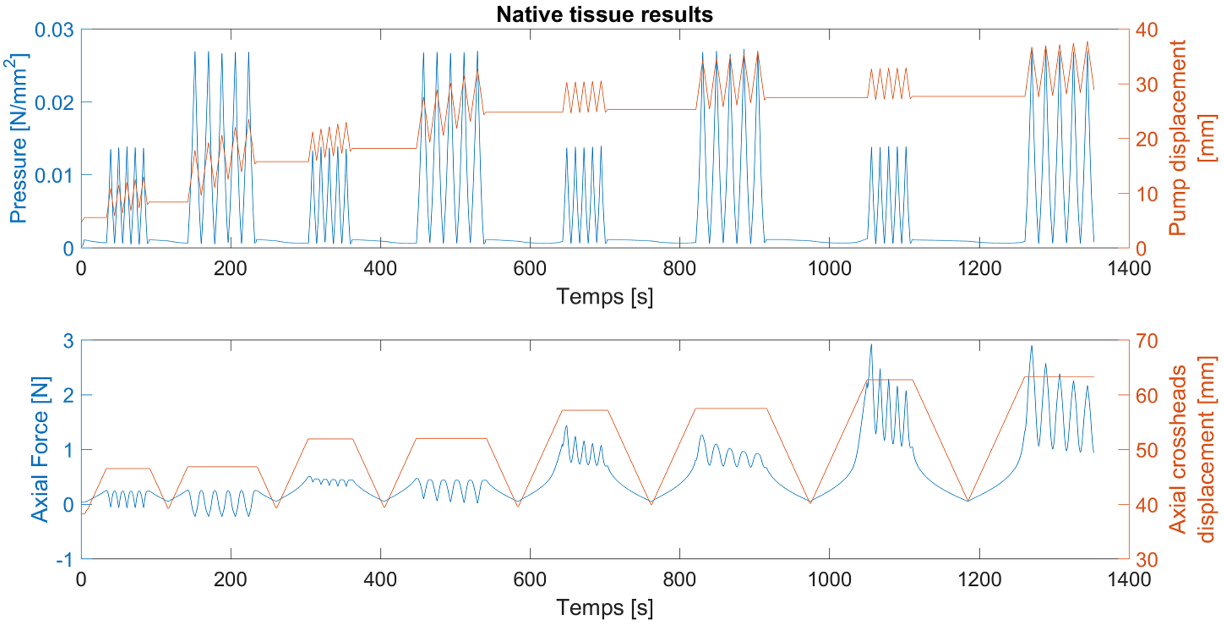

Figure 4.4: Results of the applied displacement-controlled protocol on the native tissue sample. The upper graph represents the applied pressure (blue) and the pump displacement (red) for each cycle. The lower graph represents the axial force needed (blue) to reach a specific displacement (red).

Concerning the level of strain tested, the axial force of the first and second set of cycles oscillated around 0N. Therefore, it can be concluded that reaching 15% of strain is not of great interest compared to the other values of 25-35 and 45 %. A further protocol should be more focused on the level between 25 and 45% of strain.

4.3.2 Synthetic graft

For this sample, a force-controlled protocol was chosen. The issue with the previous displacement-controlled protocol is that the sample was so stiff that it was not possible to reach 3% of strain without applying less than 20N (value of the load cell of the triaxial tester) of axial force. This stiffness could be caused by the age of the specimen since the sample used for the experimental protocol optimization was a trial sample. The protocol should therefore be tested with fresh samples to acquire more accurate results.

Figure 4.5 shows the results of the force-controlled protocol tested on a synthetic graft sample and its relaxation can be observed. After the first cycle of each set, which consist in reaching the fixed axial force chosen, there is a large difference with the value of the second cycle. This difference becomes larger as the number of cycle increases, and converges for the fourth and the fifth cycle. As the axial force applied is increased, this difference also increased. This is a typical behaviour of sample relaxation (see section 2.3.3) which was also observed in the 4D micro-CT experiments.

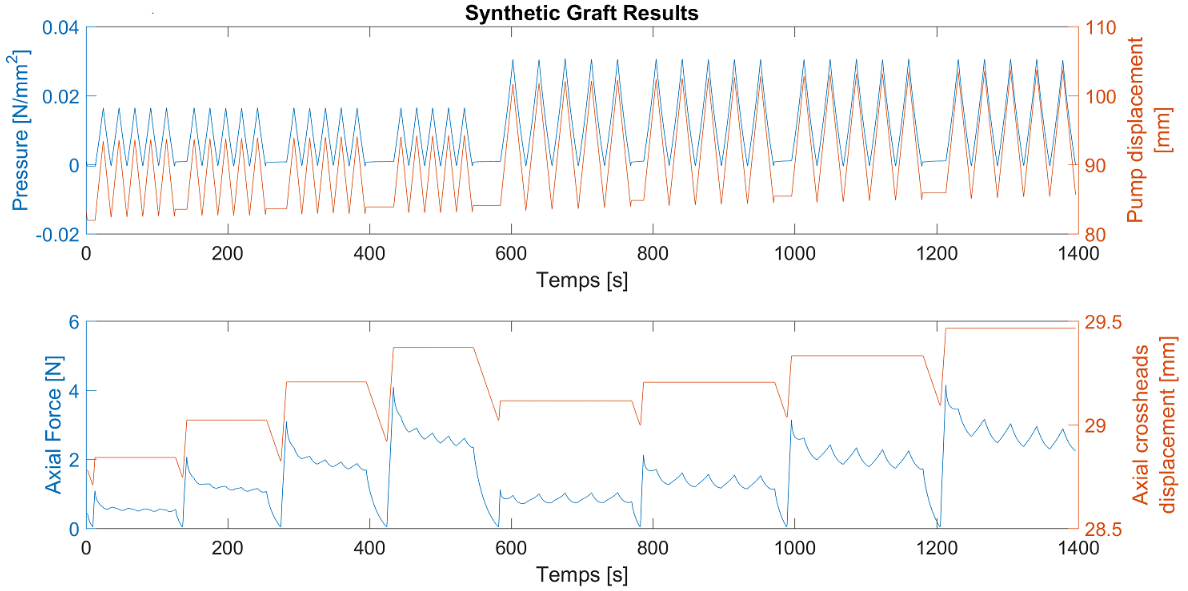

Figure 4.5: Results of the applied force-controlled protocol on the synthetic graft sample. The upper graph represents the applied pressure (blue) and the pump displacement (red) for each cycles. The lower graph represents the axial force (blue) when the displacement is fixed to the first value of the force reached (red).

4.4 Conclusion

Our preliminary tests revealed limitations in the currently used protocol, and highlighted the need to further optimize the testing protocol. Some suggestions to improve the protocol are proposed on table 4.1.

Table 4.1: Summary of suggestions to optimize the testing protocol for extension-inflation.

	Current limitations	**Suggestions**
Mounting system	Leaking with the wavy 3D printed mounting pieces and semi-cylindrical clamping rings screwed together around the sample	Flatten the lateral surface of the mounting piece and use a clamping ring with Teflon around to fully match the shape of the sample
Fluid	Water is used which, does not have the same viscosity as blood	A blood mimicking fluid should be used and an example of fluid could be a solution composed of 47.38% water, 36.94% glycerol, and 15.68% sodium iodide salt, resulting in a dynamic viscosity of 4.31±0.03 cP [81]
Bath shape	Cylindrical shape, which causes diffraction of light	Square shaped batch to minimize diffraction of light thanks to flat sides

After protocol optimization, the behavior of a synthetic graft sample should be investigated to determine if its high stiffness was due to degradation of the sample or if it is an intrinsic property. This would be useful to establish whether a displacement-controlled protocol could be performed on synthetic sample. In that way, native tissue and synthetic graft would be tested with a displacement-control protocol, and this would be more accurate to compare both.

The last objective, which was to test stained native tissue and compare its mechanical properties with unstained native tissue, could not be achieved. As detailed in the next chapter, the staining of native tissue is a interesting field of interest and unavoidable to acquire good quality micro-CT scans of native tissue. Hence, this could be an attractive area of research for further work.

Chapter 5

4D micro-CT of Dacron and 4D CE-CT of native tissue

In order to characterize the mechanical properties of Dacron and of native tissue, 4D micro-CT and 4D CE-CT, respectively, were performed. As this is a new experimental setup, the first objective was to optimize the testing protocol such as identifying the correct number of scans, how to handle the Dacron sample as it has a folded structure and the staining of the native tissue. The second objective of this test was to optimize the local strain mapping and DVC analysis allowing to identify failure mechanisms and to compare data of both materials.

5.1 Materials and methods

5.1.1 Synthetic graft and native tissue

Dacron was used as synthetic graft. This graft material is currently clinically used in bypass surgery to replace an obstructed artery.

The native tissue tested was extracted from the upper part of a porcine descending aorta, as shown on figure 5.1. This tissue was obtained from the slaughter house.

5.1.2 Sample preparation

Dacron was received as a folded tube of 6 mm of diameter and 40 cm of length. From this, two samples were prepared to evaluate the different stresses acting on the artery wall (cfr. Appendix B). One was tested in the longitudinal direction (further referred to as Dacron longitudinal), and the other was tested in the circumferential direction (further referred to as Dacron circumferential). Dacron longitudinal was prepared from a tube of 26 mm long that was cut and opened longitudinally in order to have a rectangle of 26x19 mm (figure 5.3). Similarly, Dacron circumferential was made from a tube of 8 mm, cut and opened

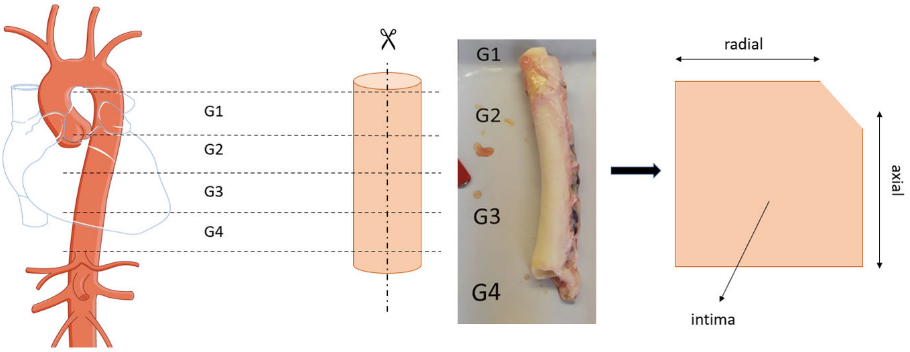

Figure 5.1: Dissection of the aorta [15].

longitudinally to obtain a rectangle of 8x19 mm (figure 5.4).

The native tissue sample was stored in the freezer at -80°C after dissection. Few days before testing, the sample was thawed and was stained during five days in a solution of 3.5% of Hf-WD POM (dissolution of 35 mg/mL Hf-WD POM in PBS). The sample was a rectangle of 10 mm of width, 3 mm of thickness and 35 mm of length (figure 5.5).

5.1.3 Micro-CT image acquisition

The scans were taken using a Phoenix NanoTom M (GE Measurement and Control and Solutions, Germany). The target is composed of tungsten coated with diamond.

For both Dacron samples the system was operated at a voltage of 40 kV and a current of 850 mA. The exposure time was 500 ms, and 1200 images were acquired with a voxel size of 9 μm. No filter was applied and a scan time of 10 min was sufficient to have a good image quality.

For the aorta, the system was operated at a voltage of 60 kV and the current was of 567 μA. The exposure time was 500 ms, and 1800 images were acquired with a voxel size of 9 μm. No filter was applied and the time of the scan was 15 min.

5.1.4 Mechanical loading protocol

The combination of the mechanical loading with the micro-CT imaging provides a clear visual interpretation of how the properties of the materials change under different loading conditions. The testing stage used in this study was a CT5000-TEC model (Deben, Germany) and is controlled with the MICROTEST tensile stage control software. This tensile stage provides a force range of tensile and compression up to 5kN and resolutions down to 25 mN [16]. The loading stage is illustrated in figure 5.2.

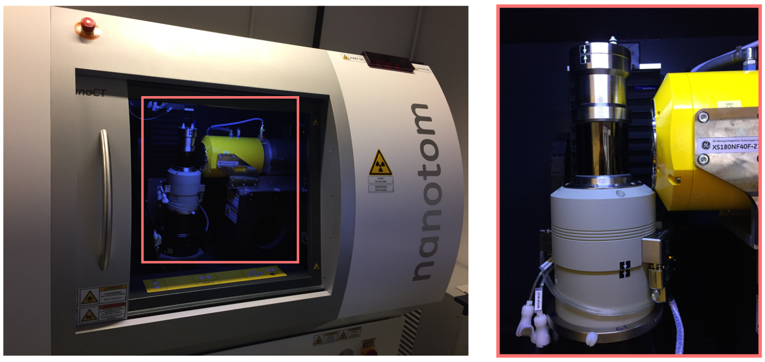

Figure 5.2: Tensile loading stage: Deben MICROTEST - CT5000-TEC [16].

A) Dacron

- **Dacron longitudinal** was tested in two parts due to its folded structure. First (i.e. Dacron longitudinal part I), it was mounted in the loading stage by attaching the extremities between clamps so that the sample was initially unstressed (figure 5.3). At zero-strain, two scans were performed with a translation of the stage of 0.1 mm in the z direction between the two scans in order to perform a zero-strain test and evaluate the accuracy and precision of the DVC analysis. This will be detailed in the following section 5.1.5. Then, the sample was prestretched to study its elastic behavior, which is the behaviour expected within the body. To do so, it was elongated until a total of 10 mm of extension at a rate of 0.1 mm/min. A scan of 10 min was performed each 0.2 mm of displacement, resulting in a total of 49 scans. One last scan was acquired the next day on the same sample in order to assess the relaxation behaviour. In total 52 scans were realized for this part of experiment.

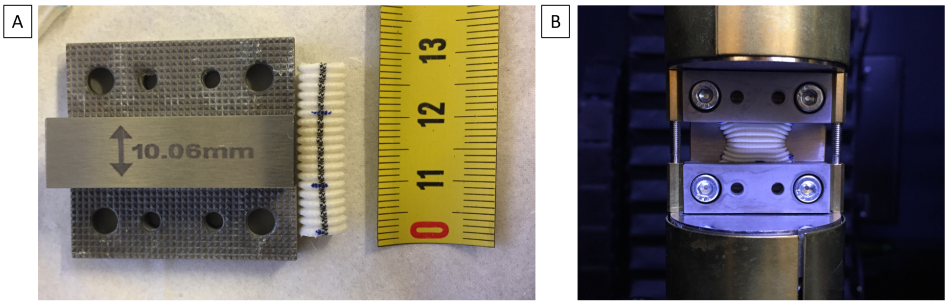

Figure 5.3: Dacron longitudinal: (A) Sample preparation and dimensions and (B) unstretched mounting of the sample

In the second part (i.e. Dacron longitudinal part II), the sample was plastically deformed to assess its intrinsic mechanical properties. The same sample was therefore initially prestretched by hand so that its structure was already slightly unfolded when remounted between the clamps. A first scan was performed before applying any displacement to acquire the reference state. Then, the sample was elongated at the same speed of 0.1 mm/min. Less scans were taken in the beginning of the experiment since it was overlapping with the end of the previous tests. Therefore scans were performed every 0.3 mm of displacement resulting in 8 scans for this first step. In a second step, the displacement between scans was decreased down to 0.2 mm and 23 scans were taken at this rate. In total, for this second part of the experiment, the sample was stretched until a maximum of 7 mm of displacement and 32 scans were taken.

- **Dacron circumferential** was mounted with the folds perpendicular to the clamps (figure 5.4). Two first scans were performed at zero displacement with 0.1 mm of vertical translation between them in order to perform the later detailed zero-strain test. Then, it was displaced at a speed of 0.1 mm/min and scanned each 0.2 mm of displacement until 26 scans were realized. The sample then rested all night, and the experiment continued the next day. The next day, the sample continued to be elongated at the same speed of 0.2 mm, but the space between scan was increased. Five scans were performed each 0.4 mm of displacement. In total, the maximum displacement was 7 mm and 32 scans were acquired.

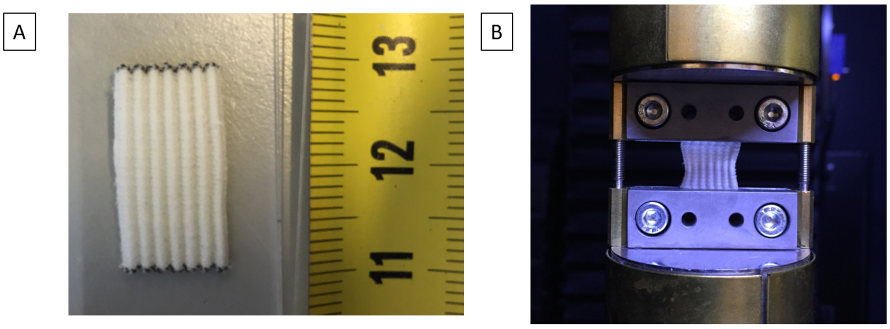

Figure 5.4: Dacron circumferential: (A) Sample preparation and dimensions and (B) unstretched mounting of the sample.

B) Aorta

The aorta sample was only tested in the longitudinal direction. After being mounted between the clamps of the loading stage (figure 5.5), two scans at zero displacement were acquired to perform the zero-strain test. Between these two scans, the loading stage was translated 0.1 mm in the z direction. Then, the sample was elongated at a speed of 0.1 mm/min and scanned every 0.2 mm of displacement. After 32 scans and a maximum displacement of 5.4 mm, the filament broke and had to be replaced. After the filament replacement, a last scan was performed.

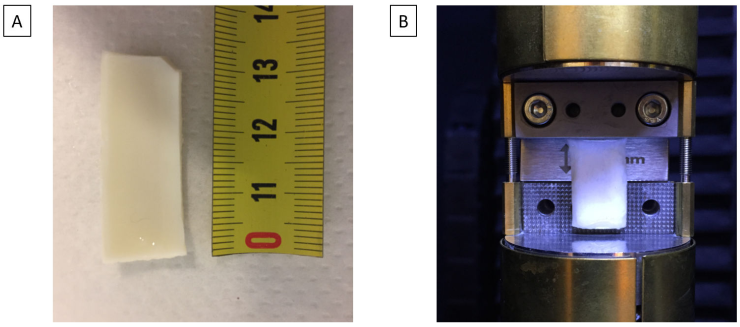

Figure 5.5: Aorta: (A) Sample preparation and dimensions and (B) unstretched mounting of the sample.

C) Stiffness of Dacron longitudinal and Dacron circumferential

The stiffness of Dacron was evaluated by plotting the true stress-strain curves of the two samples and calculating the slope of the linear portion of the curve. The *true* stress, σ_T, and the *true* strain, ϵ_T, were calculated using MATLAB R2016a. Assuming material incompressibility, the *true* data can be related to the *engineering* data as follows:

$$\sigma_T = \frac{F}{A} = \sigma_E(1+\epsilon_E), \;\; \epsilon_T = ln(1+\epsilon_E),$$

where $\sigma_E = \frac{F}{A_0}$ and $\epsilon_E = \frac{\mathit{\Delta} d}{d_0}$ are the *engineering* stress and strain, respectively. For comparison, the slope was calculated for both curves at 45% of strain.

D) Anisotropy

Dacron longitudinal and Dacron circumferential were tested to compute the difference in directional response of the material, i.e. the degree of anisotropy. The anisotropy index (AI) is the difference in stiffness between the directions divided by the average stiffness [82]:

$$AI = \frac{E_c - E_l}{E_{av}}, \quad where \;\; E_{av} = \frac{E_c + E_l}{2},$$

where E_c and E_l are the stiffness in the circumferential and longitudinal directions, respectively.

5.1.5 Image analysis and DVC

To analyse the micro-CT images, two softwares were used. CT-An (Bruker MicroCT, Belgium) was used to crop the data in order to remove the sample holder from the set of images. Avizo (ThermoFisher Scientific, Germany) enabled rendering on 3D data sets and a qualitative analysis of the failure mechanisms. It was used to calculate local strain maps of the sample thanks to the DVC module and interactive visualization tools.

A) Digital volume correlation (DVC) analysis

DVC for 3D internal deformation measurement consists of the following three consecutive steps (for detailed explanation of each of the steps, the reader is referred to appendix C):

(1) Volumetric image acquisition: acquisition of two micro-CT volume images of the test sample before and after loading.

(2) 3D displacement field calculation: Specify the interrogated points within the reference volume image and track their corresponding locations in the deformed volume to extract their 3D displacement vectors.

(3) 3D strain field estimation: Calculate the strain components from the displacement vector field using an appropriate numerical differentiation approach.

DVC analysis was applied to a region of interest (ROI) of the sample. The ROI chosen for the different samples, i.e. Dacron longitudinal part I, Dacron longitudinal part II, Dacron circumferential and aorta are square of 320x210x320 voxels, 470x210x470 voxels, 370x240x370 voxels and 250x415x250 voxels, respectively. The location of the extracted ROIs is shown in figure 5.6.

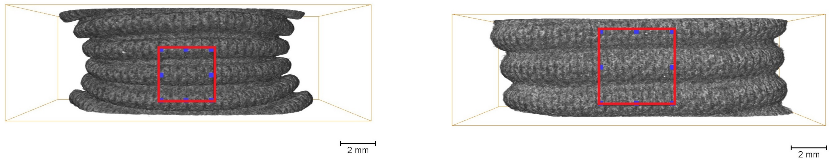

(a) Dacron longitudinal part I (b) Dacron longitudinal part II

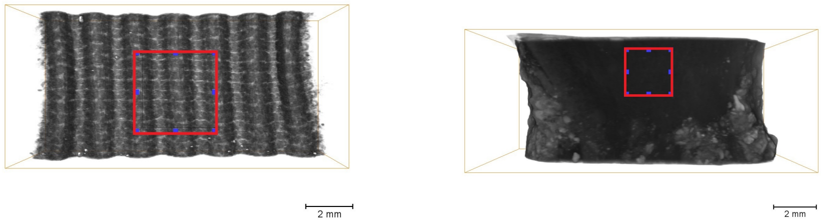

(c) Dacron circumferential (d) Aorta

Figure 5.6: Location of the ROIs (red square) on the different samples.

Two methods have been used to compute 3D displacements and strain fields between a reference image and a deformed image, i.e. after elongation of the specimen (cfr. section 2.5.5). In this work, the local approach has been used to initiate the global approach. The different steps of the methodology are the following:

(1) **Preparation of the DVC analysis:** Before DVC analysis, it is important to choose the optimized subset size for the grid as it has an impact on the DVC

resolution. If the subset size is too small, noise effects are more susceptible to appear. However, if the subset size is excessively large, it may result in an inadequate spatial resolution of the strains [83].
In order to evaluate this optimal grid sub-volume size, the "Radial Autocorrelation" module is applied to the reference image. This module will autocorrolate the reference image with itself and calculate the probability that two points translated by a distance of h belongs to the same phase. By plotting the result of this module, the distance at which autocorrelation is no more possible can be evaluated. The rule of thumb is that the subset size is three to four times this distance.

(2) **Initialization using local DVC:** After having registered the reference and deformed images, the "Digital Volume Correlation" module is set to local approach port in order to initialize the displacement of the further global analysis. A coarse grid is adapted to the sample and the local DVC analysis is performed with a correlation filter of 0.7 and the translation as well as the rotation transformation are taken into account.

(3) **Generation of the tetrahedral grid:** To apply the global DVC, a reference mesh is required. To construct this mesh and adapt it to the complex shape of the samples, several modules are applied to the reference image volume. The first one is the "Interactive thresholding" module, which produces a binarized image. Then, the "Closing" and "Erosion" modules are applied to, firstly, join small objects to larger ones and, secondly, to remove the isolated points and discard border pixels. Finally, a surface is generated thanks to the "Generate surface" module using a smoothing extent of 2. A tetrahedral grid can then be generated using the optimized subset size estimated before.

(4) **Global DVC:** The last step is to apply the Global DVC by switching the DVC approach port to global. Using the reference mesh just constructed and initializing the displacement by the local approach, the displacements and strains are calculated.

B) Zero-strain test: accuracy and precision analysis

To evaluate the accuracy of the DVC analysis or the impact of the noise on the images, a zero-strain test is performed. It consists in collecting two repeated scans with only a rigid body translation between them. In this work, a translation of 0.1 mm (11.1 voxel) was realized. The two scans can be different due to noise or motion artifacts. The translation between the scans aims to differentiate the effect of the algorithm with the effect of the imaging noise.

In a first step, the results of the preparation of the DVC analysis, i.e. the results of "Radial Autocorrelation", module were studied in order to choose the right subset size for the global DVC. Then, the strain resolution was investigated by applying the DVC algorithm to the volume after rigid body translation and calculating the precision (mean) and accuracy (standard deviation) of the resulting strain maps [83].

C) Incremental DVC

When large deformations occur, the correlation between the reference and the deformed image can be insufficient so that conventional DVC analysis fails to track the movements of the material point. Indeed, it can yield to unreliable displacement measurement. The term "decorrelation" will be further used to refer to this insufficient correlation between two images.

In this work, three different methods of incremental DVC [17] were assessed on Dacron longitudinal. The three methods are illustrated in figure 5.7. The first method used always the same fixed reference image volume. This way, the maximal displacement before having too large between the reference and deformed image can be evaluated. The second method, known as "sequential" incremental DVC, selects the deformed volume image in the previous correlation as a new reference volume image in the current correlation. The third approach, referred to as "preconditioned" incremental DVC, updates the reference volume only when severe decorrelation is present in the current deformed volume image. To evaluate when the reference volume should be updated, the results of the first method were analysed.

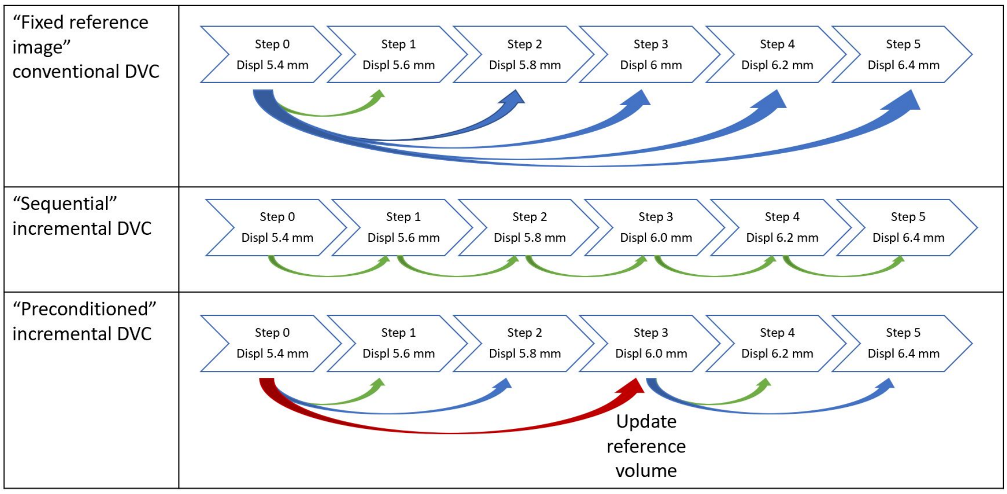

Figure 5.7: Scheme of three incremental DVC method tested in this thesis for Dacron longitudinal: the "fixed reference image" conventional DVC, the "sequential" incremental DVC and the "preconditioned" incremental DVC (adapted from [17]).

A last approach that was not tested in this work due to technical restrictions, but that could be interesting to compare with, is to directly use the module implemented in Avizo named "Incremental Global DVC" [84]. This module performs incremental DVC analysis for a series of five deformed image, using either a small strain or a large strain approach.

After the analysis of the three methods, the one which was the most adapted to this work has been applied to Dacron circumferential and the aorta sample.

5.2 Results and discussion

5.2.1 Microstructural changes during loading - visual inspection

A) Dacron

Figure 5.8 represents several steps of the elongation of the two Dacron samples. During part I of the tensile test for Dacron longitudinal, the unwrapping of the folded structure can be observed. This waviness or folds enable the graft to have a large elasticity in the longitudinal direction. With increasing displacement, during part II of the experiment, the fibres are elongated longitudinally until plastic deformation. The structure is completely unwrapped and will not come back to its initial position. For Dacron circumferential, the unwrapping of the sample as well as the elongation of the fibres until plastic deformation can be observed. A similar trend between the two directions can be assumed with an elastic and a plastic portion.

An anisotropy between the two orientations of the sample is visible. Dacron circumferential was already completely unwrapped at 7 mm of displacement while Dacron longitudinal was still folded at 10 mm of displacement. This can be explained by the specific orientation of the yarns. In addition, for both orientations, necking is identified by the decrease in the cross-sectional area of the specimen. This can assume a localization of the strain in a specific region of the specimen, which will be further analysed with the DVC analysis.

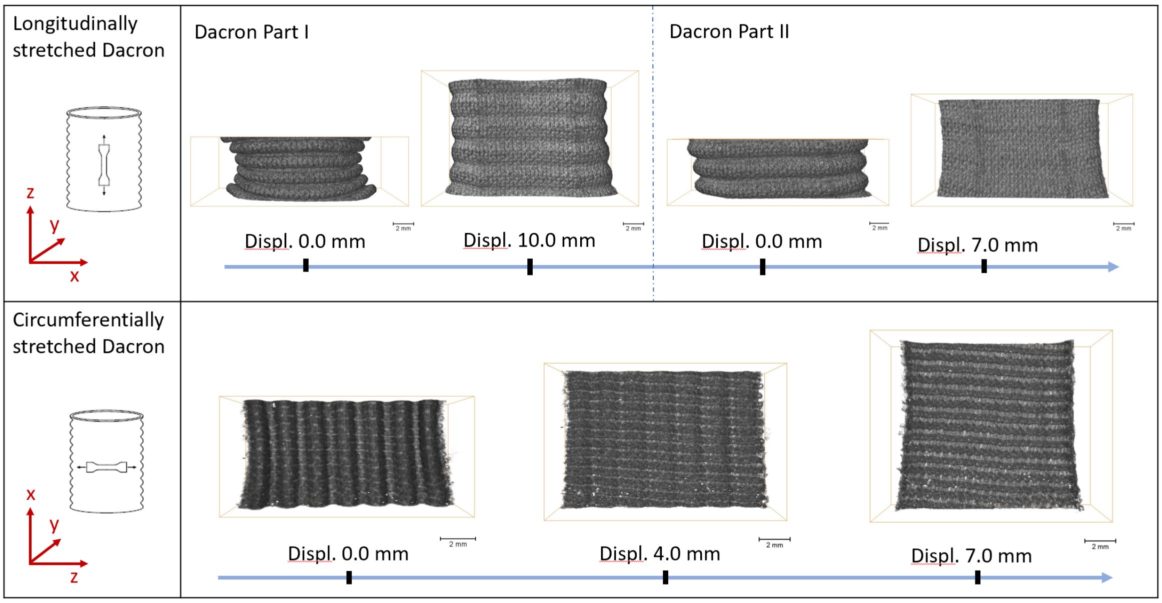

Figure 5.8: Visual inspection of microstructural changes during loading of the two different Dacron samples.

On figure 5.9, the alignment of the yarns is zoomed. There are two kinds of Dacron graft: woven and knitted. The graft analysed in this thesis is a knitted graft, as it is formed by looping fibres together, which is referred to as the velour technique. By comparing the two existing model of a knitted graft (warp or weft) on figure 5.9c with the figures 5.9a and 5.9b, the characteristic loops along the length of the fabric can be distinguished. The extension in the circumferential direction (fig. 5.9b) emphasize the visibility of these longitudinally yarns loops. Therefore, our sample can be classified as a warp knitted Dacron graft.

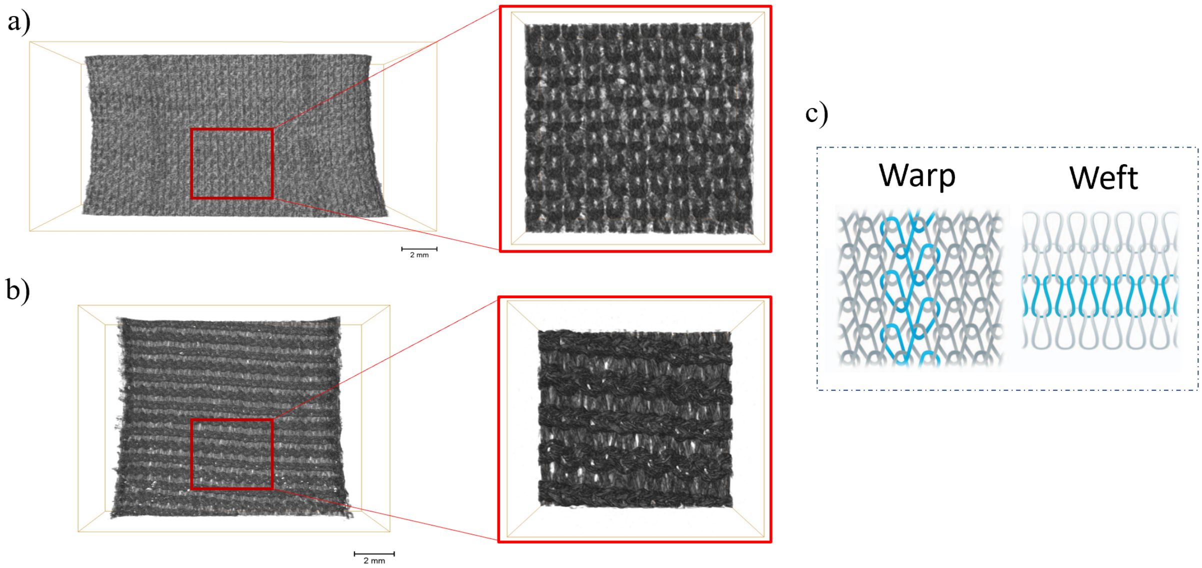

Figure 5.9: Visual characterization of Dacron microstructure: a) Zoom of the microstructure of Dacron longitudinal and (b) Dacron circumferential compared with (c) the reference model of the warp and weft knitted Dacron graft.

B) Aorta

Figure 5.10, shows three different steps of the uniaxial tensile test performed on the aorta sample. The darker area in the center of the xy cross-section means that contrast agent could not completely penetrate through the tissue and therefore, the staining could not completely be achieved. A lack of spatial resolution can also be noticed by the relatively blurry images containing small amount of details. These observations already bring the supposition of a non-negligible error during the DVC analysis. On this cross-section of the aorta, the thinning in the thickness of the native tissue is visible. Looking at the front view of the aorta sample, connective tissue is apparent. This tissue has an important role and must be taken into account for realistic estimation of the arterial wall stress [85]. The necking of the aorta is less visible compared to previously studied Dacron.

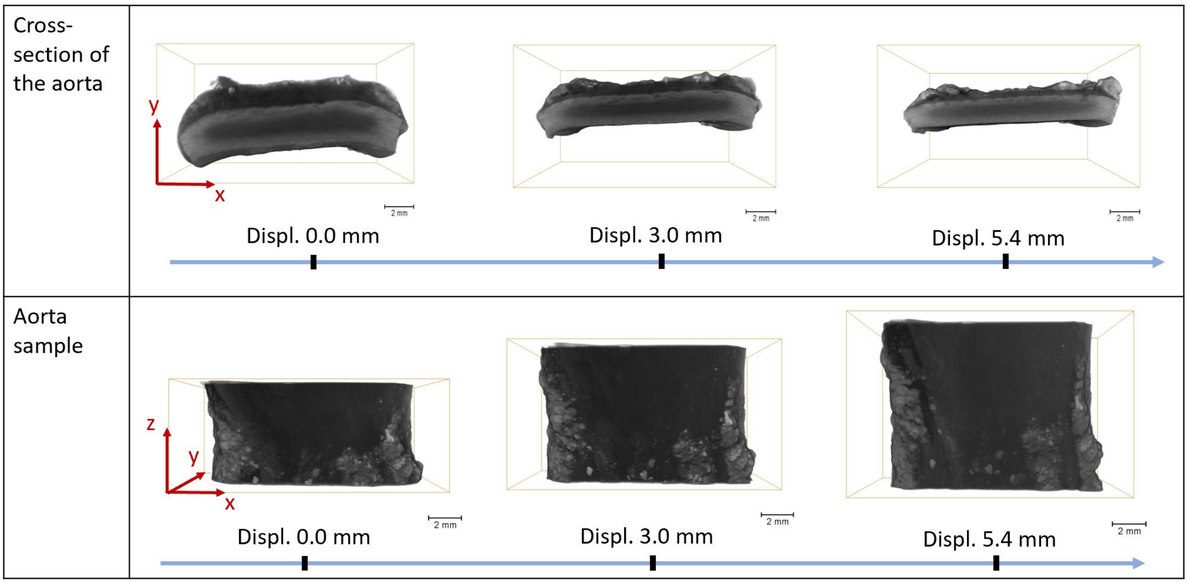

Figure 5.10: Visual inspection of microstructural changes during loading of the two different Dacron samples.

5.2.2 Mechanical properties

A) Dacron

- **Force versus elongation**

  The curves of the force versus the elongation of all the samples tested are gathered on the same graph in figure 5.11. The first features to be noted are the jumps in the blue curve of the Dacron longitudinal (circled in black). These jumps are due to a lack of sensitivity of the system. In fact, as the tensile stage provided a tensile force range up to 5 kN, when only reading out with several newtons the accuracy of the system was not efficient enough. These jumps were corrected by hand by vertically translating the curve to give the purple "modified Dacron longitudinal" curve.

  On this graph, the two parts of the elongation of the Dacron longitudinal are apparent. "Dacron Part I" corresponds to the unfolding of the folded structure. The force remained around 0 N for an elongation up to 10 mm, meaning that the sample was being elastically deformed but the material itself was not deformed. "Dacron Part II" corresponds to the evaluation of the intrinsic mechanical properties of the material. At a maximal elongation of 17 mm, the sample was completely unfolded and started to plastically deform.

  Dacron circumferential did not replicate the same behaviour as Dacron longitudinal. The force increased rapidly with the displacement. For an elongation of 7 mm of displacement, the force reached nearly the same values as the Dacron longitudinal for an elongation of 17 mm. The anisotropy in the microstructure of the graft explains the difference between the two orientations of the sample. The anisotropy will be further developed in the next section.

The relaxation of the samples after each scan is taken into account and is represented by the drops in the force on both figures 5.11 and 5.12. During the scanning time, which was of 10 minutes for the Dacron samples, the force decreased for the same level of elongation.

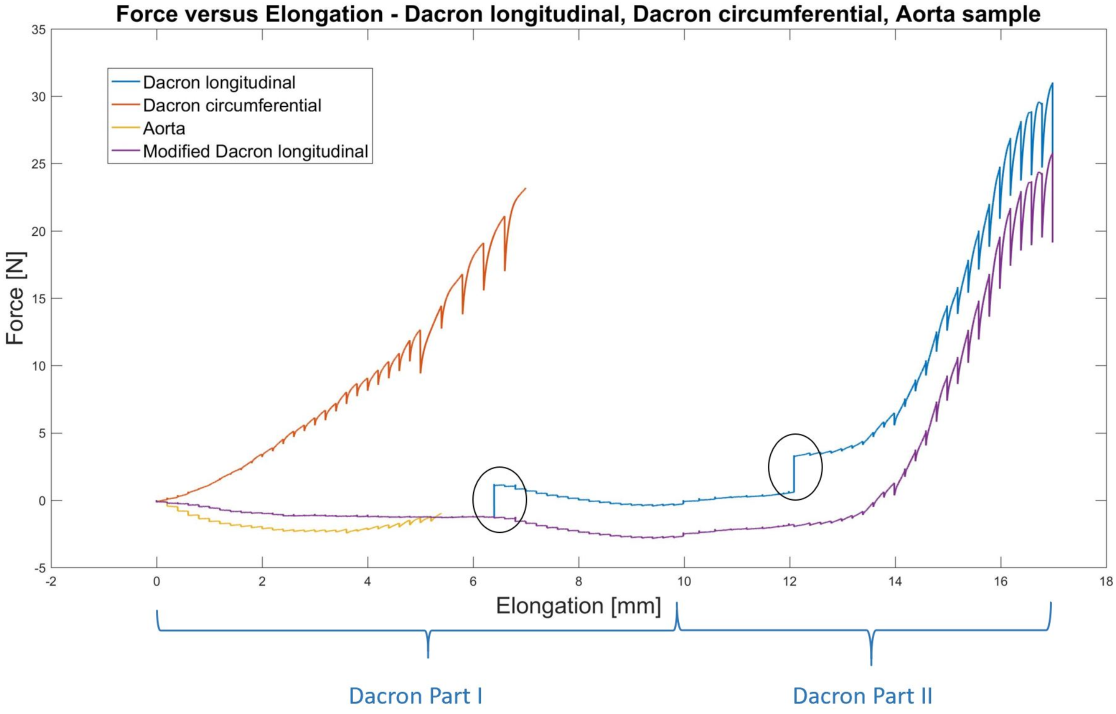

Figure 5.11: Comparison of the force versus elongation curve of all the samples.

- **Stiffness and Anisotropy**

  The true stress-strain curves of the two Dacron samples are represented on figure 5.12. The values of the tensile modulus were calculated as show on the graph at a strain of 45%. The values of the elastic modulus for Dacron longitudinal and Dacron circumferential were 5.75 MPa and 13.65 MPa, respectively (Table 5.1). There are differences between the two values, which suggest a directional dependency of the material. The Dacron circumferential is 2.4 times stiffer than the Dacron longitudinal. This could be explained by the structure of the material. As the graft is a warp knitted graft, the yarns are knitted longitudinally providing the sample with a larger elasticity in the longitudinal direction. The radial expansion of the graft is therefore limited. The anisotropy index of the Dacron sample can be calculated and is equal to 0.81.

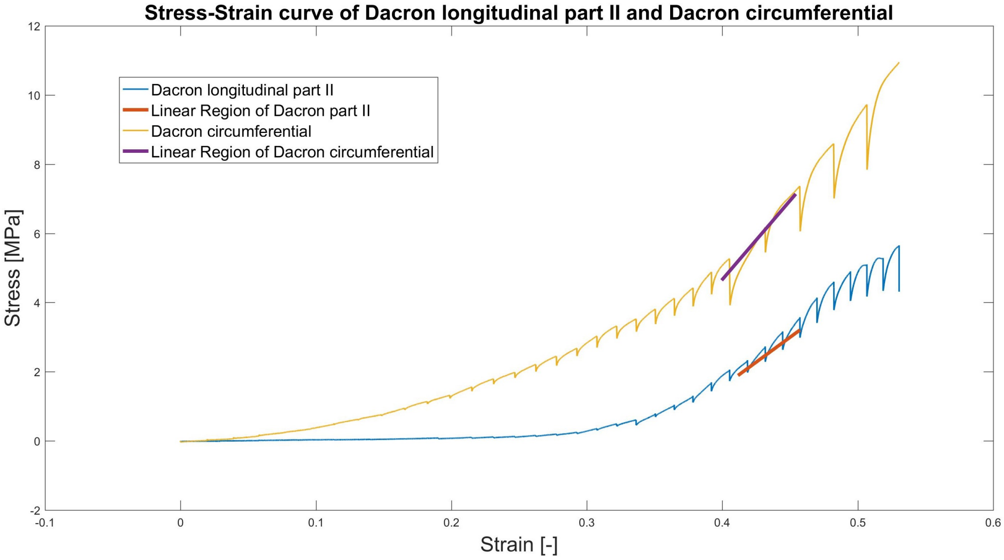

Figure 5.12: Stress-Strain curve of the Dacron longitudinal (blue) and the Dacron circumferential (yellow).

The only reviews found that studied the anisotropy of knitted Dacron graft reported values of 0.64 MPa and 12 MPa for the longitudinal and circumferential elastic modulus, respectively [86] [87]. With these values, an anisotropy index of 1.8 can be calculated. The comparison between the mentioned review and the result of this thesis should be careful since the moduli reported in the paper were evaluated at low strain and it is not clear whether the folds of the structure were taken into account. Nevertheless, an anisotropy between the two orientations was clearly identified. More recent literature identified this anisotropy for woven Dacron graft also with a anisotropy index of 0.4 [82].

The anisotropy index of Dacron can be compared with the data of healthy human ascending aorta form [82] (Table 5.1). Healthy aorta also shows a positive anisotropy index value around 0.2, meaning that, as Dacron, the circumferential direction is stiffer than the longitudinal direction. However, as experimented by [88], this large discrepancy in the anisotropy index indicates also that Dacron graft is stiffer than the aorta in the circumferential direction, which will limit the radial expansion of the graft compared to native tissue. In fact, the mismatch in circumferential stiffness could disturb the function performed by the aorta known as the "Windkessel" property [89]. As the aorta is a compliant vessel, it absorbs part of the hydraulic energy imparted to the blood during systole, which is released in diastole to maintain a constant flow. This mismatch in stiffness in the radial direction could bring complications and increase compliance mismatch when a high blood output is demanded, as during exercise. This is a topic that could be further investigated thanks to the extension-inflation test presented in chapter 4.

It is important to note that the value of elastic modulus calculated in this work are lower than the one found in the literature and stated in the "State of the art" section. This may be due to the limitations explained in the following section. Another justification could be that, as the sample was not tested until failure, the whole stress-strain curve was not recorded. Therefore, the part taken as the linear elastic region could be too close to the toe effect.

B) Aorta

- **Force versus elongation**

  The yellow curve of figure 5.11 represents the value recorded for the aorta sample. Unfortunately, due to the low sensitivity of the system, these values are difficult to interpret. Nevertheless, the variation in the value of the force is small, which means that this sample has a good elasticity in the longitudinal direction. This a characteristic that the Dacron graft replicates very well in the longitudinal direction. Also, just as for the Dacron samples, the relaxation of aorta during the 15 minutes scans is visible via the drops in the force. This is a typical behavior of the aorta wall in an uniaxial tensile test.

- **Stiffness and Anisotropy**

  The elastic modulus of the aorta could not be calculated due to the lack of reliability of the recorded values. In order to calculate this value, the experimental protocol should be adjusted.

Table 5.1: The elastic modulus of the Dacron longitudinal and Dacron circumferential as well as the anisotropy index of Dacron samples and the aorta.

	Elastic modulus	Anisotropy index
Dacron longitudinal	5.75 MPa	0.81
Dacron circumferential	13.65 MPa	
Aorta	-	0.2

C) Limitations of the experiments

This mechanical characterization experiment presents some limitations. First, the sensitivity of the loading cell was not accurate enough to study a force evolution of several newtons. More exact values of force evolution, and therefore of elastic modulus, would need to be recorded with a loading cell range of a hundreds of newtons instead of the one of 5 kN used in this work.

Secondly, the longitudinally stretched Dacron sample was tested in two parts. This was essential to perform a complete analysis of the evolution of its mechanical behavior. Due to the limited range of displacement, i.e. a maximum elongation of 10 mm inside the loading stage, the unwrapping of the folded structure had to be captured before testing the intrinsic properties of the material. Ideally, these two parts should be performed continuously without demounting and remounting the sample between the clamps with a prestretched approximately the same as at the end of "Dacron part I" experiment. If several samples should be tested this prestretch should be done carefully in order to have always the same prestretch for all the samples. This could be done by counting the number of folds that are trapped between the clamps.

Thirdly, no preconditioning of the samples was performed before recording the value of force. Preconditioning is important to stabilize the behaviour of the specimen and therefore, to acquire more accurate results. Thus, cycles of loading and unloading should be performed until repeatable force elongation curves are obtained. In addition, in the computation of the mechanical characteristics, i.e. the stress and elastic modulus, the graft cross-section area is assumed continuous, whereas the fibres have space among them and the graft is porous. Hence, the values given in the section 5.2.2 are conventional values.

Finally, only one sample of each category was tested. A more realistic view of the behavior of each sample, should be acquired by testing several specimen for each category. A statistical analysis can then be performed and an accurate distribution of the values can be obtained.

5.2.3 4D micro-CT - zero-strain test

To obtain an estimation of the accuracy and the precision of the DVC analysis, a zero-strain test was performed. The DVC methodology was applied to the two zero-strain data separated by 0.1 mm of rigid body translational displacement. The strains mesured by the DVC analysis are errors, since there was no deformation applied to the sample. This analysis was performed for the three samples.

A) Dacron longitudinal and circumferential

The zero-strain test requires the application of the DVC analysis on the ROI of each sample. The first step in the DVC analysis is the choice of the optimized size for the grid sub-volumes. The "Radial Autocorrelation" module is therefore applied to the reference image and the graph of the normalized autocorrelation in function of the distance is plotted. The graphs, as well as the reference images on which the module was applied, are shown on figure 5.13.

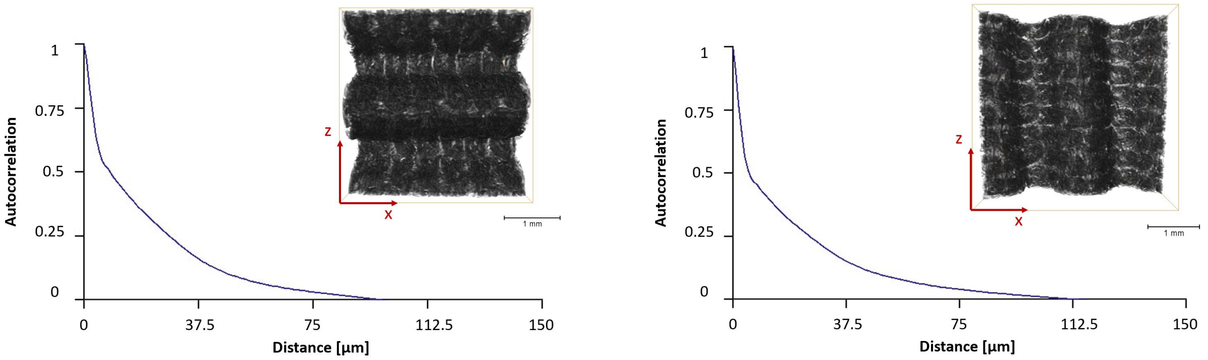

(a) Dacron longitudinal

(b) Dacron circumferential

Figure 5.13: Autocorrelation of the two samples of Dacron.

By analysing these graphs, the autocorrelation tends to zero at a distance of about 75 voxels for both samples. Applying the rule of thumb, which fixes the subset size to three to four times this distance, the subset size should range between 225 and 300 voxels. The maximal displacement that could be applied to the sample before the decorrelation between the reference and deformed image became to large is one fourth of the subset size. This gives a value ranging from 56.25 to 75 voxels which can be converted into 506.25 μm to 675 μm.

The histograms of the distribution of the strains calculated along the direction of imposed deformation, i.e. the z direction, of the two Dacron samples are shown on figures 5.14a and 5.14b. The error of the longitudinally stretched Dacron sample is ranging from -0.1% to 0.16% of strain, and the error of the circumferentially stretched sample is ranging from -0.002% to 0.08% of strain.

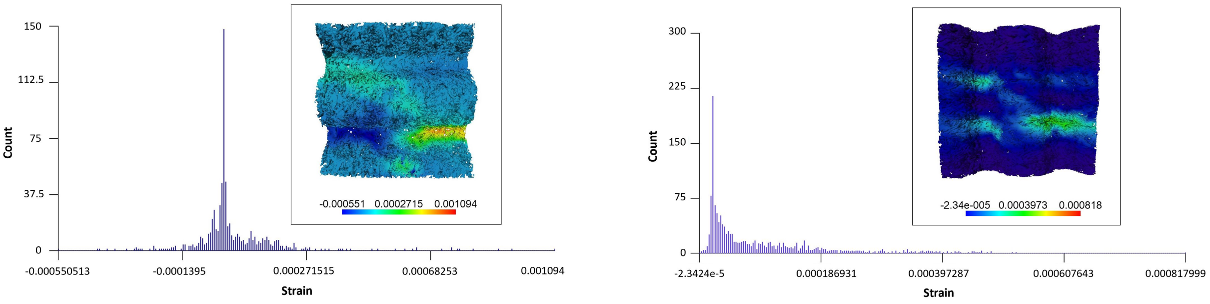

(a) Dacron longitudinal

(b) Dacron circumferential

Figure 5.14: Histogram of the distribution of the strains calculated along the direction of imposed deformation, i.e. the z direction, and strain map of the range of errors of the two Dacron samples.

The mean and the accuracy, which represents the precision and the accuracy of DVC the analysis, respectively, are presented in the table 5.2. The precision and accuracy of both Dacron samples are of the same order of magnitude. These errors may be due to the noise impacting the DVC analysis. Nevertheless, the standard deviation is very close to zero.

Table 5.2: Mean and standard deviation of the histograms of the distribution of the strains calculated along the direction of imposed deformation, i.e. the z direction, of the two Dacron samples computed from the zero-strain test.

	Dacron Longitudinal	Dacron Circumferential
Mean	3.042e-05	7.56e-05
Standard Deviation	0.000148	0.0001

On the strain map of the Dacron longitudinal microstructure (figure 5.14a), the regions where the errors were the larger are the inner part of the folds of the sample, represented in yellow. On the strain map of the Dacron circumferential microstructure (figure 5.14b), the regions where the errors were the largest are the greens strips in the same direction as the alignment of the yarns composing the structure. This information is important to take into account when interpreting the results of the DVC analysis of the next section.

B) Aorta

In the case of the aorta, the autocorrelation was more prone to errors compared with the Dacron samples. As shown on figure 5.15, the subset size to be chosen is less clear since the curve of the autocorrelation plot did not intersect the x axis at zero.

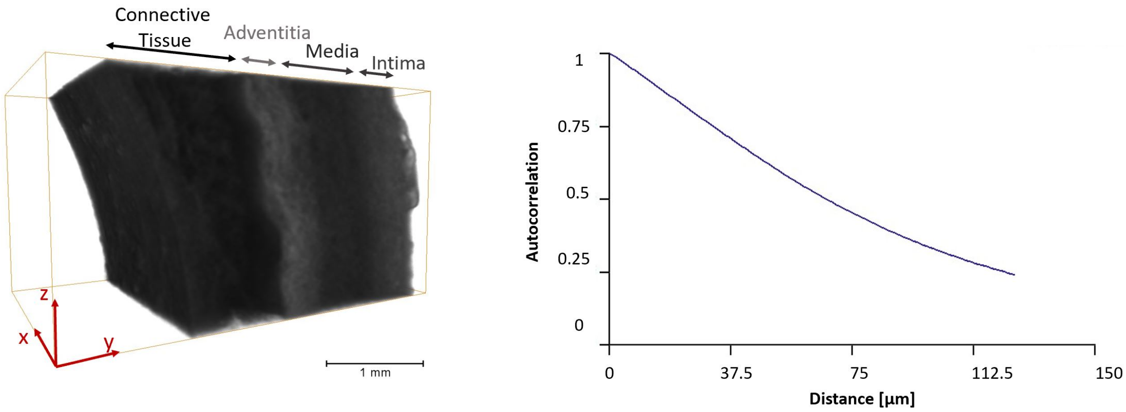

(a) Extracted ROI of the aorta sample and its complex layer structure

(b) Plot of the autocorrelation as a function of distance

Figure 5.15: Autocorrelation of the aorta sample.

This result could be attributed to the complex structure of the aorta, recalled on figure 5.15a, as well as to the insufficiency of staining. The complexity of the adequate staining of the native tissue in order to acquire reliable images already appears. Therefore, three subset sizes of 300, 240 and 180 voxels were tested. The zero-strain test was applied with each one of these grids to analyse the impact of the subset size on the error. The histograms of the strains computed by the global DVC analysis are shown on figure 5.16.

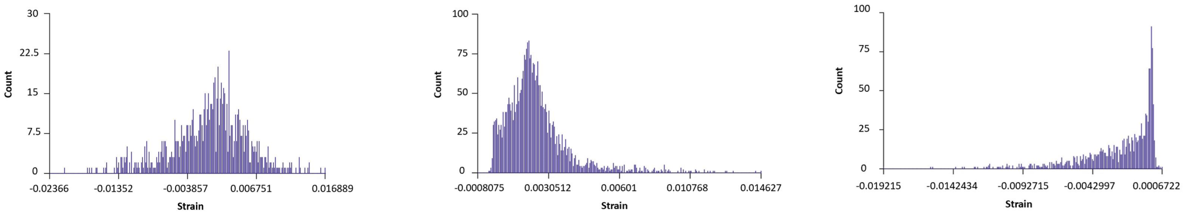

(a) Subset size = 300 voxel (b) Subset size = 240 voxel (c) Subset size = 180 voxel

Figure 5.16: Histograms of the range of error computed by the DVC analysis for three different subset sizes.

From these histograms, the range of error, the precision and the accuracy of the DVC analysis can be calculated (table 5.3). It can be observed that the error decreases with the decreasing subset size. The mean, i.e. the precision, is negative for the two first grids tested, which means that it records mainly compressive strain. It is positive for the last grid. As the test applied is a tensile test, it makes more sense to choose the 180 voxel subset size grid. The standard deviation, i.e. the accuracy, tends to be closer to zero as the subset size decreases. Hence, the outcome of this evaluation of the subset size is that a grid of 180 voxel should be taken for further analysis, as it has the lower range of tensile error and the finest accuracy.

Table 5.3: Table of the range of error in strain calculated for the aorta sample as well as the mean and standard deviation.

Subset Size	Minimal Error	Maximal Error	Mean	Standard Deviation
300	-0.0237	0.0168	-0.000233	0.00565
240	-0.0192	0.00067	-0.00237	0.00267
180	-0.000807	0.0146	0.00239	0.00176

Nevertheless, comparing this values with the ones of Dacron, a large discrepancy can be noticed. The explanation to these differences is the resolution of the aorta scans. In fact, to be able to scan the aorta sample and have sufficient contrast, a CESA had to be used. The aorta was stained during five days, which was probably not sufficient considering the results of the zero-strain test. This lack of image contrast was also an issue for the registration of the reference images with the translated images. In addition to the vertical translation, some shear was visible. This shear came from the slipping of the sample from the clamps or from a poor correlation between the two scans due to an insufficient resolution. Either way, it was a source of error.

Another interesting element to analyse is how this strain error is distributed along the different layers of the aorta. On figure 5.17, the grids with the three tested subset sizes are displayed, as well as a view of an yz plane inside the grid. Comparing figures 5.17d, 5.17e and 5.17f with the figure 5.15a, it can be observed that the maximal strains are located in the adventitia and media. This specific localisation is once again the cause of a lack of staining. The CESA had not the time to diffuse through each one of the layers of the aorta and the center layers (adventitia and media) were insufficiently stained.

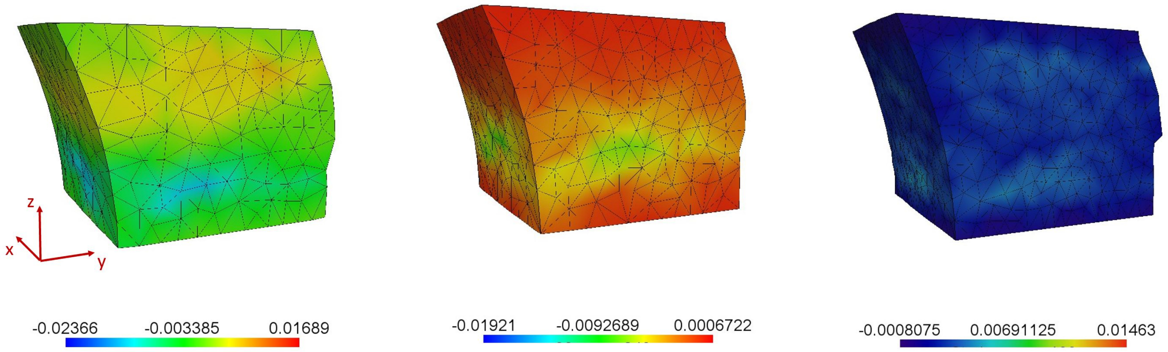

(a) Grid view with a subset size = 300 voxel

(b) Grid view with a subset size = 240 voxel

(c) Grid view with a subset size = 180 voxel

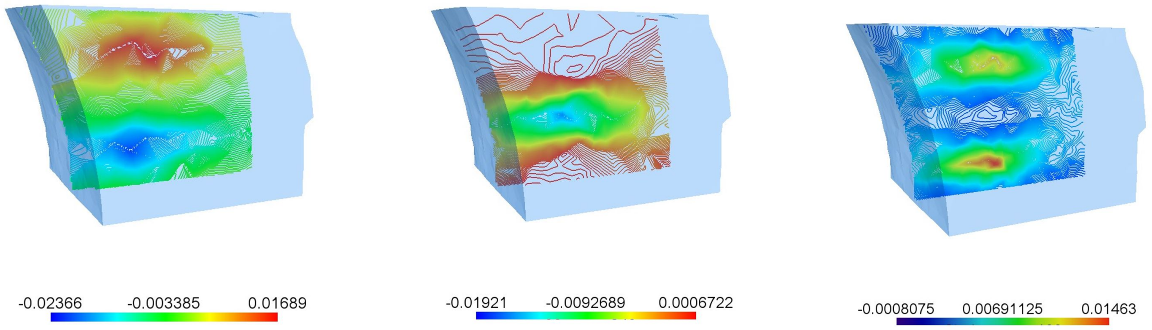

(d) Inside yz plane located at 50% of the x axis with subset size = 300

(e) Inside yz plane located at 50% of the x axis with subset size = 300

(f) Inside yz plane located at 50% of the x axis with subset size = 180

Figure 5.17: Grid view of the different subset size and analysis of one yz plane to differentiate the amount of strain error in the layers of the aorta sample.

Once again, this large level of strain errors should be kept in mind when analysing results of the DVC analysis. As the media is the layer that has the most substantial contribution, the large amount of error in this layer forces the results to be carefully discussed. Therefore, the trend of the evolution of the aorta sample under elongation will be studied rather than the specific values of strains.

5.2.4 4D micro-CT - strain mapping

A) Dacron longitudinal

The three methods of incremental DVC analysis are presented and discussed in this section. The five evaluated elongation steps are highlighted on the graph of the force versus the elongation of Dacron longitudinal part II (figure 5.18a). The ROI chosen for the DVC analysis contained one complete elongated fold, i.e. one front fold and two backwards folds (figure 5.18b).

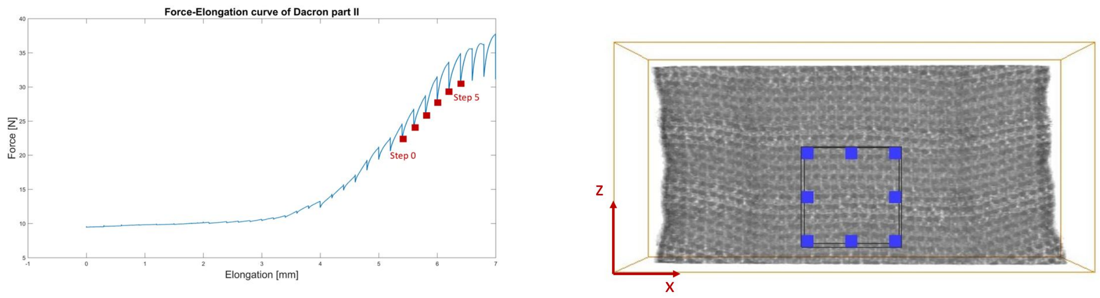

(a) Steps analyzed in the force versus elongation curve of the Dacron longitudinal part II for the three methods

(b) ROI extracted from the Dacron longitudinal elongated to 5.4 mm of displacement containing one complete folds

Figure 5.18: Force-elongation curve of Dacron lonitudinal showing (a) the steps evaluated and (b) the visualization of the ROI for the three DVC incremental methods.

"Fixed reference image" conventional DVC (Method 1) For Method 1, the maximal strains for an elongation of 1 mm are ranging from -3% to 17% (figure 5.19). By analysing the strain maps superimposing the microstructure, it can be noticed that the largest tensile strains are located on the front and backwards folds in the ROI. This demonstrates that the folding implies a stress concentration.

The advantage of this approach is that it enables to visualise the evolution of the strains for 5 steps. However, the risk of accumulation of the error due to a decorrelation between the reference and deformed image is very high. In fact, there is a variation of one order of magnitude in the compressive strains between the DVC analysis of the steps zero to three and step zero to four. This proves that this method is reliable only until a maximal displacement of 0.6 mm. This result is coherent with the maximal displacement calculated by the zero-strain test (see section 5.2.3).

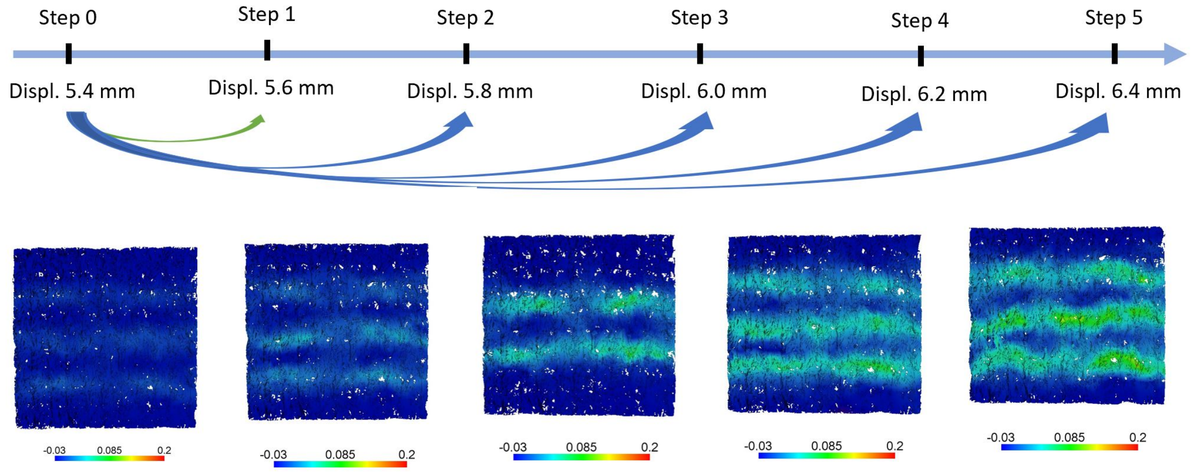

Figure 5.19: **Method 1**: Visualization of the strain map of the volumetric strains generated from the extracted ROI of Dacron longitudinal.

"Sequential" incremental DVC (Method 2) The second approach calculates the strains step by step (figure 5.20). The reference volume image is updated at each step (green arrow) preventing the issue of a decorrelation. By doing so, the strains computed are of the same order of magnitude for the DVC analysis of each steps. The sum of each maximum compressive strain and each maximum tensile strain, gives an idea of the total strain range developed in the sample after 1 mm of elongation (see figure D.1 in the Appendix for the exact strain value of each steps). The strain maps of each step exhibits, in the same way as previously, a deformation concentration at the folds.

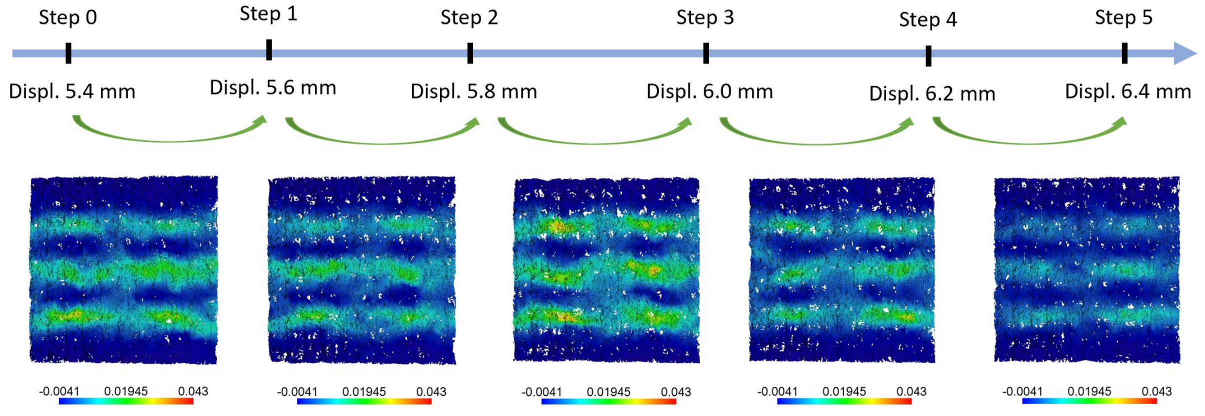

Figure 5.20: **Method 2**: Visualization of the strain map of the volumetric strains generated from the extracted ROI of Dacron longitudinal.

"Preconditioned" incremental DVC (Method 3) This third approach could be considered as a compromise of the two above methods (figure 5.21). As the maximal displacement to have reliable information about the strains developed in the sample is 0.6 mm, Method 1 is used for the three first steps. Then the reference volume image is updated at step three and becomes the fixed reference image until step five . This method induces, thus less redundant calculations and less accumulated errors. The maximal compressive strain and maximal tensile strain of the step three and the step five are added to have an idea of the total strain developed after 1 mm of elongation (see figure D.2 in the Appendix for the exact strain values of each step).

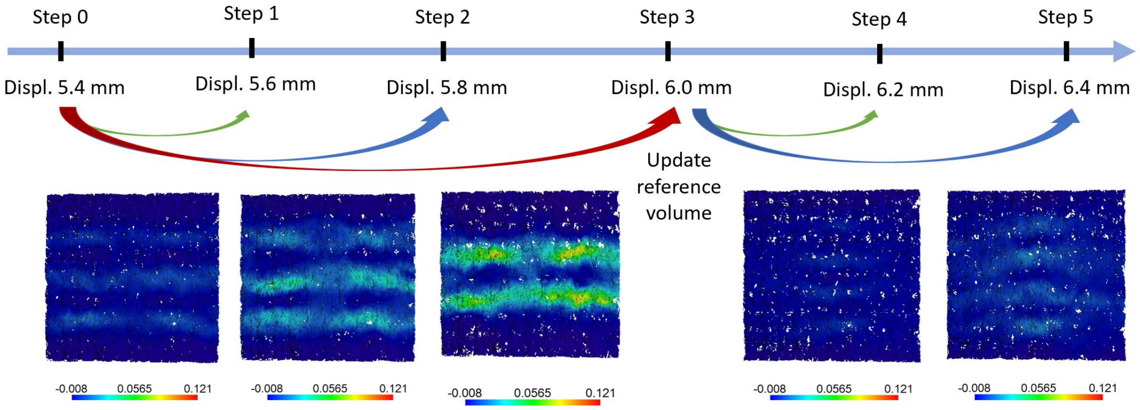

Figure 5.21: **Method 3**: Visualization of the strain map of the volumetric strains generated from the extracted ROI of Dacron longitudinal. Updated reference volume at 6 mm of elongation.

Table 5.4 compares the range of strains for the three methods. The maximal compressive strain calculated with Method 1 is three times larger than the one calculated with the "sequential" incremental DVC. The advantage of this second approach is, thus, to avoid having an unreliable value of deformation. Nevertheless, updating the reference volume image induces redundant calculation and additional accumulated errors in strains. This table indicates that Method 3 is also more accurate than the "fixed reference image" conventional DVC. In addition, compared to the "sequential" incremental DVC, it has the same order of magnitude in strains, with a lower amount of calculations and propagated errors. This method is hence, the most reliable while performing DVC analysis on large deformation.

However, in this work, as Method 1 is reliable for a maximal displacement of 0.6 millimeters and has the advantage to enable visualization of the evolution of the strains, this method has been applied for the two following samples.

Table 5.4: Table comparing the range in strain of the three methods of incremental DVC tested.

	Maximal compressive strain	Maximal tensile strain
"Fixed reference image" conventional DVC Method 1	-0.03	0.17
"Sequential" incremental DVC Method 2	-0.0097	0.163
"Preconditioned" incremental DVC Method 3	-0.00945	0.156

B) Dacron circumferential

It has been demonstrated previously with Dacron longitudinal that the results of the DVC analysis with a fixed reference volume image were reliable until a maximum of 0.6 millimeter of elongation. Therefore, this method was applied to the Dacron circumferential to analyse the evolution of the strain maps. The three evaluated steps are highlighted on the graph of the force versus the elongation of Dacron circumferential (figure 5.22a). The ROI chosen for the DVC analysis contains one complete elongated fold, i.e. one front fold and two backwards folds, as in the case of Dacron longitudinal (figure 5.22b).

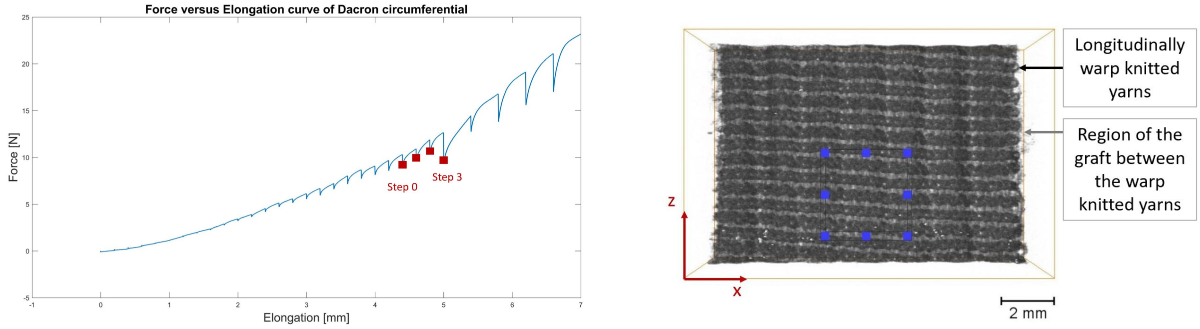

(a) Steps analyzed in the force versus elongation curve of the Dacron circumferential.

(b) ROI extracted from the Dacron circumferential elongated to 4.4 mm of displacement containing one complete fold

Figure 5.22: Force elongation curve of Dacron circumferential showing (a) the steps evaluated and (b) the visualization of the ROI .

Studying the result of the DVC analysis on the three steps highlighted on figure 5.22a, enables to visualize the location of the tensile strains while elongating the sample in the circumferential direction. By evaluating the volume rendering of figure 5.22b, it can be assumed that the region of the graft between the longitudinally warp knitted yarns of the microstructure (appearing as clearer strips on the figure), have become thinner, and therefore weaker, than the rest of the sample. Figure 5.23 confirms this with the strain maps superimposed on the microstructure. The region of maximal tensile strain of 9.04% is mostly situated between the longitudinally warp knitted yarns.

It should be noticed that between the step 2 and 3, a new region of high strain appears in the upper left corner. This can be due to fiber breaking during the elongation from 4.8 to 5.0 millimeter or due to an error of the registration. To verify this theory, a DVC analysis was performed between the step 2 and step 3 to check if a high region of strain was visible in the same region. The result of the analysis are visible on figure D.3 in the appendix D. The strain maps confirm the concentration of the strain in the middle of the ROI as well as the accumulation of the strain in the thinnest part of the sample between the longitudinally warp knitted yarns. However, it does not show any high strain concentration in the upper left corner region. This region can, therefore, be associated with a error in the registration or from the DVC analysis. By looking back at the figure 5.14b, from the zero-strain test, it can be observed that this region was also identified as an high error area.

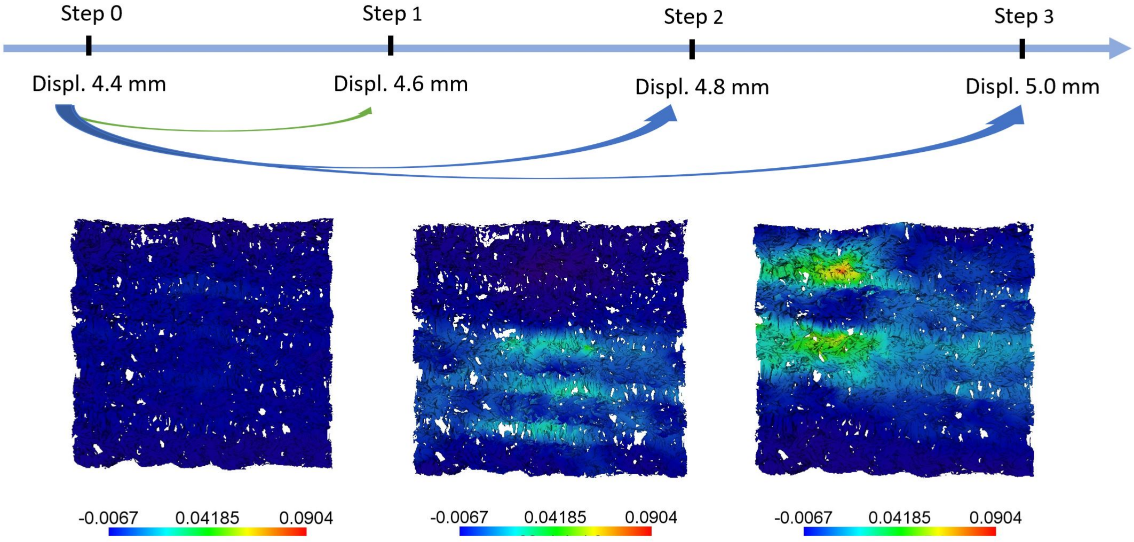

Figure 5.23: Strain maps of the "fixed reference image" DVC conventionnal analysis on Dacron circumferential from step 0 corresponding to 4.4 mm of elongation to step 3 corresponding to 5.0 mm of elongation.

Failure of the Dacron graft is more likely to happen in the circumferential direction as the folding of the microstructure, which brings elasticity and resistance to the sample, is oriented in the longitudinal direction. The structure is therefore weakened in the circumferential direction.

C) Aorta

Due to the large measurement error (section 5.2.3), only two steps could be analysed with the "fixed reference image" conventional DVC for the aorta. The relevant steps to analyze are the one located in the region where the force increases, i.e. when the low sensitivity system starts to record a force taken by the sample. The steps we analysed are situated at 4.8 mm, 5.0 mm and 5.2 mm of elongation. They are highlighted on the graph of figure 5.24a. Figure 5.24b shows the studied ROI.

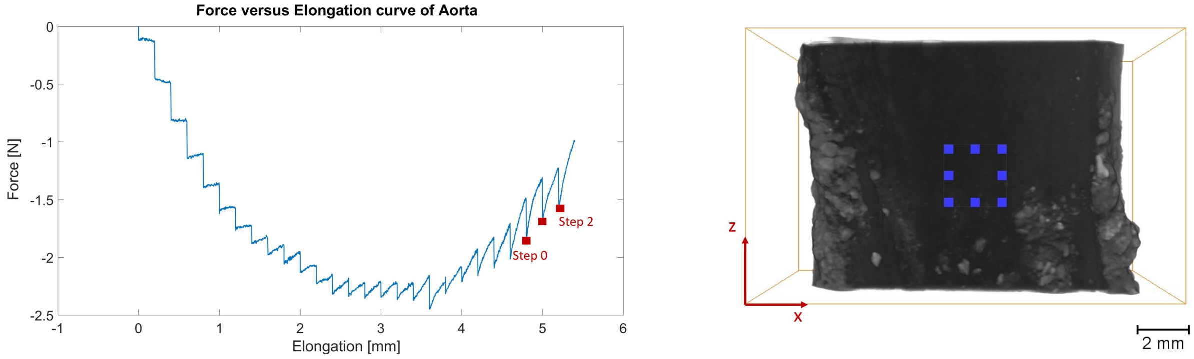

(a) Steps analyzed in the force versus elongation curve of the aorta

(b) ROI emplacement of the aorta elongated to 4.8 mm of displacement

Figure 5.24: Force elongation curve of aorta showing (a) the steps evaluated and (b) the visualization of the ROI of the aorta sample.

Figure 5.25a reminds the location of the layers of the aorta wall applied to the ROI extracted from the sample. Let's first note the thinning of the layers compared with the ROI of figure 5.15a. This thinning seems to be heterogeneous as the thickness of the media layer remains approximately the same, while the connective tissue and adventitia layer variation is more important. This result was also quantitatively assessed in [71] by calculating the Poisson's effect for each layer, confirming our results.

The strains calculated between 4.8 mm and 5.2 mm of elongation range from -0.22% to 24.4% of elongation, but due to the large measurement error, those values are not accurate. However, the visual evolution of the deformation can be analysed thanks to the grid views of figure 5.25(b ,c ,d ,e). The strains seem to concentrate at the right edge of the ROI, in the media and intima layers. Considering an inside yz plane in the structure situated at 50% of the x axis (figures 5.25d, 5.25e), this trends is confirmed and accentuated. In fact, the highest level of strain is also visible in the media and intima layers. This may be due to the weakening of the fibres in the intima. The 2D gray scale images at 4.8 mm, 5.0 mm and 5.2 mm of elongation were then observed to see if any failure mechanism could confirm this weakening theory (figure D.4 of Appendix D), but no changes were visible.

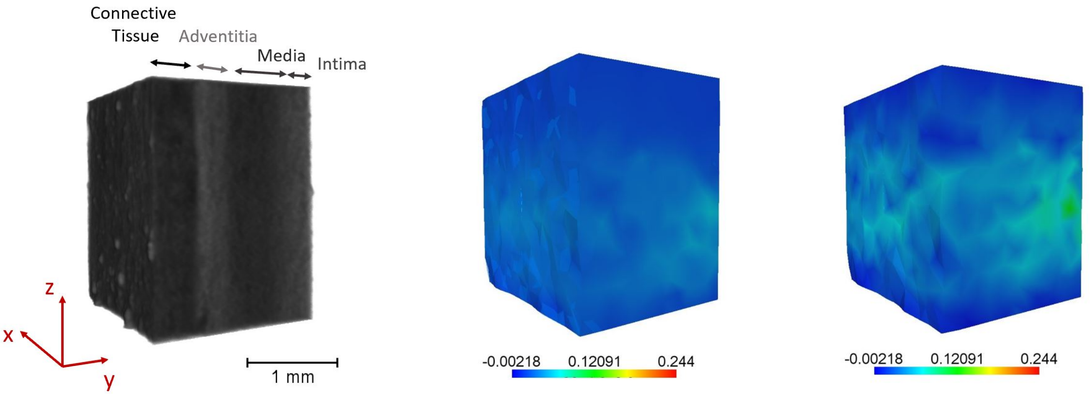

(a) ROI extracted with the aorta layers visible

(b) Grid view of the DVC analysis between the step 0 and step 1

(c) Grid view of the DVC analysis between the step 0 and step 2

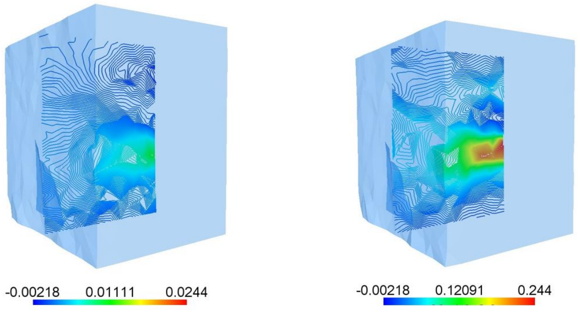

(d) Inside yz plane of the grid located at 50% of the x axis (step 0 to step 1 analysis).

(e) Inside yz plane of the grid located at 50% of the x axis (step 0 to step 2 analysis)

Figure 5.25: DVC analysis of the aorta sample from 4.8 mm of elongation to 5.2 mm of elongation.

Unfortunately, this indicates that there is an uncertainty of whether this strain concentration is due to the errors measurement (low system sensitivity and lack of staining) or due to the beginning of a failure mechanism that is not visible on the scans. For this reason, suggestions for an optimization of the protocol used for the aorta sample are presented in the following section.

D) Limitations of the current testing protocol

The protocol, and therefore the results for the three samples, still present some limitations. First, the zero-strain test was performed after all the scans were recorded. The analysis of the zero-strain test should be performed before continuing the experiment in order to have an idea of the maximal displacement possible between the scans. This could also give an idea of the errors recorded by the system, so that the parameters of the micro-CT scans could be optimized for the rest of the experiment.

Secondly, as in the case of the assessment of the mechanical properties, no preconditioning of the samples was performed. Preconditioning of the sample is important to stabilize its behaviour and, therefore, acquire more accurate results. Thus, cycles of loading and unloading of the sample could be performed before scanning the sample.

Finally, as already mentioned in the case of the mechanical properties analysis, only one sample of each category was tested and analysed. More specimens should be tested in order to have an assess of the real behaviour of the studied sample. This limitation was mostly due to the time it takes to scan the samples. In fact, scans of 10 minutes for Dacron longitudinal and Dacron circumferential, and 15 minutes for aorta where taken each 0.2 mm of elongation for a total elongation of 17 mm for Dacron longitudinal, 7 mm for Dacron circumferential and 5.4 mm for the aorta. All together, it took approximately 1600 minutes, which corresponds to nearly 27 hours. To this, the fastidious mounting and demounting time for each sample can be added.

5.3 Conclusion

Performing micro-CT imaging with *in situ* uniaxial tensile loading on native tissue and synthetic graft, namely Dacron, as well as a DVC analysis on the resulting scans, enabled to highlight interesting results but also revealed remaining limitations.

First, by a visual inspection of the sample behavior under elongation, macroscopic changes were noticed. Then, the mechanical properties were evaluated to study the intrinsic properties of the materials. Afterwards, the data acquired by the micro-CT were processed and a zero-strain test was realized to estimate the measurement error of the DVC analysis. Finally, incremental DVC was achieved and strain maps were calculated, and superimposed to the microstructure of the samples, to identify the region of highest deformation and possible failure.

The main findings are presented here separately for the synthetic Dacron graft and for the native tissue.

5.3.1 Dacron

Due to its folded structure, Dacron is a complicated sample to analyse in the longitudinal direction, especially with the limited range of space available in the uniaxial tensile test stage of the micro-CT. The experimental protocol applied in this work divided the analysis in two parts. On the one hand, the unfolding of the sample was assessed by the unwrapping of the folded structure. On the other hand, the intrinsic properties of the sample were evaluated by elastically and plastically deforming the graft. Our protocol still presents limitations, both the assessment of the mechanical properties, as for the 4D micro-CT validation and strain mapping analysis. Table 5.5 sums up the remaining limitations encountered and presents suggestions of improvement.

Table 5.5: Summary of the remaining limitations of the 4D micro-CT experiments on Dacron sample, together with suggestions to optimize the protocol.

	Limitations	**Suggestions to overcome the limitations**
Mechanical properties	Low sensitivity of the system	A load cell of 100N should be used instead of 5 kN to ensure a more accurate measurement of the force
	Lack of statistical analysis	More samples should be tested to obtain a statistically relevant evaluation of the mechanical properties of the samples and their behaviour
	Reproductibility of the experiment	The prestretch should be the same for all the samples, it can be done by counting the number of folds between the clamps in the logitudinal direction
	No preconditionning	Loading-unloading cycles should be performed to precondition the sample
4D micro-CT - Validation and strain mapping	Non-optimized parameters	Zero-strain test should be performed before continuing with the scanning of the sample to be aware of the maximal displacement and the measurement error

Even with these limitations, the first steps in the optimization of the testing protocol were taken, and interesting results were acquired from the 4D micro-CT experiment on Dacron. From the visual inspection, the longitudinal alignment of the yarns was clearly visible in both orientations of the sample. The zoom of the microstructure enabled to highlight the velour technique, characterizing a warp knitted Dacron graft. An anisotropy due to the folded structure and the aligned yarns in the longitudinal direction was also identified and further described in the evaluation of the mechanical properties.

The elastic modulus of both, the longitudinal and circumferential direction, was calculated, which allowed the computation of the anisotropic index. The sample tested in the circumferential direction was 2.5 times stiffer than in the longitudinal direction, which limits the radial expansion of the graft. However, due to its folded structure, Dacron graft has a large elasticity and resistance in the longitudinal direction.

The data processing of the micro-CT scans allowed to prepare the DVC analysis by choosing the optimized subset size. Then, a zero-strain test enabled to determine the precision and accuracy of the DVC analysis. For both directions of the Dacron graft, the result of the autocorrelation of the reference image allowed a maximum displacement of 0.5 to 0.67 millimeter of elongation before a decorrelation between the reference and deformed image, which prevents a reliable DVC analysis.

Then, we evaluated the three incremental DVC methods. The "fixed reference image" conventional DVC was reliable for a displacement of maximum 0.6 milimeter of elongation. To analyse the evolution of larger deformations, the two other methods, namely the "sequential" and "preconditionned" incremental DVC, should be used.

Finally, in our case the "fixed reference image" conventional DVC, which was reliable for 0.6 milimeter of elongation, was chosen as the best method to be applied to both Dacron samples, and later to the aorta. This enabled to evaluate and visualize where the deformations were concentrated on the microstructure. For Dacron longitudinal, the highest strains were located in the front fold and backwards fold of the folding. The folding present in the longitudinal direction, therefore, induces stress concentration. In the case of Dacron circumferential, the strains were focused in the region of the graft between the longitudinally warp knitted yarns, where the microstructure became the thinnest with the elongation. This means that the a failure mechanism is more likely to start in this region.

5.3.2 Aorta

From the experiment carried out on the aorta the main conclusion is that performing 4D CE-CT on native tissue is a real challenge due the difficulty of properly staining the tissue with the CESA. In addition to the limitation already highlighted in the case of Dacron graft, the main limitation here was the lack of staining and the limited scan resolution, thus a too low contrast in the images.

In the visual inspection, it was already clear that the tissue was not stained the same way through its whole thickness. This was then confirmed by the autocorrelation of the reference image when preparing the DVC analysis for the zero-strain test. Therefore, three different subset sizes for the global DVC analysis grid were tested. The outcome of this was to use subset size of 180 voxels. This grid had the finest accuracy and the lowest measurement error. The strain maps of the error located the highest error level in the middle of the thickness of the sample, namely around the media layer, for each one of the grid tested, reflecting the insufficient staining.

To overcome the contrast issue, the staining methodology of the native tissue should be rethought, here are three suggestions that could help to improve the quality of the acquired images.

- First, the staining agents nature and the duration of staining are important parameters to optimized. In a recent paper, already introduced in the state of the art chapter (section 2.5.5), the contrast agent used was a solution of diluted sodium polytungstate (SPT) [12]. One suggestion would be to experiment this other CESA, which could allow better quality of scan image, and compare image quality with this work.
- Secondly, due to technical limitation, the loading stage device could not get close enough to the micro-CT source and limits the voxel size to a value of 9 μm. By changing the design of this stage, this limit could be overcome and higher resolution scans could be acquire.
- One last suggestion in order to improve the quality of the analysis would be to perform high resolution scans only at some point of interest on the force elongation curve. The evolution of the sample behavior would be continuously acquired with a larger field of view, hence a lower resolution, during the *in situ* loading. At specific point, for example at partial rupture states, where a DVC analysis would be relevant, higher resolution scans would be acquired. Such a protocol would save some time of exposition of the biological sample.

Applying the "fixed reference image" conventional DVC to two steps separated of a maximum of 0.4 millimeter of elongation, the evolution of the strain maps was studied. The strains were accumulated in the center right edge of the ROI, in the intima and media layer. As no visible failure mechanism was seen in the grey scale images, this may be also the consequence of the large measurement error present.

A further objective would be to compare the data of native tissue and Dacron to highlight the differences and similarities in order to better understand its behaviour under mechanical loading and provide feedback for further extension-inflation tests. The 4D micro-CT test performed in this thesis on Dacron in the longitudinal direction can already give an idea of the force experienced by the sample in function of its elongation. This could be used in setting-up and optimizing of an extension-inflation protocol for Dacron graft.

Chapter 6

General conclusion and future perspectives

This work highlighted that the study of vascular graft is a broad and interesting field of study. It was a first step in the standardization of the experimental protocol of the extension-inflation. In addition, it emphasized the challenges of performing 4D XCT on Dacron graft and 4D CE-CT on native tissue and showed the first steps toward the optimization of this technique.

Further research in this field would be of great interest:

- **Extension-inflation tests on the three clinically applied vascular graft**: As it was revealed in this thesis, Dacron is stiffer than the aorta in the circumferential direction. It could be interesting to perform an extension-inflation test with the three grafts presented in the state of the art chapter, namely, Dacron, Gore-Tex and Vectra. The study of their respective compliance at physiological pressure and supra-physiological pressure could allow to assess at which level the graft replicates the "Windkessel" property of the aorta, essential to remain a constant pulsating blood flow even during exercise.
- **Extension-inflation tests on stained arteries**: Arteries have to be stained with a CESA in order to acquire 4D CE-CT scans of good quality. However, the effect of this CESA on the mechanical properties of the native tissue has not yet been fully assessed. Extension-inflation test accurately replicates the physiological condition, and thus performing that kind of test on stained native tissue could give insight on a possible change in mechanical properties.
- **Optimization of the staining of the native tissue**: One of the main limitations of this work concerning the aorta was the staining of the tissue. The staining of native tissue thanks to a CESA is a challenge for nowadays micro visualization technique such as micro-CT. Therefore, a study of the best CESA and staining time in order to have quality scans while performing a 4D CE-CT experiment would be

essential. Some suggestions of recently used CESA for arterial tissue could be found in literature [12].

Challenges remain in the field of biomechanics before fully characterizing the mechanical properties of vascular grafts used to create bypasses. Hopefully, the present thesis brought an incremental contribution to the complex problems still to be resolved, and will pave the way for additional research on the matter by offering ideas for the next steps. The broader purpose of improving the life of the large number of patients suffering from cardiovascular diseases motivates the scientific community to deliver further efforts.

Appendix A

Artefacts in micro-CT

Artefacts in micro-CT

First, the statistical noise, which is not normally considered as an artefact, clearly affects the quality of the image. It is generally easily identified and its effects on image analysis are fairly obvious. The noise makes small features more difficult to identify and therefore reduces the contrast resolution (figure A.1). An important parameter is the signal-to-noise ratio; it is a measure of the signal power divided by the noise power [90]. The following relationship shows how the Signal-to-Noise Ratio (SNR) is related to the flux, which is the measurement of the number of photons on the detector [91]. A solution to increase the SNR could be, for example, increasing the X-ray flux.

$$\frac{Signal}{Noise} \propto \sqrt{Flux}$$

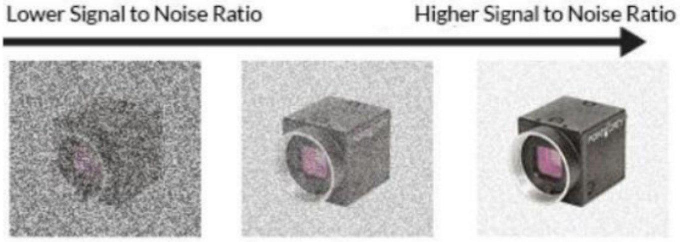

Figure A.1: Effect of Signal to Noise Ratio (SNR) on image quatity [18].

Secondly, one of the most common artefacts seen in tomography using conventional X-ray sources, is beam hardening. This artefact leads to an image where the edges appear brighter than the center, even if the material is homogeneous (figure A.2). This is due to the shift of the energy spectrum towards higher energies as a polychromatic X-ray beam is attenuated. Because attenuation is normally greater through the center of the specimen than the periphery, this results in a characteristic effect where the specimen appears to be less dense in the center. Two methods can be applied to deal with beam hardening [19]. The first one consists in linearizing the projection data using a theoretically or experimentally derived calibration curve, using a software. The second method is to use physical filtering to reduce the spectral spread. A combination of filtering and linearisation can provide the required level of accuracy for most purposes.

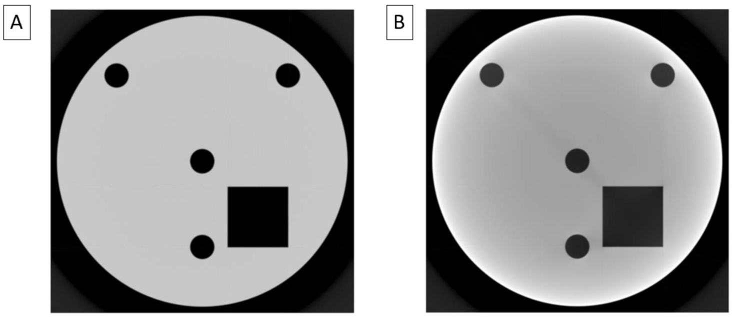

Figure A.2: Comparison of (A) a 'perfect' reconstruction with (B) beam hardening artefacts caused by use of polychromatic radiation [19].

The last artefact presented in this section is the partial volume effect (PVE). During image sampling, the attenuation properties are sampled on a voxel grid. Obviously, the contours of the voxels do not match the actual contours of the attenuation distribution. Most voxels therefore include different types of tissues. The signal intensity in each voxel is the mean of the signal intensities of the underlying tissues included in that voxel (figure A.3). The PVE affects then the apparent object size. The contours of the object, as seen on the image, may encompass more or less than the real object contours.

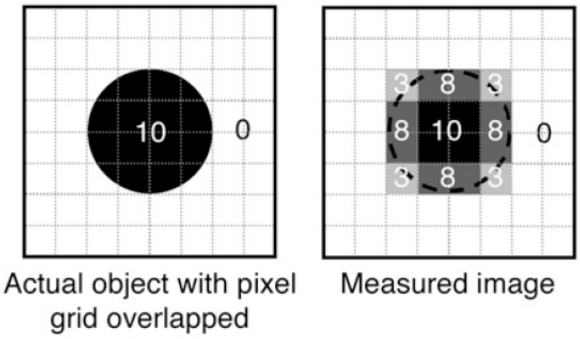

Figure A.3: Influence of image sampling on PVE. Pixels on the edges include both source and background tissues. Signal in these pixels is mean of signal intensities of underlying tissues [20].

Numerous parameters influence PVE and only some can be controlled [20]. A first parameter is the shape and the size of the object. The smaller the object, the greater the underestimation of the attenuated value. A second parameter is the spatial resolution in the reconstructed images, which is one of the most important parameters. Spatial resolution determines how far the signal spreads around its actual location. It is partly determined by scanner features, but also depends on reconstruction parameters. Therefore, PVE can be partly controlled through the choice of these parameters: better spatial resolution yields less PVE. Other parameters that influence PVE are the surrounding tissues, the image sampling, the measurement method and the difference of attenuation between the contrast and the background.

Appendix B

Stresses acting on the artery wall

In the body, when blood flows through the artery, several stresses act on its wall (figure B.1). These stresses can be defined by Laplace's and Poiseuille's laws.

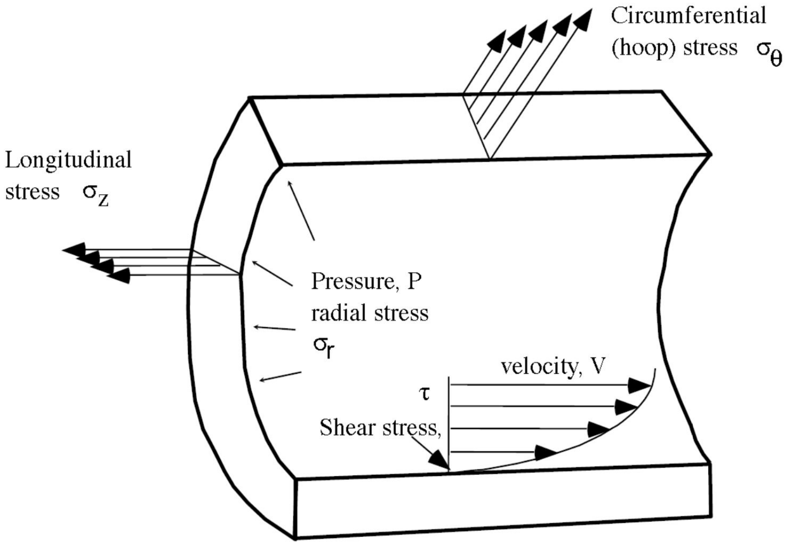

Figure B.1: Stresses acting on the arterial wall [6].

The circumferential stress is described by the law of Laplace. As stated by the first law of Newton, to respect equilibrium, the sum of the forces acting on a body at rest must be equal to zero. Therefore, taking the notations of figure B.2 the following can be written:

$$\Sigma F_x = 0$$

$$\sigma_\theta hl = P(2r_i l)$$

$$\sigma_\theta = \frac{Pr_i}{h}$$

where σ_θ is the circumferential stress, h is the thickness of the arterial wall, l is the length of the portion of artery considered, P is the internal pressure and r_i is the internal radius. By a similar process, the longitudinal stress,σ_z, can be derived:

$$\sigma_z = \frac{Pr_i^2}{r_o^2 - r_i^2}$$

where r_o is the outer radius.The shear stress, τ, comes from the law of Poiseuille which can be derived as follow:

$$\Sigma F_z = 0$$

$$P * \pi r^2 - (P - \Delta p)\pi r^2 - 2\pi r \Delta z \tau = 0$$

$$\Delta p \pi r^2 = 2\pi r \Delta z \tau$$

$$\tau = \frac{\Delta p}{\Delta z}\frac{r}{2}$$

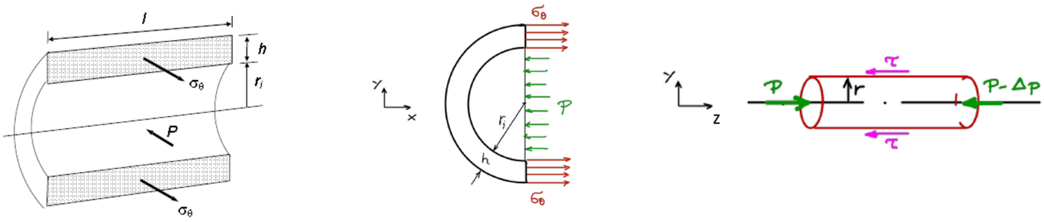

Figure B.2: Illustration of the vessel with the terms used in the definition of Laplace's law [6].

Appendix C

Digital Volume Correlation

DVC for 3D internal deformation measurement consists of the following three consecutive steps:

(1) Volumetric image acquisition: acquisition of two micro-CT volume images of the test sample before and after loading.

(2) Calculation of the 3D displacement field: specify the interrogated points within the reference volume image and track their corresponding locations in the deformed volume to extract their 3D displacement vectors.

(3) 3D strain field estimation: calculate the strain components from the displacement vector field using an appropriate numerical differentiation appraoch.

The second step requires further clarifications. Usually, a single voxel point from the reference frame cannot be reliably tracked in the deformed volume image. In fact, because of the limited grayscale depth, there exists a lot of voxel point candidates with the same intensity. Therefore, in order to reduce the variations in the graylevel distribution, a cubic subvolume centered at each interrogated point is selected, as shown on figure C.1. This subvolume can now be reliably and accurately identified in the deformed volume image.

The zero mean normalized cross-correlation (ZNCC) coefficient is used to find the location of the target cubic subvolume in the deformed image volume. For a reference cubic subvolume containing $n = (2M+1) \times (2M+1) \times (2M+1)$ voxels and an integer-voxel displacement of (u_0, v_0, w_0), the position of the subvolume in the deformed volume image is the one that gives a global maximum of the ZNCC coefficient, defined as follow [21]:

$$\begin{aligned} &C_{ZNCC}(u_0, v_0, w_0) \\ &\qquad = \frac{\sum_{i=1}^{n}[f(x_i, y_i, z_i) - f_m][g(x_i + u_0, y_i + v_0, z_i + w_0) - g_m]}{\sqrt{\sum_{i=1}^{n}[f(x_i, y_i, z_i) - f_m]^2}\sqrt{\sum_{i=1}^{n}[g(x_i + u_0, y_i + v_0, z_i + w_0) - g_m]^2}} \end{aligned}$$

where $f(x_i, y_i, z_i)$ and $g(x_i + u_0, y_i + v_0, z_i + w_0)$ are the grayscale values of the ith voxel point in the reference subvolume and target volume, respectively. $f_m = \frac{1}{n}\sum_{i=1}^{n}[f(x_i, y_i, z_i)]$

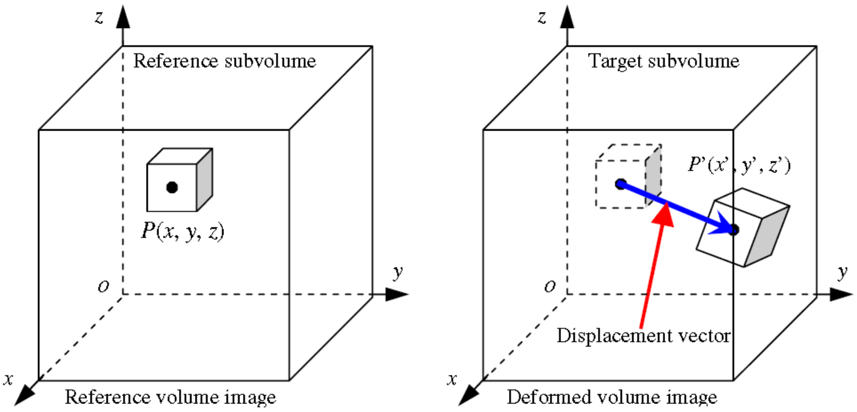

Figure C.1: Basic principle od DVC: a cubic reference subvolume, centered at the interrogated point P(x,y,z) of the reference volume image, is selected and used to track its target one in the deformed volume image. The coordinate difference between the target subvolume center P'(x',y',z') and reference subvolume center P(x,y,z) yields the 3D displacement vector at the interrogated point [21]

and $g_m = \frac{1}{n}\sum_{i=1}^{n}[g(x_i+u_0, y_i+v_0, z_i+w_0)]$ are the mean intensity values of the reference and target subvolumes, respectively.

DVC is based on the correspondence of the same image point located in the reference and deformed volume images. Two changes can result from this correspondence, explained hereunder and schematized on figure C.2.

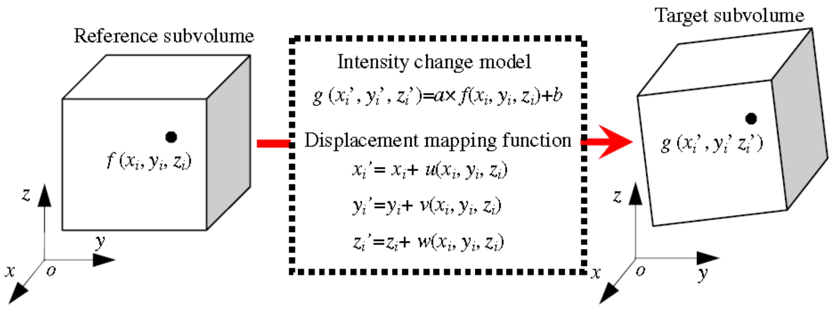

Figure C.2: Schematic demonstrating that the two changes may practically occur to a voxel point of the reference subvolume after deformation

First, the intensities and/or contrast of the voxel points may change due to the nonlinear response of a real image device. A solution to take this change into account is to use a practical linear-intensity-change model involving two additional unknow variables (i.e. a,b)[21]:

$$g(x_i', y_i', z_i') = a \times f(x_i, y_i, z_i) + b \qquad i = 1, 2, ..., n$$

A second change is the deformation of the reference subvolume in an irregular shape. This implies that the normal strain, shear strain, rotation or their combinations may also have occurred in the target subvolume. To take this issue into consideration a linear displacement mapping function is used. The coordinates of a point (x_i, y_i, z_i) in the reference subvolume, around the subvolume center, noted (x_0, y_0, z_0), can be thus mapped to the corresponding point (x'_i, y'_i, z'_i) in the deformed subvolume according to the following first-order displacement mapping function [21]:

$$x'_i = x_0 + \mathit{\Delta} x + u_0 + \mathit{\Delta} u + u_x \mathit{\Delta} x + u_y \mathit{\Delta} y + u_z \mathit{\Delta} z$$

$$y'_i = y_0 + \mathit{\Delta} y + v_0 + \mathit{\Delta} v + v_x \mathit{\Delta} x + v_y \mathit{\Delta} y + v_z \mathit{\Delta} z$$

$$z'_i = z_0 + \mathit{\Delta} z + w_0 + \mathit{\Delta} w + w_x \mathit{\Delta} x + w_y \mathit{\Delta} y + w_z \mathit{\Delta} z$$

where $\mathit{\Delta} x, \mathit{\Delta} y, \mathit{\Delta} z$ are the distance components from the center point (x_0, y_0, z_0) and the considered point (x_i, y_i, z_i); u_0, v_0, w_0 and $\mathit{\Delta} u, \mathit{\Delta} v, \mathit{\Delta} w$ are the integer-voxel and sub-voxel displacement components for the subvolume center in the x, y and z directions, respectively; and $u_x, u_y, u_z, v_x, v_y, v_z, w_x, w_y, w_z$ are the displacement derivatives of the subvolume. The nine displacement derivatives can be estimated at each point of calculation using the Iterative Least Square (ILS) algorithm [21].

The 3D strain field estimation is made by a pointwise least-squares (PLS) fitting approach. Because of the unavoidable noise contained in the recorded volume images, using the PLS approach is more accurate. The strains can be extracted by fitting a cloud of neighboring discrete displacement vectors within a predefined cube using linear least squares. If the strain calculation window is small enough, the displacements in each direction can be assumed to be linearly distributed:

$$u(x, y, z) = a_0 + a_1 x + a_2 y + a_3 z$$

$$v(x, y, z) = b_0 + b_1 x + b_2 y + b_3 z$$

$$w(x, y, z) = c_0 + c_1 x + c_2 y + c_3 z$$

where x, y, z are the local coordinates within the strain calculation box, $u(x, y, z), v(x, y, z)$ and $w(x, y, z)$ are the original displacements obtained by the ILS algorithm, and $a_{i=0,1,2,3}$, $b_{i=0,1,2,3}$, $c_{i=0,1,2,3}$ are the unknown polynomial coefficients. Once they are determined by minimizing the least-squares criteria, the six Cauchy strain components at the interrogated point can be calculated as:

$$\begin{aligned}
\epsilon_x &= \frac{\partial u}{\partial x} = a_1, & \epsilon_{xy} &= \frac{1}{2}(\frac{\partial v}{\partial x} + \frac{\partial u}{\partial y}) = \frac{1}{2}(b_1 + a_2), \\
\epsilon_y &= \frac{\partial v}{\partial y} = b_2, & \epsilon_{yz} &= \frac{1}{2}(\frac{\partial w}{\partial y} + \frac{\partial v}{\partial z}) = \frac{1}{2}(c_2 + b_3), \\
\epsilon_z &= \frac{\partial w}{\partial z} = c_3, & \epsilon_{xz} &= \frac{1}{2}(\frac{\partial u}{\partial z} + \frac{\partial w}{\partial x}) = \frac{1}{2}(a_3 + c_1),
\end{aligned}$$

Appendix D

Additional images of chapter 5

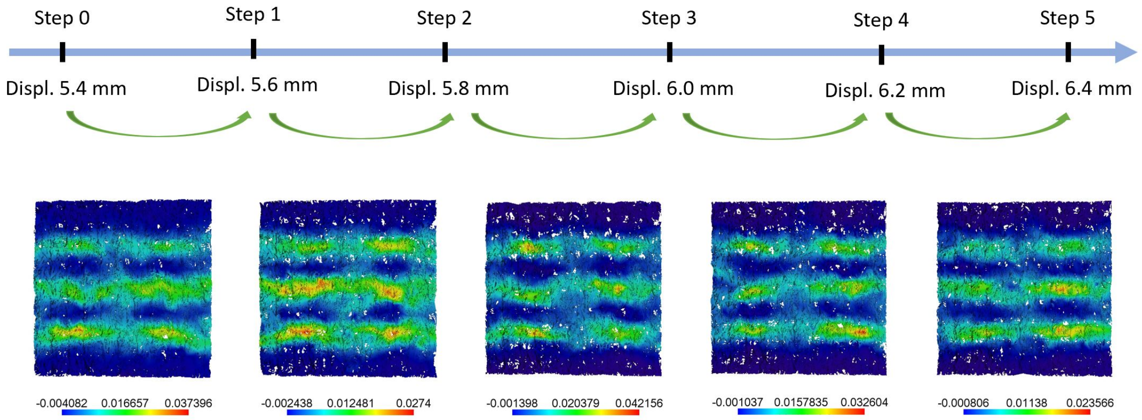

Figure D.1: Method 2: Visualization of the strain map of the volumetric strains generated from the extracted ROI of Dacron longitudinal. The colorbar indicates the strain experienced by the sample at each step. These are the values that has been summed up and listed in table 5.4.

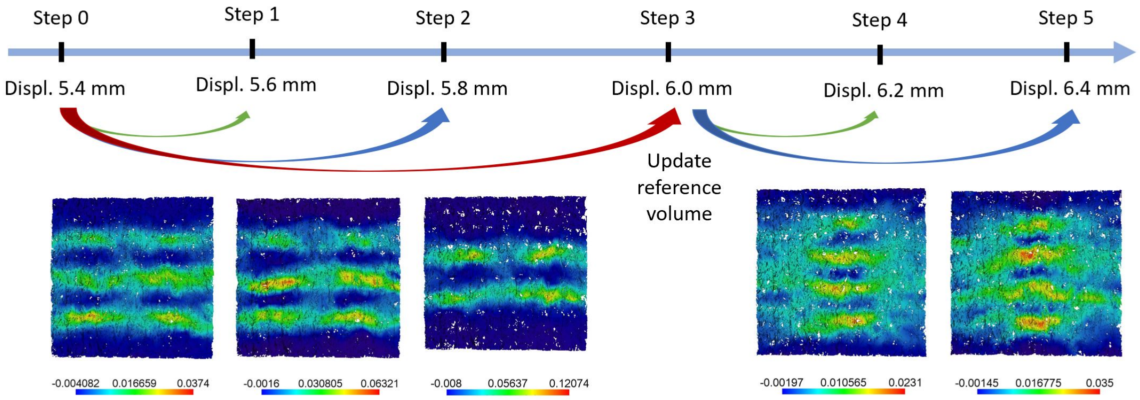

Figure D.2: Method 3: Visualization of the strain map of the volumetric strains generated from the extracted ROI of Dacron longitudinal. The colorbar indicates the strain experienced by the sample at each step. Values that has been summed up and listed in table 5.4.

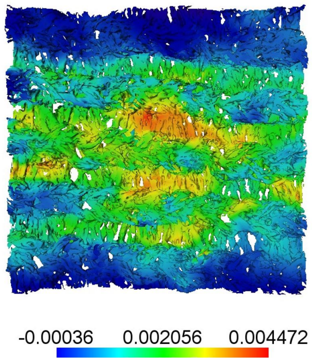

Figure D.3: Result of the DVC analysis between the step 2 and 3 of the Dacron circumferential sample. The scale bar associate the strain with a color superimposed on the microstructure of the material. The strains scale from -0.036% (dark blue) to 0.45% (red).

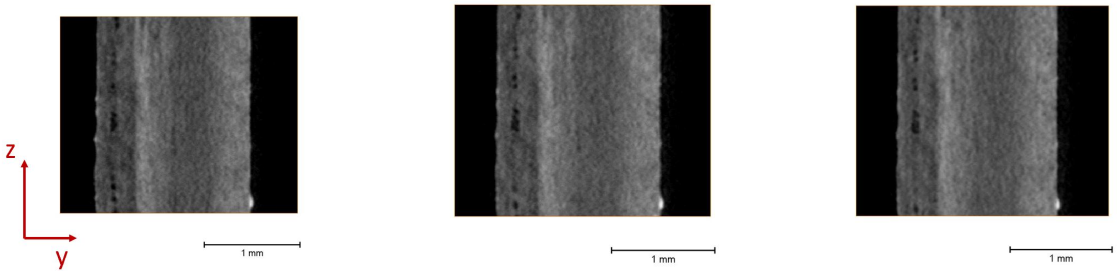

(a) 2D slice at 4.8 mm of elongation

(b) 2D slice at 5.0 mm of elongation

(c) 2D slice at 5.2 mm of elongation

Figure D.4: 2D slice of the yz plane where the maximal strains where highlighted. No visible failure mechanism is observed.

Bibliography

[1] Lina Badimon, Teresa Padró, and Gemma Vilahur. Extracorporeal assays of thrombosis. *Methods in molecular biology (Clifton, N.J.)*, 788:43–57, 01 2012.

[2] Anna V. Piterina, Aidan J. Cloonan, Claire L. Meaney, Laura M. Davis, Anthony Callanan, Michael T. Walsh, and Tim M. McGloughlin. Ecm-based materials in cardiovascular applications: Inherent healing potential and augmentation of native regenerative processes. *International Journal of Molecular Sciences*, 10(10):4375–4417, 2009.

[3] Henryk J. Salacinski et al. The mechanical behavior of vascular grafts: A review. *Journal of biomaterials applications*, 15:242–278, 2001.

[4] MA Lillie, RE Shadwick, and JM Gosline. Mechanical anisotropy of inflated elastic tissue from the pig aorta. *Journal of biomechanics*, 43(11):2070–2078, 2010.

[5] Charanpreet Singh, Cynthia S Wong, and Xungai Wang. Medical textiles as vascular implants and their success to mimic natural arteries. *Journal of functional biomaterials*, 6(3):500–525, 2015.

[6] Nikolaos Stergiopulos. Xelep1400-biomechanics of the cardiovascular system. EPFL – École polytechnique fédérale de Lausanne, 2018-2019.

[7] Kewei Li, Ray W Ogden, and Gerhard A Holzapfel. An exponential constitutive model excluding fibres under compression: Application to extension–inflation of a residually stressed carotid artery. *Mathematics and mechanics of solids*, 23(8):1206–1224, 2018.

[8] Isa CT Santos, Alexandra Rodrigues, Lígia Figueiredo, Luís A Rocha, and João Manuel RS Tavares. Mechanical properties of stent–graft materials. *Proceedings of the Institution of Mechanical Engineers, Part L: Journal of Materials: Design and Applications*, 226(4):330–341, 2012.

[9] Y Song, Jan Feijen, Dirk W Grijpma, and Andreas A Poot. Tissue engineering of small-diameter vascular grafts: a literature review. *Clinical hemorheology and microcirculation*, 49(1-4):357–374, 2011.

[10] Ryley A Macrae, Karol Miller, and Barry J Doyle. Methods in mechanical testing of arterial tissue: a review. *Strain*, 52(5):380–399, 2016.

[11] Roberto Fedele, Antonia Ciani, and Fabrizio Fiori. X-ray microtomography under loading and 3d-volume digital image correlation. a review. *Fundamenta Informaticae*, 135(1-2):171–197, 2014.

[12] Clémentine Helfenstein-Didier, Damien Taïnoff, Julien Viville, Jérôme Adrien, Éric Maire, and Pierre Badel. Tensile rupture of medial arterial tissue studied by x-ray micro-tomography on stained samples. *Journal of the mechanical behavior of biomedical materials*, 78:362–368, 2018.

[13] B Wang, B Pan, and Gilles Lubineau. Morphological evolution and internal strain mapping of pomelo peel using x-ray computed tomography and digital volume correlation. *Materials & Design*, 137:305–315, 2018.

[14] Kamel Madi, Gianluca Tozzi, QH Zhang, Jie Tong, Andrew Cossey, Andrew Au, David Hollis, and François Hild. Computation of full-field displacements in a scaffold implant using digital volume correlation and finite element analysis. *Medical engineering & physics*, 35(9):1298–1312, 2013.

[15] Maité Pétré. Master thesis: 4D CE-CT of biological tissues - Protocol for samples preparation, 2020. Université Catholique de Louvain.

[16] Deben. CT5000 5kN in-situ tensile stage for μXCT applications. `https://deben.co.uk/tensile-testing/%c2%b5xct/tensile-stages-for-x-ray-ct-tomography/`. Accessed: 2020-04-05.

[17] Bo Wang and Bing Pan. Incremental digital volume correlation method with nearest subvolume offset: an accurate and simple approach for large deformation measurement. *Advances in Engineering Software*, 116:80–88, 2018.

[18] Shane P Gilroy, John O'Dwyer, and Lucas C Bortoleto. Characterisation of cmos image sensor performance in low light automotive applications.

[19] GR Davis and JC Elliott. Artefacts in x-ray microtomography of materials. *Materials science and technology*, 22(9):1011–1018, 2006.

[20] Marine Soret, Stephen L Bacharach, and Irene Buvat. Partial-volume effect in pet tumor imaging. *Journal of Nuclear Medicine*, 48(6):932–945, 2007.

[21] Bing Pan, Dafang Wu, and Zhaoyang Wang. Internal displacement and strain measurement using digital volume correlation: a least-squares framework. *Measurement Science and Technology*, 23(4):045002, 2012.

[22] Alireza Karimi, Mahdi Navidbakhsh, Ahmad Shojaei, and Shahab Faghihi. Measurement of the uniaxial mechanical properties of healthy and atherosclerotic human coronary arteries. *Materials Science and Engineering: C*, 33(5):2550–2554, 2013.

[23] Ruben Y. Kannan, Henryk J. Salacinski, Peter E. Butler, George Hamilton, and Alexander M. Seifalian. Current status of prosthetic bypass grafts: A review. *Journal of Biomedical Materials Research Part B: Applied Biomaterials*, 74B(1):570–581, 2005.

[24] Claudio A Bustos, Claudio M García-Herrera, and Diego J Celentano. Mechanical characterisation of dacron graft: Experiments and numerical simulation. *Journal of biomechanics*, 49(1):13–18, 2016.

[25] J Chlupáč, E Filova, and L Bačáková. Blood vessel replacement: 50 years of development and tissue engineering paradigms in vascular surgery. *Physiological Research*, 58(Suppl 2):S119–S139, 2009.

[26] Will Zhang, Yuan Feng, Chung-Hao Lee, Kristen L Billiar, and Michael S Sacks. A generalized method for the analysis of planar biaxial mechanical data using tethered testing configurations. *Journal of biomechanical engineering*, 137(6):064501, 2015.

[27] Gerhard A. Holzapfel, Thomas C. Gasser, and Ray W. Ogden. A new constitutive framework for arterial wall mechanics and a comparative study of material models. *Journal of elasticity and the physical science of solids*, 61(1):1–48, Jul 2000.

[28] Gerhard Sommer, Christoph Benedikt, Justyna A Niestrawska, Gloria Hohenberger, Christian Viertler, Peter Regitnig, Tina U Cohnert, and Gerhard A Holzapfel. Mechanical response of human subclavian and iliac arteries to extension, inflation and torsion. *Acta biomaterialia*, 75:235–252, 7 2018. Copyright 2018 Acta Materialia Inc. Published by Elsevier Ltd. All rights reserved.

[29] Swathi et al. Ravi. Polymeric materials for tissue engineering of arterial substitutes. *Vascular*, 17:S45–S54, 7 2009.

[30] Hisham S Bassiouny, Scott White, Seymour Glagov, Eric Choi, Don P Giddens, and Christopher K Zarins. Anastomotic intimal hyperplasia: mechanical injury or flow induced. *Journal of vascular surgery*, 15(4):708–717, 1992.

[31] Valentin Fuster, Zahi A Fayad, and Juan J Badimon. Acute coronary syndromes: biology. *The Lancet*, 353:s5–s9, 1999.

[32] Wikipedia contributors. Stroke volume — Wikipedia, the free encyclopedia. `https://en.wikipedia.org/w/index.php?title=Stroke_volume&oldid=914618618`, 2019. [Online; accessed 1-November-2019].

[33] Yves Marois and Robert Guidoin. Biocompatibility of polyurethanes. In *Madame Curie Bioscience Database [Internet]*. Landes Bioscience, 2013.

[34] Michael N Helmus, Donald F Gibbons, and David Cebon. Biocompatibility: meeting a key functional requirement of next-generation medical devices. *Toxicologic pathology*, 36(1):70–80, 2008.

[35] Thomas A Wynn. Cellular and molecular mechanisms of fibrosis. *The Journal of Pathology: A Journal of the Pathological Society of Great Britain and Ireland*, 214(2):199–210, 2008.

[36] Robert E Shadwick. Mechanical design in arteries. *Journal of Experimental Biology*, 202(23):3305–3313, 1999.

[37] Cheng-Jen Chuong and Yuan-Cheng Fung. Residual stress in arteries. In *Frontiers in biomechanics*, pages 117–129. Springer, 1986.

[38] Taewon Kang. Mechanical behavior of arteries under inflation and extension. *Journal of Mechanical Science and Technology*, 22(4):621, 2008.

[39] Jaretzke A.L. Voorhees, A.B. and A.H. Blakemore. The use of tubes constructed from vinyon "n" cloth in bridging arterial defects. *Annals of surgery*, 135:332–336, 1952.

[40] Arthur H Blakemore and Arthur B Voorhees Jr. The use of tubes constructed from vinyon “n” cloth in bridging arterial defects—experimental and clinical. *Annals of surgery*, 140(3):324, 1954.

[41] BS Gupta and VA Kasyanov. Biomechanics of human common carotid artery and design of novel hybrid textile compliant vascular grafts. *Journal of Biomedical Materials Research: An Official Journal of The Society for Biomaterials and The Japanese Society for Biomaterials*, 34(3):341–349, 1997.

[42] Stephen D Bruck. Considerations of species-related hematological differences on the evaluation of biomaterials. *Biomaterials, medical devices, and artificial organs*, 5(1):97–113, 1977.

[43] Lian Xue and Howard P Greisler. Biomaterials in the development and future of vascular grafts. *Journal of vascular surgery*, 37(2):472–480, 2003.

[44] Gregory J Wilson, DC MacGregor, Petr Klement, Jean-Pierre Dereume, Bruce A Weber, Allen G Binnington, and Leonard Pinchuk. The composite corethane/dacron vascular prosthesis. canine in vivo evaluation of 4 mm diameter grafts with 1 year follow-up. *ASAIO transactions*, 37(3):M475–6, 1991.

[45] Alexander M Seifalian, Henryk J Salacinski, Alok Tiwari, Alan Edwards, Staffan Bowald, and George Hamilton. In vivo biostability of a poly (carbonate-urea) urethane graft. *Biomaterials*, 24(14):2549–2557, 2003.

[46] Andreas Eberhart, Ze Zhang, Robert Guidoin, Gaétan Laroche, Louis Guay, Dominique De La Faye, Michel Batt, and Martin W King. A new generation of polyurethane vascular prostheses: rara avis or ignis fatuus? *Journal of biomedical materials research*, 48(4):546–558, 1999.

[47] Anthony Ratcliffe. Tissue engineering of vascular grafts. *Matrix Biology*, 19(4):353–357, 2000.

[48] Daniel Howard, Lee D Buttery, Kevin M Shakesheff, and Scott J Roberts. Tissue engineering: strategies, stem cells and scaffolds. *Journal of anatomy*, 213(1):66–72, 2008.

[49] Ahmed A Shokeir, Ahmed M Harraz, and Ahmed B Shehab El-Din. Tissue engineering and stem cells: Basic principles and applications in urology. *International Journal of Urology*, 17(12):964–973, 2010.

[50] Crispin B Weinberg and Eugene Bell. A blood vessel model constructed from collagen and cultured vascular cells. *Science*, 231(4736):397–400, 1986.

[51] Gordon R Campbell and Julie H Campbell. Development of tissue engineered vascular grafts. *Current pharmaceutical biotechnology*, 8(1):43–50, 2007.

[52] E. O. Carew, J. E. Barber, and I. Vesely. Role of preconditioning and recovery time in repeated testing of aortic valve tissues: Validation through quasilinear viscoelastic theory. *Annals of Biomedical Engineering*, 28(9):1093–1100, Sep 2000.

[53] Heleen Fehervary. *Planar biaxial testing of soft biological tissues.* PhD thesis, KULeuven, 2018.

[54] YC Pao, JT Lu, and EL Ritman. Bending and twisting of an in vivo coronary artery at a bifurcation. *Journal of biomechanics*, 25(3):287–295, 1992.

[55] Anthony C Jones, Bruce Milthorpe, Holger Averdunk, Ajay Limaye, Tim J Senden, Arthur Sakellariou, Adrian P Sheppard, Rob M Sok, Mark A Knackstedt, Arthur Brandwood, et al. Analysis of 3d bone ingrowth into polymer scaffolds via micro-computed tomography imaging. *Biomaterials*, 25(20):4947–4954, 2004.

[56] Luc Salvo, Peter Cloetens, Eric Maire, Simon Zabler, Jean Jacques Blandin, Jean-Yves Buffiere, Wolfgang Ludwig, Elodie Boller, Daniel Bellet, and Charles Josserond. X-ray micro-tomography an attractive characterisation technique in materials science. *Nuclear instruments and methods in physics research section B: Beam interactions with materials and atoms*, 200:273–286, 2003.

[57] Shivangi Kelkar, Carol J Boushey, and Martin Okos. A method to determine the density of foods using x-ray imaging. *Journal of food engineering*, 159:36–41, 2015.

[58] Brian D Metscher. Microct for comparative morphology: simple staining methods allow high-contrast 3d imaging of diverse non-mineralized animal tissues. *BMC physiology*, 9(1):11, 2009.

[59] J-Y Buffiere, E Maire, J Adrien, J-P Masse, and E Boller. In situ experiments with x ray tomography: an attractive tool for experimental mechanics. *Experimental mechanics*, 50(3):289–305, 2010.

[60] A Guvenilir, TM Breunig, JH Kinney, and SR Stock. Direct observation of crack opening as a function of applied load in the interior of a notched tensile sample of al`[U+E5F8]` li 2090. *Acta materialia*, 45(5):1977–1987, 1997.

[61] J-Y Buffiere, E Maire, P Cloetens, G Lormand, and R Fougeres. Characterization of internal damage in a mmcp using x-ray synchrotron phase contrast microtomography. *Acta materialia*, 47(5):1613–1625, 1999.

[62] Sébastien de Bournonville, Sarah Vangrunderbeeck, Hong Giang T Ly, Carla Geeroms, Wim M De Borggraeve, Tatjana N Parac-Vogt, and Greet Kerckhofs. Exploring polyoxometalates as non-destructive staining agents for contrast-enhanced microfocus computed tomography of biological tissues. *Acta Biomaterialia*, 105:253–262, 2020.

[63] John T Johnson, Mark S Hansen, Isabel Wu, Lindsey J Healy, Christopher R Johnson, Greg M Jones, Mario R Capecchi, and Charles Keller. Virtual histology of transgenic mouse embryos for high-throughput phenotyping. *PLoS Genetics*, 2(4), 2006.

[64] Horst Detlef Litzlbauer, Christoph Neuhaeuser, Alexander Moell, Susanne Greschus, Andreas Breithecker, Folker Ernst Franke, Wolfgang Kummer, and Wigbert Stephan Rau. Three-dimensional imaging and morphometric analysis of alveolar tissue from microfocal x-ray-computed tomography. *American Journal of Physiology-Lung Cellular and Molecular Physiology*, 291(3):L535–L545, 2006.

[65] Tanja Schulz-Mirbach, Martin Heß, and Brian D Metscher. Sensory epithelia of the fish inner ear in 3d: studied with high-resolution contrast enhanced microct. *Frontiers in zoology*, 10(1):63, 2013.

[66] HJ Nieminen, T Ylitalo, S Karhula, J-P Suuronen, S Kauppinen, R Serimaa, E Hæggström, KPH Pritzker, M Valkealahti, P Lehenkari, et al. Determining collagen distribution in articular cartilage using contrast-enhanced micro-computed tomography. *Osteoarthritis and cartilage*, 23(9):1613–1621, 2015.

[67] Greet Kerckhofs, Steve Stegen, Nick van Gastel, Annelies Sap, Guillaume Falgayrac, Guillaume Penel, Marjorie Durand, Frank P Luyten, Liesbet Geris, Katleen Vandamme, et al. Simultaneous three-dimensional visualization of mineralized and soft skeletal tissues by a novel microct contrast agent with polyoxometalate structure. *Biomaterials*, 159:1–12, 2018.

[68] Sébastien de Bournonville, Sarah Vangrunderbeeck, and Greet Kerckhofs. Contrast-enhanced microct for virtual 3d anatomical pathology of biological tissues: A literature review. *Contrast media & molecular imaging*, 2019, 2019.

[69] Bo Wang, Lijuan Sun, and Bing Pan. Mapping internal deformation fields in 3d printed porous structure with digital volume correlation. *Polymer Testing*, 78:105945, 2019.

[70] Kamel Madi, Katherine A Staines, Brian K Bay, Behzad Javaheri, Hua Geng, Andrew J Bodey, Sarah Cartmell, Andrew A Pitsillides, and Peter D Lee. In situ characterization of nanoscale strains in loaded whole joints via synchrotron x-ray tomography. *Nature biomedical engineering*, pages 1–12, 2019.

[71] Víctor A Acosta Santamaría, María Flechas García, Jérôme Molimard, and Stephane Avril. Three-dimensional full-field strain measurements across a whole porcine aorta subjected to tensile loading using optical coherence tomography–digital volume correlation. *Frontiers in Mechanical Engineering*, 4:3, 2018.

[72] Marco Palanca, Andrew J Bodey, Mario Giorgi, Marco Viceconti, Damien Lacroix, Luca Cristofolini, and Enrico Dall'Ara. Local displacement and strain uncertainties in different bone types by digital volume correlation of synchrotron microtomograms. *Journal of biomechanics*, 58:27–36, 2017.

[73] Bryant C Roberts, Egon Perilli, and Karen J Reynolds. Application of the digital volume correlation technique for the measurement of displacement and strain fields in bone: a literature review. *Journal of biomechanics*, 47(5):923–934, 2014.

[74] Jing Du, Ji Hyun Lee, Andrew T. Jang, Allen Gu, Mehran Hossaini-Zadeh, Richard Prevost, Donald A. Curtis, and Sunita P. Ho. Biomechanics and strain mapping in bone as related to immediately-loaded dental implants. *Journal of Biomechanics*, 48(12):3486–3494, 2015.

[75] Víctor A Acosta Santamaría, María Flechas García, Jérôme Molimard, and Stéphane Avril. Characterization of chemoelastic effects in arteries using digital volume correlation and optical coherence tomography. *Acta Biomaterialia*, 102:127–137, 2020.

[76] Ante Buljac, Clément Jailin, Arturo Mendoza, Jan Neggers, Thibault Taillandier-Thomas, Amine Bouterf, Benjamin Smaniotto, François Hild, and Stéphane Roux. Digital volume correlation: review of progress and challenges. *Experimental Mechanics*, 58(5):661–708, 2018.

[77] Christian AJ Schulze-Bauer, Christian Mörth, and Gerhard A Holzapfel. Passive biaxial mechanical response of aged human iliac arteries. *J. Biomech. Eng.*, 125(3):395–406, 2003.

[78] Stéphane Avril, Pierre Badel, and Ambroise Duprey. Anisotropic and hyperelastic identification of in vitro human arteries from full-field optical measurements. *Journal of Biomechanics*, 43(15):2978–2985, 2010.

[79] James M Norton. Toward consistent definitions for preload and afterload. *Advances in Physiology Education*, 25(1):53–61, 2001.

[80] Nicolas Guillaud, Catherine Froustey, Frédéric Dau, and Philippe Viot. Impact response of thick composite plates under uniaxial tensile preloading. *Composite Structures*, 121:172–181, 2015.

[81] Majid Y Yousif, David W Holdsworth, and Tamie L Poepping. A blood-mimicking fluid for particle image velocimetry with silicone vascular models. *Experiments in fluids*, 50(3):769–774, 2011.

[82] Dominique Tremblay, Tiffany Zigras, Raymond Cartier, Louis Leduc, Jagdish Butany, Rosaire Mongrain, and Richard L Leask. A comparison of mechanical properties of materials used in aortic arch reconstruction. *The Annals of thoracic surgery*, 88(5):1484–1491, 2009.

[83] F Gillard, Richard Boardman, Mark Mavrogordato, Dave Hollis, Ian Sinclair, Fabrice Pierron, and Martin Browne. The application of digital volume correlation (dvc) to study the microstructural behaviour of trabecular bone during compression. *Journal of the mechanical behavior of biomedical materials*, 29:480–499, 2014.

[84] Xtra Library for ThermoFisher Scientific . Incremental global dvc. `https://xtras.amira-avizo.com/xtras/iterative-global-dvc`, 2020. [Online; accessed 14-May-2020].

[85] Jungsil Kim, Brooke Peruski, Chris Hunley, Sebastian Kwon, and Seungik Baek. Influence of surrounding tissues on biomechanics of aortic wall. *International journal of experimental and computational biomechanics*, 2(2):105, 2013.

[86] J Michael Lee and Gregory J Wilson. Anisotropic tensile viscoelastic properties of vascular graft materials tested at low strain rates. *Biomaterials*, 7(6):423–431, 1986.

[87] Subbu Venkatraman, Freddy Boey, and Luciana Lisa Lao. Implanted cardiovascular polymers: Natural, synthetic and bio-inspired. *Progress in Polymer Science*, 33(9):853–874, 2008.

[88] Giovanni Ferrari, Prabakaran Balasubramanian, Eleonora Tubaldi, Francesco Giovanniello, and Marco Amabili. Experiments on dynamic behaviour of a dacron aortic graft in a mock circulatory loop. *Journal of biomechanics*, 86:132–140, 2019.

[89] Shin Y Kim, Thomas J Hinkamp, William R Jacobs, Robert C Lichtenberg, Harold Posniak, and Roque Pifarré. Effect of an inelastic aortic synthetic vascular graft on exercise hemodynamics. *The Annals of thoracic surgery*, 59(4):981–989, 1995.

[90] Robert Kieser, Pall Reynisson, and Timothy J Mulligan. Definition of signal-to-noise ratio and its critical role in split-beam measurements. *ICES Journal of Marine Science*, 62(1):123–130, 2005.

[91] Grzegorz Pyka. XCT imaging and treatment of tomography data. University Lecture, 2020.

UNIVERSITÉ CATHOLIQUE DE LOUVAIN
École polytechnique de Louvain
Rue Archimède, 1 bte L6.11.01, 1348 Louvain-la-Neuve, Belgique | **www.uclouvain.be/epl**